Doctoral Dissertation
Doctoral Program in Energy Engineering (35th Cycle)

Comprehensive analysis of Port Water Injection as a key enabler to Hydrogen-fueled high-performance ICE operation under stoichiometric conditions

Fabrizio Gullino

******

Coordinator: Prof. Federico Millo
Supervisor: Prof. Luciano Rolando

Doctoral Examination Committee:
Prof. Kulzer, A.C., Referee, University of Stuttgart
Prof. Moro, D., Referee, University of Bologna

Politecnico di Torino
2023

Declaration

I hereby declare that, the contents and organization of this dissertation constitute my own original work and does not compromise in any way the rights of third parties, including those relating to the security of personal data.

Fabrizio Gullino

2023

* This dissertation is presented in partial fulfillment of the requirements for **Ph.D. degree** in the Graduate School of Politecnico di Torino (ScuDo).

To my loving family, whose never-ending support was worth more than I can express on paper

To Marta, for her encouragements, for the time to spend together that we had to sacrifice,

thank you

Acknowledgment

First of all, I would like to thank Ferrari S.p.A. for sponsoring this research. In particular, I would like to express my gratitude to Mr. Francesco Pulvirenti, Dr. Stefano Paltrinieri, Mr. Roberto Tonelli, Mr. Giovanni Corvaglia, Dr. Fabio Mortellaro, Mr. Pierre-Alain Hoffer, Dr. Federico Rulli, Mr. Simone Suardi, and Mr. Davide Villa for their valuable and continuous support during my doctoral work, for always finding time for constructive discussions, and for sharing with me so much knowledge about their wonderful engines.

I would like to thank my supervisor, Prof. Millo, for his wise guidance and constant support. Likewise, my sincere gratitude goes to Dr. Luciano Rolando and Dr. Andrea Piano for their constant support and valuable suggestions. Last but not least, I would like to thank all my lab-mates I have had the pleasure of working with and sharing so many pleasant moments during these years.

Abstract

Under the proposed Green Deal program, the European Union (EU) will aim to achieve zero net greenhouse gas (GHG) emissions by 2050. To shift the mobility of the future towards a zero-emission scenario, besides the fostering of powertrain electrification, which represents the most promising solution to improve the air quality in highly congested urban areas, the Green Deal also supports the development and the production of sustainable alternative fuels capable to achieve a zero impact in their entire life cycle. Among them, hydrogen (H2) has recently become a highly attractive solution since it could be produced from renewable energy sources, and its combustion generates almost zero GHG emissions. It is well known that H2 can be used with both internal combustion engines (ICEs) and fuel cells (FCs). However, hydrogen-fueled ICE represents a robust and cost-efficient option to be quickly implemented under the current production infrastructure. H2 engines are usually run ultra-lean to avoid abnormal combustion phenomena, limit the exhaust gas temperatures, minimize the emissions of nitrogen oxides (NOx) and achieve high conversion efficiencies. However, the exploitation of excess-air makes the power density very low, creating also huge challenges for the design of the charging system. In this framework, this manuscript focuses on the conversion of a high-performance 3.0L V6 Direct Injection (DI) gasoline engine in a hydrogen-fueled one. The H2-ICE is supposed to run in ultra-lean conditions at low loads, adjusting the power output by solely varying the relative Air-Fuel ratio. On the other hand, at high loads, the engine switches from ultra-lean to stoichiometric operations where, to mitigate knock and limit the exhaust gas temperature, Port Water Injection (PWI) is exploited. Before preliminarily evaluating the potential of the converted ICE, a comprehensive analysis on water injection was carried out. In particular, by exploiting a huge set of experimental data collected on a small displacement gasoline engine in dry and wet conditions, a proper methodology to simulate Port Water Injection technology was defined, analyzing in detail its knock mitigation potential and the effect of water content on the combustion process. Afterwards, due to the lack of H2-ICE experimental data, this methodology was

adapted to simulate hydrogen combustion. The H2 combustion model, together with a dedicated knock model, was then integrated into a complete H2 engine model, paving the way for a preliminary definition of displacement, Compression Ratio (CR) and turbocharger (TC) size with the aim to achieve a demanding full-load performance target, minimizing the water demand. Finally, in the process of building up a virtual engine dedicated for hydrogen development, a 3D-CFD methodology to preliminary assess the H2-air mixture formation considering different injector positions was also developed.

Contents

List of Figures XV
List of Tables XXI
List of Abbreviations XXIII
List of symbols XXVII
List of Publications XXXI
1 Introduction 1
1.1 Background 1
1.2 Hydrogen as a fuel for ICE 3
1.2.1. Hydrogen production 3
1.2.2. Hydrogen applications in Transport Sector 4
1.2.3. Hydrogen properties 5
1.2.4. H2ICE: Operating modes and Aftertreatment systems 7
1.2 Scope of the Work 9
1.3 Document Content and Structure 10
2 Port Water Injection technology 11
2.1 Introduction 11
2.2 Case study 13

2.2.1 Experimental measurements 15
2.3 Numerical Set-up 17
2.3.1 Calibration of the combustion model 17
2.3.2 Calibration of CCV model 20
2.3.3 Knock model 21
2.4 Port Water Injection Model 23
2.4.1 Port-Puddling model 23
2.4.2 Evaporation model 27
2.4.3 Water dilution effect 28
2.4.4 Port water injection model validation 30
2.5 Engine Virtual calibration 32
2.5.1 Water Injection Strategy definition 33
2.5.2 Intake Valve Lift Profile Optimization 37
2.6 Virtual test rig 39
2.6.1 Results 41
2.7 Conclusions 44
3 Hydrogen-fueled Internal Combustion Engine 46
3.1 Introduction 46
3.2 Case study 47
3.3 Hydrogen Injection Analysis 50
3.3.1 Experimental characterization of H2 injector 50
3.3.2 3D-CFD characterization of H2 injector 52
3.3.3 H2 Injection in a H2-ICE 55
3.4 H2-ICE performance analysis 62
3.4.1 Methodology 63
3.4.2 Results 66
3.5 Conclusions 77

4 Concluding remarks and Outlook 79
References 83
Appendix 95

List of Figures

Figure 1-1: Annual CO2 emissions by world region [2], t = tons.....2

Figure 1-2: Hydrogen production pathways [9].....3

Figure 1-3: Schematic of hydrogen engine performance limits and operating modes.....8

Figure 1-4: Schematic of manuscript structure.....10

Figure 2-1: 3-cylinder 1.0L Turbocharged Direct Injection Spark Ignition engine – GSE T3 [47].....14

Figure 2-2: Schematic layout of Port Water Injection system.....15

Figure 2-3: Experimental test matrix.....16

Figure 2-4: (a) Brake Mean Effective Pressure (b) Brake Specific Fuel Consumption (c) Volumetric Efficiency (d) Pressure Cycle (left) and Burn rate (right) at 3000 RPM obtained at Full-Load operating conditions without Port Water Injection; simulated (red solid line) and experimental (black dashed line).....19

Figure 2-5: Coefficient of Variation of the Indicated Mean Effective Pressure (top) and average Indicated Mean Effective Pressure over 300 CCV-cycles (bottom) at Full-Load without PWI; simulated (red solid line) and experimental (black dashed line).....21

Figure 2-6: Example of CCV simulation (a) and comparison between simulated (red solid line) and experimentally measured (black dashed line) knocking cycles percentage over 300 CCV-cycles at Full-Load without PWI (b). 22

Figure 2-7: Schematic representation of (a) port-puddling model (b) injected water behavior.....25

Figure 2-8: Example of Evaporation Index as a function of Crank Angle (CA) 25

Figure 2-9: (a) Evaporation index measured during the 3rd cycle in a row of PWI at 4000 RPM – 17 bar for Water-to-Fuel ratios of 9% (red line), 18% (blue line) 50% (green line); 1D simulation (solid line), 3D simulation (dashed line); (b) Optimized values of the calibration parameters for the port-puddling model as a function of the total injected water per cylinder 26

Figure 2-10: (a) The amount of water available before IVO, water trapped in the wall film, water backflow and water which is present into the cylinder during the combustion process as a function of the consecutive engine cycles with PWI; (b) The amount of injected water, trapped water in the wall film and the knock induction time integral as a function of the consecutive engine cycles with PWI; k ≥ 13 cycles 26

Figure 2-11: (a) In-cylinder temperature measured at IVC and (b) Volumetric Efficiency as a function of the Water-to-Fuel ratio for different values of the FHW model calibration parameter; operating point 2500 RPM – 18 bar 28

Figure 2-12: (a) Crank Angle corresponding to 50% of fuel burned (top), and maximum in-cylinder pressure (bottom) as a function of the Water-to-Fuel ratio; (b) Pressure Cycle (left), and Burn Rate (right) for a Water-to-Fuel ratio of 90%; operating point 2500 RPM – 18 bar; simulated (solid lines) and experimental (black dashed line) 30

Figure 2-13: Experimental Coefficient of Variation of the Indicated Mean Effective Pressure at Full-Load in dry (red bars) and wet (blue bars) conditions .31

Figure 2-14: In-cylinder Pressure (left), and Burn rate (right) at 4000 RPM – Full-Load both in dry and wet conditions; simulated (red solid line) and experimental (black dashed line) 32

Figure 2-15: Correlation plots between 1D-CFD predictions and experimental results: combustion center of gravity MFB50 (top left), combustion duration MFB10-90 (top right), Brake Specific Fuel Consumption (bottom left), and maximum in-cylinder pressure (bottom right). 33

Figure 2-16: (a) Spark timing, (b) Combustion center of gravity angle MFB50, (c) Burn duration (10-90%) and (d) Brake Specific Fuel Consumption as a function of the injected water mass per cylinder at the operating point 2500 RPM – 18 bar BMEP.....35

Figure 2-17: Engine (configuration 3) map of the injected water mass per cylinder 36

Figure 2-18: Engine map of the variation of (a) combustion center of gravity angle, (b) burn duration (10-90%) and (c) Brake Specific Fuel Consumption between engine variants 2 and 3. 36

Figure 2-19: Schematic representation of the engine variants with CR 13.....37

Figure 2-20: (a) Combustion center of gravity angle, (b) burn duration (10-90%) and (c) Brake Specific Fuel Consumption obtained as a function of injected water per cylinder and Intake Valve opening duration for the operating point 2500 RPM × 18 bar BMEP.....38

Figure 2-21: Engine map of the reduction of the injected water mass per cylinder obtained though the intake valve lift profiles optimization. 39

Figure 2-22: 95th percentile of VxApos (vehicle velocity multiplied by vehicle positive acceleration) as a function of driving cycles.....42

Figure 2-23: (a) Water consumption and (b) CO2 emission reduction as a function of driving cycles 43

Figure 2-24: Operating points covered by the engine along the NEDC and the RTS95 driving cycles.....43

Figure 3-1: H2 injector sample geometry 48

Figure 3-2: Jet penetration as a function of time for different injection and chamber pressures.....51

Figure 3-3: Jet penetration as a function of time for different injector mounting positions z and chamber pressures.....51

Figure 3-4: Vessel used for experimental data acquisition and numerical domain 52

Figure 3-5: Hexahedral mesh adopted for the H2 injection analysis work. In this representation, the injector mounting position corresponds to z = 0 mm. The needle geometry is blurred for confidentiality reasons.....53

Figure 3-6: Penetration curve (top) and jet width measured 21 mm from injector tip (bottom) as a function of time. Experimental (dashed lines) and simulated (solid lines). Fixed parameters: P_f = 40 bar, P_{ch} = 1.2 bar 55

Figure 3-7: Schematic of the combustion chamber from the top, intake valves on the right and exhaust valves on the left. Injector central-mounted in grey, intake side mounted in light blue and exhaust side mounted in red. 56

Figure 3-8: Evolution of lambda distribution throughout the compression stroke for tests 1, 2 and 3 (see Table 3-4).....59

Figure 3-9: Mixture concentration distribution at TDCf (top) and Tumble index as a function of crank angle (bottom) for tests 1, 2 and 3 (see Table 3-4) 60

Figure 3-10: Evolution of lambda distribution along the compression stroke for tests 4, 5 and 6 (see Table 3-4) 61

Figure 3-11: Mixture concentration distribution at TDCf (top) and Tumble index as a function of crank angle (bottom) for tests 4, 5 and 6 (see Table 3-4) ..62

Figure 3-12: Schematic representation of burn duration estimation for a hydrogen engine.....64

Figure 3-13: Configuration 1 (TC), Water-to-Fuel ratio required at 8500 RPM full-load by different engine displacements as a function of the brake torque achieved at 2000 RPM in dry conditions (x-axis) and the brake power reached at 8500 RPM exploiting PWI (y-axis) 67

Figure 3-14: Fuel energy split in dry operating conditions as a function of engine displacement.....68

Figure 3-15: Configuration 1 (TC), maximum in-cylinder pressure (top), anchor angle MFB50 (middle), Water-to-Fuel ratio (bottom) as a function of brake power achieved at 8500 RPM with three different levels of engine displacement.....69

Figure 3-16: Configuration 2 (SC), Water-to-Fuel ratio required at 8500 RPM full-load by different engine displacements as a function of the brake torque achieved at 2000 RPM in dry conditions (x-axis) and the brake power reached at 8500 RPM exploiting PWI (y-axis) 70

Figure 3-17: Performance of configurations 1 and 2, considering 3 different engine displacements, as a function of maximum torque achieved at 2000 RPM in ultra-lean conditions, i.e. lambda 2.8 (x-axis) and fuel consumption measured at the operating point 2000 RPM – 32% of LET target.....71

Figure 3-18: Configuration 1 (TC), brake power at 8500 RPM (top-left), brake torque at 2000 RPM (top-right), anchor angle MFB50 (bottom-left) and Water-to-Fuel ratio at 8500 RPM full-load (bottom-right) as a function of turbocharger scaling factor (x-axis) and compression ratio (y-axis).....73

Figure 3-19: Configuration 1 (TC), 5L H2-ICE maps of brake thermal efficiency (top-left), lambda (top-right), Water-to-Fuel ratio (bottom-left) and intake manifold pressure (bottom-right).....75

Figure 3-20: Configuration 1 (TC), 5L H2-ICE maps of combustion anchor angle (top-left), burn duration 10-90% (top-right), maximum in-cylinder pressure (bottom-left) and turbine inlet temperature (bottom-right).....76

List of Tables

Table 1-1: Hydrogen properties [7] 6

Table 2-1: GSE T3 Engine specifications 14

Table 2-2: Main vehicle characteristics for the NEDC, WLTC, FTP75, Artemis Motorway cycle, RDE, RTS95 and US06 15

Table 2-3: Optimized values of the calibration parameters of the SITurb combustion model 20

Table 2-4: Optimized values of the calibration parameters for the CCV model 21

Table 2-5: Optimized value of the calibration parameters for the Knock model 22

Table 3-1: V6 120° Twin Turbocharged DISI engine specifications 49

Table 3-2: HTV19000 Harrop supercharger (SC) main characteristics 49

Table 3-3: Experimental Schlieren measurements boundary conditions 50

Table 3-4: Boundary conditions of mixture formation simulations 56

List of Abbreviations

1D	One Dimensional
3D	Three Dimensional
aSoE	after Start of Energizing
aTDCf	after Top Dead Center Firing
ATS	Aftertreatment System
BEV	Battery Electric Vehicle
bIVC	before Intake Valve Closing
BMEP	Brake Mean Effective Pressure
BSFC	Brake Specific Fuel Consumption
B-SUV	B-Segment Sport Utility Vehicle
BTE	Brake Thermal Efficiency
CAC	Charge Air Cooler
CCV	Cycle-to-Cycle Variability
CFD	Computational Fluid Dynamic

CO	Carbon Monoxide
CO2	Carbon Dioxide
COV	Coefficient of Variation
CR	Compression Ratio
deg	Crank Angle degrees
DI	Direct Injection
DoE	Design of Experiment
EGR	Exhaust Gas Recirculation
EI	Evaporation Index
EOI	End Of Injection
ET	Energizing Time
EU	European Union
FC	Fuel Cell
FHV	Fraction of vaporized Heat taken from Walls
FTP75	Federal Test Procedure
GHG	Greenhouse Gases
GT	Gamma Technologies
HC	Hydrocarbons
ICE	Internal Combustion Engine
IEA	International Energy Agency
IMEP	Indicated Mean Effective Pressure
IVC	Intake Valve Closing
IVO	Intake Valve Opening

ISFC	Indicated Specific Fuel Consumption
Lambda	Relative air-to-fuel ratio
LET	Low-End Torque
LFS	Laminar Flame Speed
LHV	Lower Heating Value
LIVC	Late Intake Valve Closing
N2	Nitrogen
NOx	Nitrogen Oxides
MBT	Maximum Brake Torque
MFB10-90	10-90% Mass Fuel Burned angle
MFB50	50% Mass Fuel Burned angle
NEDC	New European Driving Cycle
P3	Turbine Inlet Pressure
PFI	Port Fuel Injection
PID	Proportional-Integral-Derivative
PISO	Pressure Implicit with Splitting Operator
PM	Particulate Matter
PVM	Puddle Velocity Multiplier
PWI	Port Water Injection
RANS	Reynolds-Averaged Navier-Stokes
RDE	Real Driving Emissions
RON	Research Octane Number
RPM	Round Per Minute

RTS-95	Standardized Random Test - Aggressive
SF	Scaling Factor
SI	Spark Ignition
SOI	Start Of Injection
T-DISI	Turbocharged Direct Injection Spark Ignition
T2	Compressor Outlet Temperature
T3	Turbine Inlet Temperature
TBD	To Be Defined
TDC	Top Dead Center
TJI	Turbulent Jet Ignition
TTW	Tank To Wheel
UNECE	United Nations Economic Commission for Europe
US06	Supplemental Federal Test Procedure
vECU	virtual Engine Control Unit
VVA	Variable Valve Actuation
w/	with
W/F	Water-to-Fuel ratio
w/o	without
WI	Water Injection
WOT	Wide Open Throttle
WLTC	Worldwide Harmonized Light-Duty Test Cycle
WLTP	Worldwide Harmonized Light-Duty Test Procedure

List of symbols

ϕ	Equivalence Ratio
λ	Taylor Microscale
ρ_u	Unburned Gas Density
τ	Induction Time
ω	Engine Speed
A_f	Flame Area
C_λ	Taylor Length Scale Multiplier
C_D	Dilution Effect Multiplier
C_k	Flame Kernel Growth Multiplier
C_S	Turbulent Flame Speed Multiplier
D_i	Mass Fraction of Diluents
L_t	Turbulent Length Scale
M_1	Knock Induction Time Multiplier
M_2	Activation Energy Multiplier

$\mathbf{M_b}$	Burned Mass
$\mathbf{m_{back}}$	In-Cylinder Water Mass that flows back to the Intake Ports
$\mathbf{M_e}$	Entrained Mass
$\mathbf{m_{film}}$	Water Trapped In The Wall Film
$\mathbf{m_{H_2O,liq}}$	In-cylinder Mass of Liquid Water
$\mathbf{m_{H_2O,vap}}$	In-cylinder Mass of Water Vapor
$\mathbf{m_{inj}}$	Injected Water Mass per Cylinder
$\mathbf{m_{trap}}$	Water Mass Trapped in the Cylinder after IVC
$\mathbf{M_u}$	Unburned Mass
$\mathbf{^{(n)}}$	Cycle Number
$\mathbf{p}$	In-cylinder Pressure
$\mathbf{P_{ch}}$	Chamber Pressure
$\mathbf{P_f}$	Fuel Pressure
$\mathbf{p_{max}}$	Maximum in-cylinder Pressure
$\mathbf{R_f}$	Flame Radius
$\mathbf{S_L}$	Laminar Flame Speed
$\mathbf{S_T}$	Turbulent Flame Speed
$\mathbf{t}$	time
$\mathbf{T_{ch}}$	Chamber Temperature
$\mathbf{T_f}$	Fuel Temperature
$\mathbf{t_i}$	Actuation time of injector
$\mathbf{t_{knock}}$	autoignition instant

$\mathbf{T_u}$	Temperature of the Unburned Gas
u'	Turbulent Intensity
z	H2 injector retraction (axial mounting position)

List of Publications

Part of the work described in this thesis was previously published in:

- Millo, F.; Gullino, F.; Rolando, L., "*Methodological Approach for 1D Simulation of Port Water Injection for Knock Mitigation in a Turbocharged DISI Engine*", Energies 2020, 13, 4297. https://doi.org/10.3390/en13174297.

- Gullino, F., Millo, F., and Rolando, L., "Numerical Assessment of Port Water Injection Capabilities to Reduce CO2 Emissions of a Lambda 1 Turbocharged Spark Ignition Engine," SAE Technical Paper 2023-01-0181, 2023. https://doi.org/10.4271/2023-01-0181.

- Millo, F., Piano, A., Rolando, L., Accurso, F., Gullino, F., et al., "Synergetic Application of Zero-, One-, and Three-Dimensional Computational Fluid Dynamics Approaches for Hydrogen-Fuelled Spark Ignition Engine Simulation," SAE Int. J. Engines 15(4):561-580, 2022. https://doi.org/10.4271/03-15-04-0030.

- Paltrinieri, S., Olcuire, M., Calia, V., Mortellaro, F., Gullino, F., et al., "Experimental and Numerical Investigation of Hydrogen Injection and its Preliminary Impact on High Performance Engines Development," SAE Technical Paper 2023-01-0402, 2023, https://doi.org/10.4271/2023-01-0402.

Chapter 1

Introduction

1.1 Background

The entire scientific community agrees that there is a solid and incontestable relation between global Greenhouse Gases emissions, their concentration in the atmosphere, and the average global air and sea temperatures. The inexorable growth in energy demand and the heavy dependence on fossil fuels has led to significant increases in global carbon dioxide (CO2) emissions, despite major technology-driven improvements in energy efficiency and the rapid growth of renewables for power generation. As a matter of fact, in 2022 the global CO2 emissions grew of 0.9% or 321 Mtons to a new all-time high of 36.8 billion tons. Last year's increase follows two years of exceptional oscillations in energy-related emissions, as shown in Figure 1-1. Emissions shrank by more than 5% in 2020, due to the Covid-19 pandemic cut in energy demand. In 2021, emissions returned to past pre-pandemic levels, growing more than 6% in tandem with economic stimulus and the roll-out of vaccines [1].

The huge climate changes observed in the last decades as a consequence of GHG emissions boosted the efforts of the European Union to decarbonize its economy. Indeed, despite being responsible for less than 15% of the total CO2 emitted in the last 10 years, the EU, with the European Green Deal announced at the end of 2019, declared its aim to achieve the carbon neutrality by 2050.

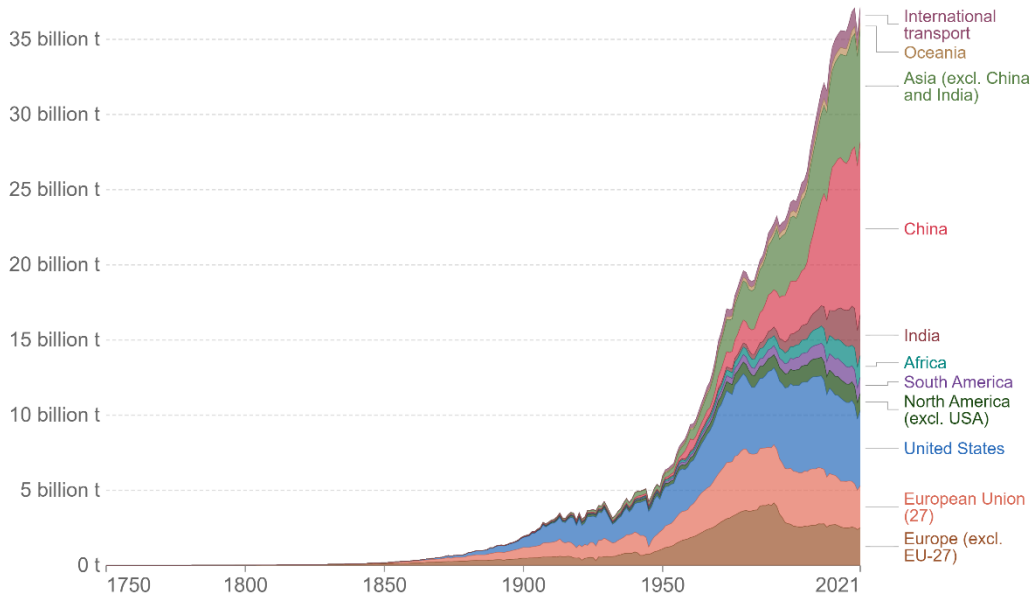


Figure 1-1: Annual CO2 emissions by world region [2], t = tons

In such a framework, the main goals concern the phase-out of the coal used for power generation and the reduction of methane emissions. Particular attention is also devoted to the shift toward more sustainable mobility since the road transportation sector is responsible for 18% of the total CO2 emissions and, differently from other relevant sectors (i.e. industry and buildings), has shown an increasing trend in the past 25 years [3]. Besides the fostering of powertrain electrification, which represents the most promising solution to improve the air quality in highly congested urban areas, the European Green Deal also supports the development and the production of sustainable alternative fuels capable to achieve a zero impact in their entire life cycle [4]. Among them, hydrogen has recently become a highly attractive solution since it could be produced from renewable energy sources, and its combustion generates almost zero GHG emissions. In this context, the European Commission initiated a new dedicated strategy on hydrogen in Europe [5], simultaneously launching the European Clean Hydrogen Alliance [6], aiming to assist in large scale the deployment of H2 technologies and infrastructures by 2030.

1.2 Hydrogen as a fuel for ICE

1.2.1. Hydrogen production

The universal applicability of hydrogen for modern energy needs (i.e. heat generation, production of industrial feedstock, refining processes, etc...) has boosted the investments on the development of technologies for renewable hydrogen production by many countries, with China being the largest importer and the US being the largest exporter, as of 2017. Australia, Japan and Germany have also defined strategic plans to become major players in the potential future hydrogen economy [7]. As of 2016, 96% of the total hydrogen production (i.e., ~55 million tons per annum) originated from fossil fuels [8]. Apart from the thermo-chemical conversion of coal and oil into hydrogen (the so-called black hydrogen), steam methane reforming is the most widely adopted method for 'grey hydrogen' production due to its cost effectiveness. However, it is worth to point out that CO2 is produced also during the steam methane reforming process. Therefore, as shown in Figure 1-2, due to the fossil feedstock, hydrogen produced through these chemical pathways is not considered renewable. Instead, the 'Blue hydrogen', obtained through the natural gas reforming with Carbon Capture and Storage (CCS) technology, could help rapidly build up the demand for clean H2. However, even in the long-run, this technology will hardly achieve carbon neutrality due to residual

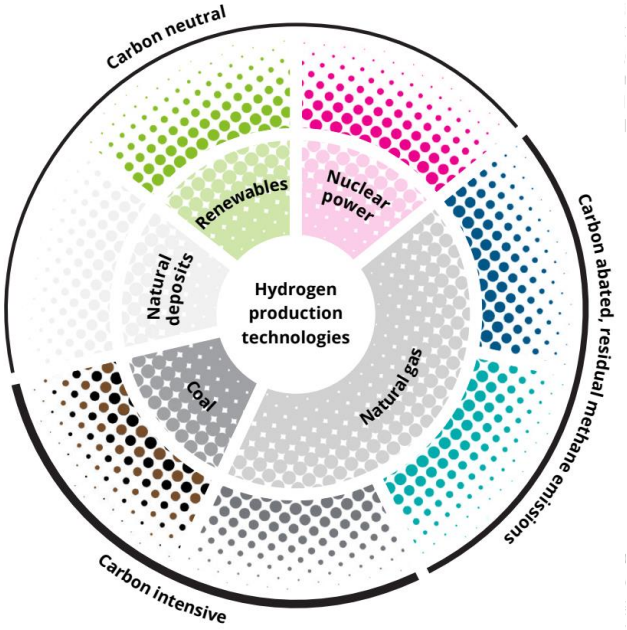


Figure 1-2: Hydrogen production pathways [9]

emissions (the highest carbon capture rate is currently estimated at around 95%) and upstream methane emissions. As an alternative, 'Turquoise hydrogen' can be produced via pyrolysis of natural gas. Unlike grey or blue hydrogen, this process releases solid (and not gaseous) carbon, which can be either used as feedstock for other industrial processes (without releasing it into the atmosphere as CO2 down the value chain) or stored permanently. On the other hand, electrolysis of water, an electro-chemical process of splitting water into oxygen and hydrogen using electric current, can be considered renewable if the electricity is sourced renewably, such as using hydro, wind or solar power (green hydrogen). This method currently accounts for only 4% of the world hydrogen production but it is predicted to expand rapidly to 22% by 2050 [10]. The so-called pink hydrogen is instead produced via electrolysis of water but using nuclear power. There are also natural stockpiles of 'white hydrogen' which can be extracted from drilling in underground wells. However, the endowments are negligible with compared to global needs. The research community has also developed other carbon neutral H2 production pathways, including photocatalytic hydrogen production, biomass and waste gasification and biological hydrogen production through biomass fermentation, etc. Some of these technologies are expected to mature and to enter commercial scale production by 2030 [7] and will boost the production of hydrogen through renewable routes.

1.2.2. Hydrogen applications in Transport Sector

Hydrogen powertrains mainly utilize two energy conversion technologies: hydrogen Fuel Cell and ICE. A FC, which converts hydrogen into electrical energy used for propulsion, is presently the more commercialized approach. A FC vehicle is reported to have a tank-to-wheel efficiency in the range from 31% to 36%, with water vapor being the only emission [11]. Toyota, Honda and Hyundai have already commercialized FC vehicles in selected markets, with more than 6500 units sold as of June 2018 [12]. On the other hand, the advantages of hydrogen ICE compared to the FC technology include a higher tolerance to fuel impurities, flexibility to switch between fuels, reduction of rare materials usage and a lower thermal load to be managed. In addition, H2-ICE technology benefits from the reduced cost of using the existing manufacturing facilities and processes for conventional ICEs [7]. The development of advanced hydrogen ICEs is still in the conceptual stage. Besides the activities of automotive manufacturers which are investigating the feasibility of hydrogen propelled vehicles through the development of several prototypes for both passenger cars and heavy-duty applications [13–15], a huge number of research projects is currently ongoing to identify the most attractive hydrogen powertrain

solutions [16]. As a matter of fact, scientific literature presents a wide range of possible H2 applications relying on either fuel autoignition [17], Dual Fuel concepts [18,19], or premixed combustion. In such a framework, Spark Ignition (SI) engines represent the most common solution with studies on both Port Fuel Injection (PFI) and Direct Injection systems. Despite DI configurations are able to achieve better performance thanks to the higher volumetric efficiency and the lower risk of abnormal combustion [20], the majority of hydrogen-fueled ICE prototypes use PFI system, benefiting from a straightforward conversion from existing gasoline engines. A proof-of-concept light-duty truck and 'microbus' powered by such hydrogen-fueled ICE was presented by Tokyo City University. It has to be noted that even with such a simple modification, an engine Brake Thermal Efficiency (BTE) of 30÷37% at medium load was reported [21], readily comparable with the current FC technology. On the other hand, the potential of DI system has been already demonstrated by BMW and its partners in 2009. A hydrogen DI system with up to 300 bar injection pressure has been developed and integrated into a Spark Ignition (SI) engine, achieving a maximum efficiency of 42%, paralleling diesel engines with turbocharging [7]. In light of the potential of hydrogen engine, Mazda has been developing a hydrogen rotary engine combining PFI and DI technology since 2006. This technology has been integrated into a sports-car model with an extended driving range of 649 km [22]. Eventually, Koch et al. [23] have proved that the revamping could be performed also with diesel engines since the spark plug can be installed in the cylinder head through the machining of the injector seat. Moreover, the presence of the Exhaust Gas Recirculation (EGR) loop, mandatory in the latest generation of compression ignition engines, may enable additional strategies to reduce pumping losses, NOx emissions, and the occurrence of abnormal combustion phenomena. In this framework, Punch performed virtual conversion in H2-ICE of a 3.0L multicylinder diesel engine architecture, demonstrating a potential peak efficiency of 42% [24].

1.2.3. Hydrogen properties

Hydrogen has unique physical and chemical properties, compared to the conventional fossil fuels widely used in the transportation sector, namely Compressed Natural Gas (CNG), gasoline and diesel, as shown in Table 1-1. One of the many advantages of using hydrogen in ICE as a clean alternative fuel is its zero carbon content. This means that carbon-based emissions, mainly CO, CO2 and soot, can be almost eliminated, leaving NOx as the only harmful combustion byproduct. Moreover, with a high Lower Heating Value (LHV), H2 can provide nearly three times as much energy by mass compared with other fossil fuels. From

the abnormal combustion perspective, the high values of both autoignition temperature and Research Octane Number (RON ≥ 130) of hydrogen can limit the knock likelihood. However, the low minimum ignition energy may strongly increase the risk of preignition, glow ignition, and backfiring in the case of external mixture preparation [20]. Moreover, the high diffusion coefficient of H2 leads to fast mixing with the induced air (compared to conventional fuels), which is beneficial for mixture homogenization, especially in the case of Direct Injection. At atmospheric pressure and 273 K, the density of hydrogen is an order of magnitude less than that of natural gas, due to its very low molecular weight. This leads to a significant challenge for the implementation of hydrogen ICE in on-road applications due to the limited vehicle space. Increasing storage pressure is required to increase hydrogen density and hence the volumetric energy content. For instance, hydrogen at 350 bar (i.e., a current standard supply pressure for hydrogen refueling) and 273 K can increase the gas density to ~31 kg/m^3. As for the quenching distance of hydrogen, it is small if compared to conventional hydrocarbon fuels, necessitating the development for a proper liner lubrication [25,26]. Moreover, higher temperature gradients near the combustion chamber walls can be expected, leading to increased combustion heat losses. Finally, it should be noted that utilizing hydrogen in ICEs may induce other safety concerns related to the on-board fuel storage and delivery system.

Table 1-1: Hydrogen properties [7]

Property	H2	CNG	Gasoline	Diesel
Carbon content [mass %]	0	75	84	86
Lower Heating Value [MJ/kg]	120	45.8	44.8	42.5
Density[a,b] [kg/m^3]	0.089	0.72	755	830
Stoichiometric air demand [-]	34.5	17.2	14.7	14.5
Minimum ignition energy[a,d] [mJ]	0.02	0.29	0.24	0.24
Autoignition Temperature [K]	858	813	623	523
Quenching distance[a,c,d] [mm]	0.64	2.1	2	-
Laminar Flame Speed [m/s]	1.85	0.38	0.4	0.4
Diffusion Coefficient[a,b] [m^2/s]	8.5x10^{-6}	1.9x10^{-6}	-	-

[a] at 1 bar, [b] at 273 K, [c] at 298 K, [d] at stoichiometry

For example, hydrogen embrittlement is a common cause of material failure when high pressure hydrogen is used [27]. Also, the high diffusivity of H2 indicates that hydrogen poses a high risk of leakage. These issues require special measures in the design of the vehicle and the fuel delivery system.

1.2.4. H2ICE: Operating modes and Aftertreatment systems

The main product of complete combustion of hydrogen with air is water vapor. However traces of carbon based emissions (CO, CO2 and HC) can be found in the exhaust gases. Their origin is generally attributed to the combustion or cracking of lubrication oil [28]. To oxidize these components, a catalytic converter needs to be implemented in the exhaust line. The critical pollutant specie for hydrogen engines is instead represented by nitrogen oxides, which form in the combustion chamber due to the high temperatures in combination with the presence of nitrogen (N2) from air. For homogeneous operation the amount of nitrogen oxides emissions created during combustion of hydrogen is heavily dependent on the composition of the fuel air mixture. Generally, as reported in Figure 1-3, exploiting ultra-lean mixture (i.e. lambda $\geq$ 2.8), the in-cylinder temperatures are sufficiently low as to avoid NOx formation [29]. By reducing the excess air, the nitrogen oxides emissions increase exponentially achieving a maximum between lambda 1.2 and 1.3. When approaching stoichiometric mixtures the NOx emissions decrease. If lean mixtures are exploited (1 < lambda < 2.8), NOx emission must be treated through a 'Diesel-like' aftertreatment system (ATS), which includes Oxidation Catalyst, Urea injector, single-stage Selective Catalytic Reduction (SCR) system and an Ammonia Slip Catalyst (ASC). However, the main limitation of this solution lies on packaging. In fact, its dimensions can be assumed proportional to the mass flow rate of NOx to be reduced. Therefore, when coupled to a high performance engine, the high air flow rates involved, in conjunction with a lean lambda between 1 and 2.2 (where NOx emissions are high), would demand for a too large ATS design. For this reason, a minimum limit of lambda 2.2 has been considered for the adoption of this type of aftertreatment system. Concerning the maximum load achievable, lean mixtures allow to significantly reduce the knock tendency, thus exploiting combustion anchor angles close to the optimum (i.e. 8-10 deg aTDCf), but make the power density very low, creating also huge challenges for the design of the charging system [30]. On the other hand, in stoichiometric conditions, the required boost pressure is lower but the power density achievable is significantly limited from knock and exhaust gas temperature. To mitigate knock as well as to protect the components at the exhaust, thus allowing to achieve high power levels, Water Injection Technology could be exploited. As for the aftertreatment system for

stoichiometric operations, a Three-Way Catalyst is adopted to oxidize the carbon based emissions coming from lubricant oil combustion. The same catalyst is also supposed to reduce the emitted nitrogen oxides using the unburned hydrogen as a reducing agent. Finally, a NOx trap is implemented at the end of the exhaust line to contain and reduce nitrogen oxides emitted when switching from ultra-lean to stoichiometric operations and the catalyst cannot guarantee a 100% conversion efficiency of NOx due to the lack a reducing agent (unburned hydrogen) [28].

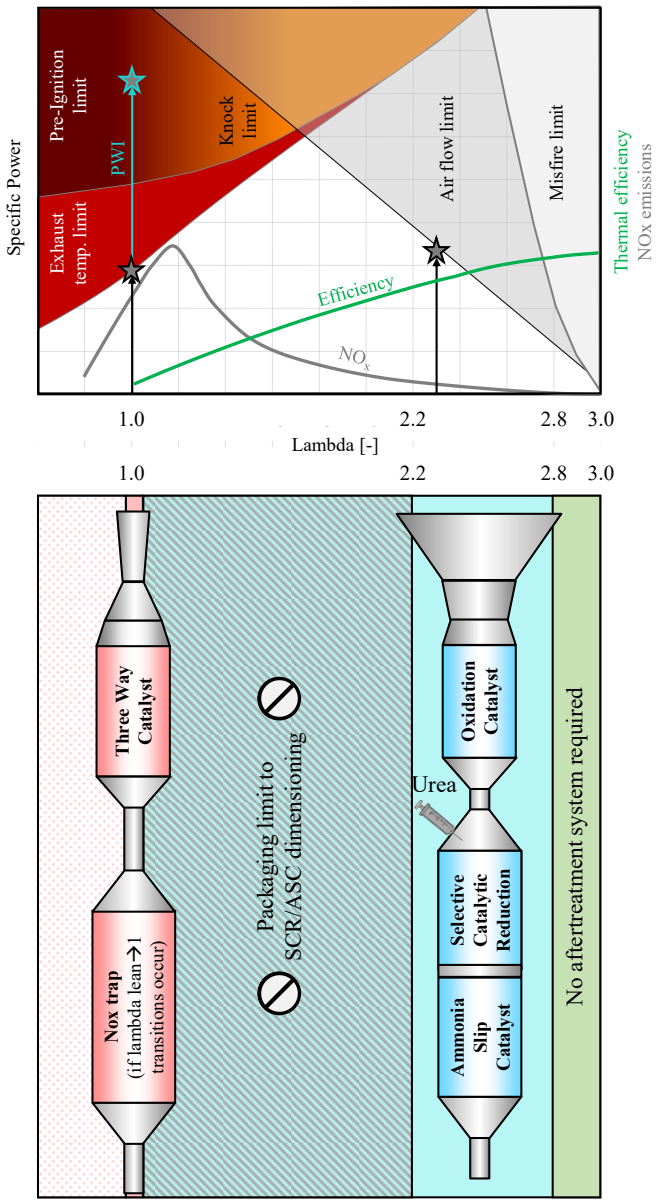


Figure 1-3: Schematic of hydrogen engine performance limits and operating modes

1.2 Scope of the Work

The scope of the work was to analyze the performance of a hydrogen fueled ICE revamped from a state-of-the-art 3.0L V6 120° Twin Turbocharged Direct Injection Spark Ignition engine, to optimize its parameters and to drive the preliminary design of its architecture. In this perspective, once outlined the full-load curve target to achieve, the first objective concerned the definition of the H2-ICE operating mode. According to Figure 1-3, the engine was supposed to run in ultra-lean conditions (lambda $\geq$ 2.8) at low loads. In this conditions, power output adjustment could be accomplished by solely varying the relative air/fuel ratio, which also minimizes losses caused by use of a throttle. For higher load demands, the engine switches from ultra-lean to stoichiometric operations, injecting water when necessary to mitigate knock and to control the exhaust gas temperature.

Afterwards, the focus of the activity shifted towards the analysis of Port Water Injection technology. Exploiting a huge set of experimental data collected on a small displacement gasoline engine in dry and wet conditions, the objective was to investigate in detail the knock mitigation potential of PWI technology as well as the effect of water content on combustion parameters. Moreover, once developed a 1D-CFD methodology to simulate PWI, the analysis was concluded assessing the potential CO2 emission reduction of the above-mentioned engine coupled with a B-segment Sport Utility Vehicle (B-SUV) achievable exploiting high Compression Ratio, Miller Cycle and PWI system, over different driving cycles.

Once acquired a solid background on Port Water Injection technology, the focus returned to the hydrogen engine. At this point, two objectives were set. The first one concerned the development of a 3D-CFD methodology devoted to understand H2 injection behavior and optimize the in-cylinder mixture preparation. The second one was related to a preliminary virtual H2-ICE architecture optimization through 1D-CFD simulations. To tackle this task, a methodology to simulate hydrogen combustion, together with a dedicated knock model and a virtual engine control unit, were developed. After defining the optimal combination of engine displacement, compression ratio and turbocharger with the aim to achieve the full-load performance target with the minimum water demand, the final goal was to generate the engine maps of the main operating parameters.

1.3 Document Content and Structure

This document is structured as shown in Figure 1-4: a comprehensive analysis of Port Water Injection technology is proposed in Chapter 2. Starting from a quasi-dimensional approach to model a PWI system integrated in a Downsized Turbocharged Direct Injection Spark Ignition engine, a virtual engine calibration methodology is proposed and the potential CO2 emission reduction achievable exploiting PWI system over different driving cycles is reported. In Chapter 3, the focus shifts towards a hydrogen-fueled ICE revamped from a high-performance 3.0L V6 120° Twin Turbocharged Direct Injection Spark Ignition engine. At first, a 3D-CFD methodology, developed to mimic hydrogen injection, is presented. Afterwards, a quasi-dimensional methodology to model a H2-ICE operation is described. Eventually, after performing a preliminary engine architecture optimization, the maps of the main engine operating parameters are generated and presented. A final summary of the work is reported in Chapter 4 of this manuscript.

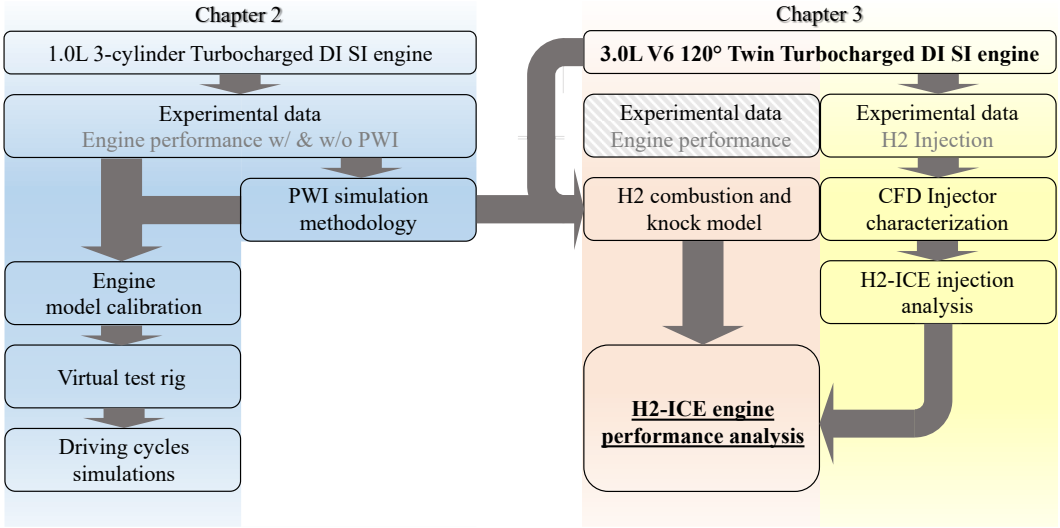


Figure 1-4: Schematic of manuscript structure

Chapter 2

Port Water Injection technology

2.1 Introduction

Water Injection (WI) is nowadays considered as one of the most promising solutions for knock mitigation in high performance engines. WI, taking advantage of the high latent heat of vaporization of the water introduced into the cylinders, allows an effective cooling of the charge, thus reducing knock tendency [31,32]. Moreover, thanks to the increase in the heat capacity of the charge, and to the reduction of the burn rate, the knock tendency can be further reduced, as demonstrated by Cazzoli et al in [34].

WI has been thoroughly examined in the last decade both through experimental and numerical activities [33]. Some researchers studied the fundamentals of water injection: both Cazzoli et al. [34] and Bozza et al. [35] analyzed the impact of water vapors on Laminar Flame Speed (LFS) and autoignition delay time, while Gern et al. [36] investigated the effect of water injection on Particulate Matter (PM) emissions. Several papers also compared the pros and cons of direct and indirect water injection strategies [37]. The latter, thanks to its simplicity and cost-effectiveness, seems to be the best candidate for series production [38]. Some studies focused on the optimization of the Port Water Injection system, paying particular attention on both spray targeting and injection timing which was demonstrated to play a key-role in reducing water consumption [39–41]. Millo et al. [42] investigated the issues related to both liquid film formation and oil dilution were discussed while Paltrinieri et al. [43] analyzed through both numerical simulation and experimental activities the effects on engine performance of several calibrations of a Port Water Injection system integrated in a single cylinder high specific power engine. The potential of PWI as an enabling technology to extend stoichiometric operation even at high load was also assessed in [44], with a significant reduction in the Indicated Fuel Consumption (ISFC). Also Wilson [45] estimated a considerable Brake Specific Fuel Consumption (BSFC) reduction coupling PWI and increased Compression Ratio.

Based on the above literature overview, 3D-CFD models proved to be very useful in better understanding and in predicting with high accuracy the influence of water on the in-cylinder phenomena [41,42]. Nevertheless, to point out possible synergies between WI and other promising technologies (such as high CR configuration and Miller cycle) a virtual test rig of the whole engine seems to be mandatory. As a result, several researchers exploited 1D-CFD models to tackle this task and to obtain a reliable prediction of the whole system behavior with reduced computational effort [41]. On the other hand, such approaches require simplified, but physically based sub-models that allow for a physically based reproduction of turbulence, combustion, wall film formation, heat transfer, Cycle-to-Cycle Variability (CCV) and knock phenomena. Only in this way, a preliminary engine calibration with an enhanced knock resistance can be numerically identified, together with realistically expected performance improvements. In this regard, Bozza et al. developed a methodology to model a WI system with the aim to generate BSFC maps of a downsized turbocharged two-cylinder engine under wet and dry operating conditions. The computed maps were then embedded in a vehicle model with the objective of estimating the potential CO2 reduction achievable through WI over a Worldwide harmonized Light-duty Test Procedure (WLTP) cycle [35,46] and to define the proper sizing of the water tank [47]. Nevertheless, a quasi-static approach [48] for the vehicle simulations may not be suitable to fully exploit the benefits of water injection. As a matter of fact, the highly dynamic conditions of real-world driving scenarios may be characterized by a significantly different knock probability with respect to stationary engine operations which, in turn, will lead to a wrong estimation of the water consumption. Based on the above considerations, this chapter aims to describe a comprehensive methodology to:

- model a PWI system integrated in a state-of-the-art Turbocharged Direct Injection Spark Ignition (T-DISI) engine [49];
- numerically identify an optimal engine calibration;
- assess, in different driving conditions, the potential CO2 emission reduction of a T-DISI engine integrated in a B-segment Sport Utility Vehicle (B-SUV) achievable exploiting high Compression Ratio, Miller Cycle and PWI system.

After a brief introduction on the experimental measurements, the main features of the numerical model, which was preliminary calibrated and validated in dry operating conditions, are described. Afterwards, the methodology for PWI modelling is presented and discussed in detail, in four sub-sections. The first describes the integration of the port-puddling model, which allows to properly

replicate transient phenomena of water wall film formation in the intake ports. The second focuses on the water evaporation model, calibrated with the aim to correctly account for the fraction of in-cylinder water that evaporates by absorbing heat from walls. The third examines the combustion model, which required a further refinement in order to accurately predict the effects of water vapors on the burn rate. The last sub-section reports the PWI model validation. Subsequently, a description of the methodology to optimize the Water Injection strategy and the Intake Valve Lift profiles is provided. Eventually, the vehicle simulation results obtained for different type approval and RDE driving cycles are summarized in a last section, highlighting potential CO2 emission reduction of high Compression Ratio, Miller Cycle and PWI system in the range of 4-8% with a still acceptable water consumption (lower than 1.1 l/100km).

2.2 Case study

The research activity described in Chapter 2 is carried out on a state-of-the-art 3-cylinder Turbocharged Direct Injection Spark Ignition engine, which has been reported in Figure 2-1. The engine features a total displacement of 1.0L and it is equipped with an electro-hydraulic Variable Valve Actuation (VVA) MultiAir system on the intake side [50]. Four different configurations were taken into account as reported in in Table 2-1.

Configuration 1 is the reference and it represents the normal production engine layout, while in configuration 2 the Compression Ratio (CR) is increased up to 13 for efficiency maximization. In this case, Miller strategy with Late Intake Valve Closing (LIVC) is exploited to reduce the knock likelihood and the exhaust gas temperature at low and high engine speed respectively. However, despite a LIVC strategy, configuration 2 is not able to guarantee the same performance of the reference variant in terms of brake power: the higher compression ratio implies a higher knock propensity and a consequent delayed combustion, which has a detrimental effect on the thermodynamic efficiency. This results in a higher air flow demand, which the compressor is not able to satisfy. To preserve the original power output, configuration 3 and 4 are equipped with a Port Water Injection system.

The above-described engine equips a B-SUV vehicle through a 6-speed manual transmission. The main specifications of the vehicle are outlined in Table 2-2 as a function of the driving conditions.



Figure 2-1: 3-cylinder 1.0L Turbocharged Direct Injection Spark Ignition engine – GSE T3 [51]

Table 2-1: GSE T3 Engine specifications

Specification	Conf. 1	Conf. 2	Conf. 3	Conf. 4
N. of cylinders [-]	3	=	=	=
Displacement [cm^3]	999	=	=	=
Bore [mm]	70	=	=	=
Stroke [mm]	86.5	=	=	=
Compression Ratio [-]	10.5	13	=	=
VVA System	Baseline	LIVC	LIVC	LIVC opt.
Injection System	GDI	=	=	=
Full rated power [kW]	88 at 5500 RPM	75 at 5500 RPM	88 at 5500 RPM	88 at 5500 RPM
Full rated torque [N-m]	190 at 2000 RPM	170 at 2000 RPM	190 at 2000 RPM	190 at 2000 RPM
PWI	No	No	Yes	Yes

Table 2-2: Main vehicle characteristics for the NEDC, WLTC, FTP75, Artemis Motorway cycle, RDE, RTS95 and US06

Parameter	Unit	NEDC	Other driving cycles
Vehicle Mass	kg	1470	1630
Rolling Radius	m	0.333	0.333
Power demand at 100 km/h	kW	18	20.5
Electrical load (engine on)	W	220	400
Electrical load (engine off)	W	120	120

2.2.1 Experimental measurements

For the experimental campaign the engine was installed on the test bench in its standard configuration. It was equipped with 3 piezoelectric pressure transducers integrated in the spark plugs to detect in-cylinder pressure signal within each cylinder. A linear lambda sensor was mounted downstream of the turbine to measure the relative Air-to-Fuel ratio. Furthermore, several piezo-resistive pressure transducers and K-type thermocouples were used to monitor pressure and temperature along both intake and exhaust lines.

The water used for the experiments was de-ionized distilled water stored in a tank at 25°C. As depicted in Figure 2-2, a recirculating pump delivered water at a pressure of 6 bar to the rail, which in turn was connected to three injectors, which were located in the intake runners, one for each cylinder.

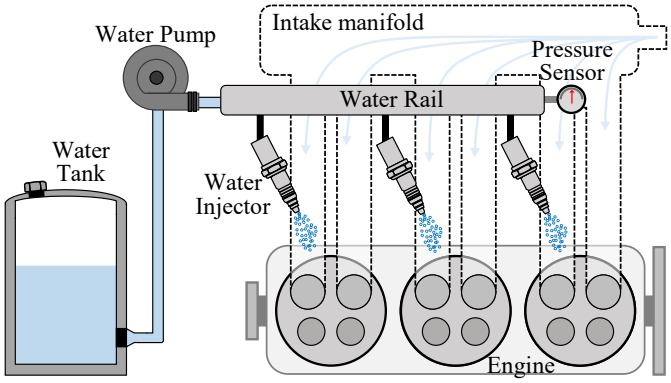


Figure 2-2: Schematic layout of Port Water Injection system

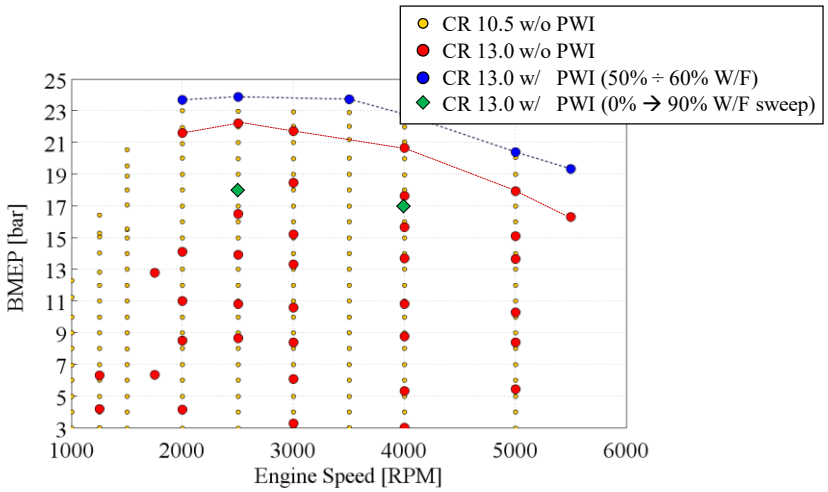


Figure 2-3: Experimental test matrix

During all the tests, the engine was operated at stoichiometric Air-to-Fuel ratio and was fueled with a RON 95 gasoline having a LHV of 42.5 MJ/kg. Furthermore, water injection timing was kept constant with an End of Injection (EOI) equal to 360 Crank Angle degree (i.e. equal to gas exchange Top Dead Center). For all measurements, experimental data were recorded and evaluated over 300 consecutive engine cycles, in order to gather a significant statistical sample for knock-limited spark advance operating conditions, where few percent of engine cycles are typically knocking.

A summary of the experimental campaign is shown in Figure 2-3. The engine was primarily tested in its standard configuration 1 to define the engine reference performance (orange circles). The tests were then repeated with the increased compression ratio (conf. 2, red circles). In this case, the engine was not able to guarantee the same full-load performance of the standard configuration. At low engine speed, the higher compression ratio implied a high knock propensity, forcing the combustion anchor angle (MFB50) to be delayed up to a maximum of 30 deg aTDCf: not being enough, the boost pressure was reduced through the wastegate valve in order to control knock. At higher engine speed, knock was still present and the delayed combustion had a detrimental effect on the engine thermodynamic efficiency. This resulted in a higher air flow demand, which the compressor was not able to satisfy.

Afterwards the impact of WI on the combustion was assessed on configuration 3 through two sensitivity analyses on the Water-to-Fuel (W/F) ratio at 2500 RPM - 18 bar Brake Mean Effective Pressure (BMEP) and at 4000 RPM – 17 bar BMEP (green rhombuses). Finally, the increase in engine performance enabled by PWI

knock suppression capabilities were assessed at Wide Open Throttle (WOT) exploiting Water-to-Fuel ratios between 50% and 60% (blue circles, blue dashed line).

2.3 Numerical Set-up

At first, a detailed 1D-CFD model of the reference engine was built by means of GT-POWER^{TM}, a one-dimensional fluid-dynamic code developed by Gamma Technologies Inc. for engine performance simulation. In particular, a simple injector model was adopted to control the injected fuel mass in order to guarantee a stoichiometric combustion. Concerning water injection, it was performed via multiple profile injectors connected to the intake runners, while the injected water mass was imposed equal to the experimental one. A model-based controller was then introduced to actuate the wastegate opening position in order to match the experimental boost pressure.

After a thorough calibration of the gas-exchange processes, a predictive combustion model, the so-called SITurb [52,53], was implemented in the code for the prediction of the burn rate at various operating conditions. Knock detection was instead accomplished through a Kinetics-Fit model, which was tuned on the basis of a CCV-replicating model.

The following paragraphs contain a detailed description of SITurb, CCV and Knock model calibration processes, which were carried out considering only the experimental tests without the Port Water Injection system.

2.3.1 Calibration of the combustion model

Following a well-assessed hierarchical 1D/3D approach, as a first step a turbulence sub-model was calibrated on the basis of 3D-CFD results obtained at various valve strategies and engine speeds [54]. The second step of the tuning procedure concerned the optimization of the SITurb combustion model constants. The main characteristics of the SITurb model are briefly summarized in the following sub-section. More details can be found in [52,53].

SITurb model

The entrained mass (M_e) rate of the unburned air-fuel mixture in the flame front is dependent on the flame area (A_f), the unburned gas density (ρ_u) and the sum of the Turbulent and Laminar Flame Speeds, as expressed by Equation 1:

$$\frac{dM_e}{dt}=\rho_u A_f(S_T+S_L) \tag{1}$$

S_T, namely the Turbulent Flame Speed, is calculated through Equation 2, where R_f, u' and L_t are respectively flame radius, turbulent intensity and turbulent length scale.

$$S_T=C_S \cdot u' \left(1-\frac{1}{1+\frac{C_k \cdot R_f^2}{L_t^2}} \right) \tag{2}$$

In Equation 2, two calibration parameters are present: the Flame Kernel Growth Multiplier (C_k), which scales the flame front evolution, and the Turbulent Flame Speed Multiplier (C_S), which globally scales the Turbulent Flame Speed.

A further calibration parameter, the Dilution Effect Multiplier (C_D), is instead adopted to tune the effect of diluents such as exhaust residuals, EGR or water on the Laminar Flame Speed (S_L), which is calculated by Equation 3:

$$S_L=\left(B_m+B_\phi(\phi-\phi_m)^2\right)\left(\frac{T_u}{T_0}\right)^\alpha\left(\frac{p}{p_0}\right)^\beta\left(1-0.75 \cdot C_D \cdot (1-(1-0.75 \cdot C_D \cdot [D_i])^7)\right) \tag{3}$$

where ϕ is the in-cylinder equivalence ratio, T_u is the temperature of the unburned gas, p is the in-cylinder pressure, D_i is the mass fraction of the diluents in the unburned zone and ϕ_m is the equivalence ratio at maximum speed. B_m, B_ϕ, T_0, p_0, α and β are model constants.

Finally, Equation 4 is used to determine the burn rate of the entrained unburned mass (M_u):

$$\frac{dM_b}{dt}=\frac{M_u}{\tau}=\frac{M_e-M_b}{\tau} \tag{4}$$

where τ is assumed to be the time needed by the Laminar Flame Speed to cover the Taylor Microscale (λ_T) of turbulence, expressed by Equation 5.

$$\tau = \frac{\lambda_T \cdot C_\lambda}{S_L} \tag{5}$$

C_λ, the Taylor Length Scale Multiplier, is a further calibration parameter inversely proportional to the burnup rate.

SITurb model calibration results

Six engine operating points at Full-Load, the ones shown with red circles connected by a red dashed line in Figure 2-3, were chosen for the tuning of the previously described four SITurb calibration parameters.

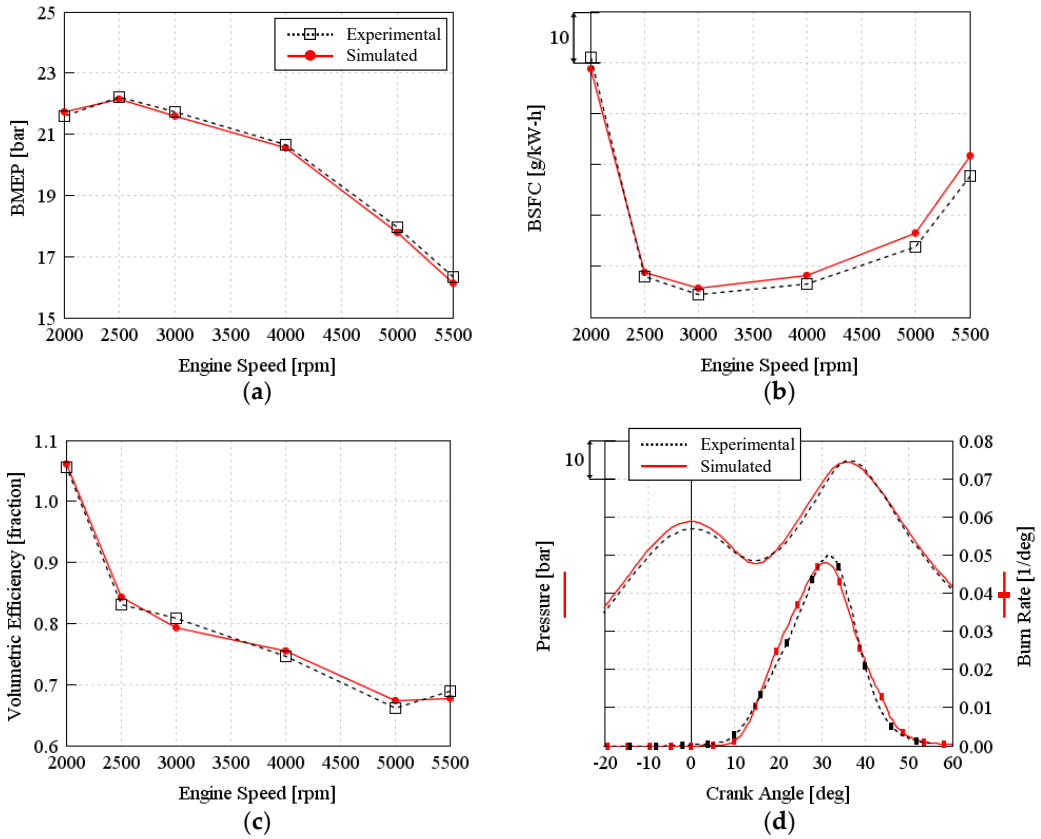


Figure 2-4: (a) Brake Mean Effective Pressure (b) Brake Specific Fuel Consumption (c) Volumetric Efficiency (d) Pressure Cycle (left) and Burn rate (right) at 3000 RPM obtained at Full-Load operating conditions without Port Water Injection; simulated (red solid line) and experimental (black dashed line)

Table 2-3: Optimized values of the calibration parameters of the SITurb combustion model

Calibration parameter	Value
C_k	4.112
C_S	0.625
C_λ	0.789
C_D	0.872

By imposing the experimental spark timing, a Design of Experiment (DoE) methodology, integrated with a Genetic Algorithm optimum search, was used to identify the best set of SITurb constants aimed at minimizing the error between experimental and predicted burn rates for the selected operating conditions [54]. Once the optimal SITurb calibration parameters have been defined (see Table 2-3), the results of the complete engine model were compared with experimental data in order to assess its accuracy and reliability. The values of BMEP, BSFC and Volumetric Efficiency, depicted in Figure 2-4a, b, and c respectively, highlight a very good agreement with an error below 2%. Moreover, also the simulated pressure cycle and burn rate profile reported in Figure 2-4d show a satisfactory correlation with experimental measurements.

2.3.2 Calibration of CCV model

Since knock is heavily dependent on Cycle-to-Cycle variability (CCV), its occurrence cannot be predicted by analyzing the average cycle only. However, to physically reproduce the CCV, it would be necessary to accurately model the stochastic behavior of in-cylinder charge motion, the local inhomogeneities of the Air-to-Fuel ratio inside the cylinder, etc. as discussed in detail in [55]. As a result, the adoption of a 0D phenomenological combustion model does not allow a rigorous modelling of CCV, which instead must be "injected" into the model using a statistically-based approach [56]. In this research work, the GT CCV model [53] developed by Gamma Technologies was adopted. Such an approach, after the simulation of some preliminary cycles to achieve the convergence of the flow solution, perturbs two variables of the SITurb combustion model, namely the Turbulent Flame Speed Multiplier C_S and the Taylor Length Scale Multiplier C_λ, for 300 cycles in a row. C_S and C_λ assume random values from Gaussian distributions whose standard deviations represent the calibration parameters of the CCV model. Similarly to the approach adopted for SITurb calibration, a DoE methodology integrated with a Genetic Algorithm optimum search was used to calculate the standard deviations of C_S and C_λ that minimized the error between experimental and simulated Coefficient of Variation (COV) of the Indicated Mean

Table 2-4: Optimized values of the calibration parameters for the CCV model

Calibration parameter	Value
Standard deviation for C_S	0.048
Standard deviation for C_λ	0.167

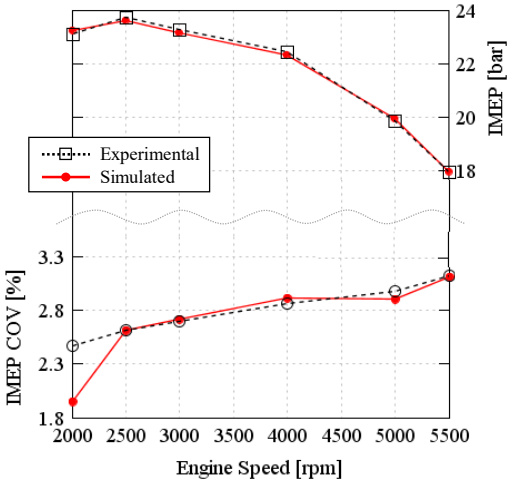


Figure 2-5: Coefficient of Variation of the Indicated Mean Effective Pressure (top) and average Indicated Mean Effective Pressure over 300 CCV-cycles (bottom) at Full-Load without PWI; simulated (red solid line) and experimental (black dashed line)

Effective Pressure (IMEP) (see Table 2-4). Afterwards, the average IMEP and its COV resulting from the CCV-run were compared against experimental outcomes. As it can be seen in Figure 2-5, the CCV model provides a good estimation of these quantities for almost the entire engine speed range, with the only exception of the 2000 RPM operating condition, for which the simulation underestimates the COV.

2.3.3 Knock model

Most of the model developed for knock prediction are based on the approach proposed by Livengood and Wu [57] which states that the autoignition of the end gas occurs when the Knock Induction Time Integral (KITI) achieves the value of 1, as described by the following equation:

$$\mathrm{KITI} = \int_{t=0}^{t_{knock}} \frac{1}{\tau} dt = 1 \qquad (6)$$

where τ is the induction time of the Air-Fuel mixture, $t=0$ can be associated to the Intake Valve Closing (IVC) instant and t_{knock} is the time corresponding to the autoignition instant of the unburned gas (computed from the start of compression).

Several empirical relationships for induction time (τ) calculation have been developed in the scientific literature [58–60]. Most of them, however, do not take into account induction time dependence from mixture composition in terms of diluents, such as water, and are not capable to reproduce the Negative Temperature Coefficient (NTC) behavior [56]. For these reasons, the so-called Kinectics-Fit model, proposed by Gamma Technologies [53], was preferred for this work; it calculates the induction time on the basis of equation 7:

$$\tau = \mathbf{M_1} \cdot a \left(\frac{ON}{100}\right)^{b} [Fuel]^{c}[O_2]^{d}[D_i]^{e} \exp\left(\frac{f}{\mathbf{M_2} T_u}\right) \quad (7)$$

where ON is the fuel Octane Number, [Fuel] and $[O_2]$ are the concentrations in [mol/m3] of fuel and oxygen respectively; T_u is the temperature of the unburned gas; $[D_i]$ is the sum of N_2, CO_2, and H_2O concentrations in [mol/m3]. The knock Induction Time Multiplier (M_1) and the Activation Energy Multiplier (M_2) are the knock calibration parameters while quantities from 'a' to 'f' are model constants.

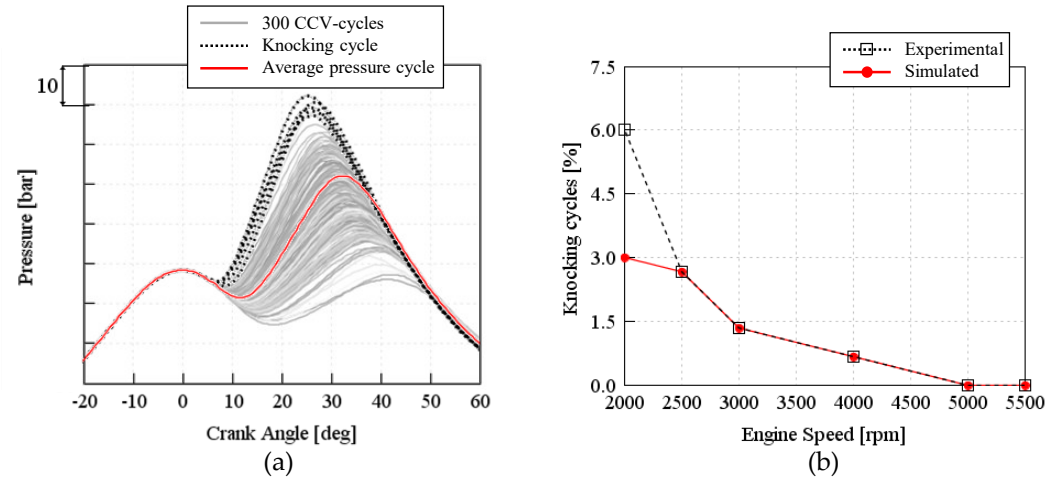


Figure 2-6: Example of CCV simulation (a) and comparison between simulated (red solid line) and experimentally measured (black dashed line) knocking cycles percentage over 300 CCV-cycles at Full-Load without PWI (b).

Table 2-5: Optimized value of the calibration parameters for the Knock model

Calibration parameter	Value
M_1	0.860
M_2	0.916

After the set-up of the artificial CCV model described in the previous section, which allowed to simulate the cycle to cycle variability as shown in Figure 2-6a, the knock model was calibrated through a Genetic Algorithm optimum search. M_1 and M_2 were tuned so that the percentage of knocking cycles detected by the model during the 300 CCV-cycles was coincident to the experimental one (see Table 2-5). Optimization results are presented in Figure 2-6b. The Knock model demonstrated the capability to reproduce the experimental knocking behavior, with the exception of the operating point at 2000 RPM. This is the direct consequence of CCV-model, which underestimates IMEP COV at 2000 RPM (see Figure 2-5), thus underestimating the knock likelihood.

2.4 Port Water Injection Model

In this section, the numerical approach adopted for the modelling of Port Water Injection system is presented and discussed in detail, in three sub-sections. The first describes the integration of the port-puddling model, which allows to properly replicate transient phenomena of water wall film formation in the intake ports. The second focuses on the water evaporation model, calibrated to discern the water amount that is directly participating in the charge cooling from that which is evaporating on the walls. Finally, the last sub-section examines the SITurb combustion model, which requires a further refinement in order to accurately describe the effect of water vapor on the burn rate.

The calibration of the PWI model has been carried out considering the experimental outcomes obtained at the operating points of 2500 RPM – 18 bar BMEP and 4000 RPM – 17 bar BMEP, shown in Figure 2-3 with green rhombuses.

2.4.1 Port-Puddling model

A particular model capable to reproduce the formation of a water wall film was adopted for the intake ports downstream of water injectors. Afterwards, with the aim of describing the roles that water performs during each cycle, the following mass balance equation was introduced:

$$m_{inj}^{(n)} + m_{back}^{(n-1)} = m_{film}^{(n)} + m_{trap}^{(n)} + m_{back}^{(n)} \quad (8)$$

As represented in Figure 2-7, the entire water mass injected at cycle ‘n’ ($m_{inj}^{(n)}$) temporarily becomes part of the wall film. Subsequently, the code models the building-up of the liquid film, along with its evaporation and transportation under

the action of shear forces generated by intake air flow (see Figure 2-7a). The modelling of such process is achieved by the following two parameters: the Circumferential Extent of Wall Wetting (CEWW) and the Puddle Velocity Multiplier (PVM). The first one, as shown in Figure 2-7a, defines the fraction of the intake port circumference that is covered by the water puddle: higher values imply a greater amount of water that can be retained by the wall film. On the other hand, PVM represents a multiplier to increase or decrease the effect of shear stresses on the transportation of the water puddle: higher values of PVM cause lower amount of water to be trapped in the wall film.

It follows that just a fraction of the injected mass ($m_{inj}^{(n)}$) remains trapped in the wall film ($m_{film}^{(n)}$), while the remaining part escapes from the film and enters into the cylinder. Once reached the combustion chamber, the liquid water starts evaporating by extracting heat either from the surrounding air or from the cylinder walls. Afterwards, some vapor can flow back into the intake ports ($m_{back}^{(n)}$) due to the LIVC. $m_{back}^{(n)}$, as vapor, does not become part of the liquid film and it gets entrained in the cylinder during the following cycle. Finally, $m_{trap}^{(n)}$ represents the amount of water which is present in the cylinder during the combustion process.

With the aim of characterizing the evaporation process of the injected water, an index was defined through 3D-CFD simulations [42]. Such index, as described by Equation 9, represents instant by instant the ratio between the mass of water vapor into the cylinder ($m_{H_2O,evap}$) and the maximum amount of water theoretically available at each engine cycle, that is the sum of the injected water during cycle 'n' ($m_{inj}^{(n)}$) and of the backflow water from the previous cycle 'n-1' ($m_{back}^{(n-1)}$).

$$\text{Evaporation Index (EI)} = \frac{m_{H_2O,evap}}{m_{inj}^{(n)} + m_{back}^{(n-1)}} \tag{9}$$

Figure 2-8 reports an example of Evaporation Index computation: after IVO, entrained water mass produces a subsequent growth of EI; then, from Bottom Dead Centre (BDC) on, a reduction of EI is observed as a consequence of the high water backflow generated by the Miller cycle (Late Intake Valve Closing). The Evaporation Index, due to the building-up of the wall film, varies from cycle to cycle and achieves its highest value, 1, when the wall film is saturated and all the injected water enters into the combustion chamber.

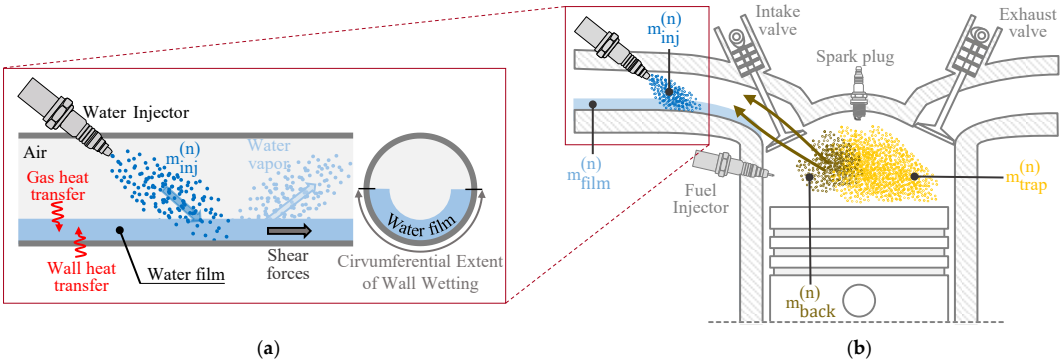


Figure 2-7: Schematic representation of (a) port-puddling model (b) injected water behavior

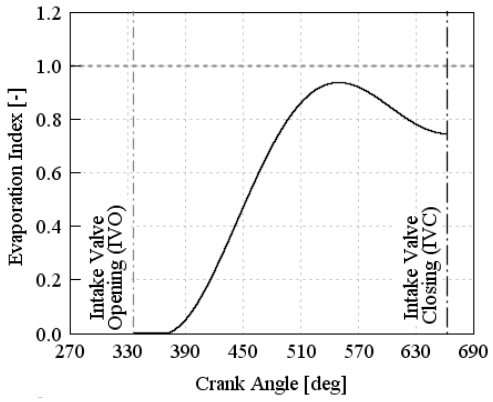


Figure 2-8: Example of Evaporation Index as a function of Crank Angle (CA)

To carry out the calibration of the water wall film model, the results of a previous work of the authors were considered [30]: in particular, the Evaporation Indexes computed for three different values of Water-to-Fuel ratios, namely 9%, 18% and 50%, at the operating point 4000 RPM - 17 bar BMEP, were taken as reference. Such calculations showed that the higher the mass of water injected, the higher the fraction retained by the wall film. Moreover, as depicted in Figure 2-9a by dashed lines, none of the computed indexes reached the maximum value of 1: indeed they were recorded during the 3rd cycle in a row of Port Water Injection and therefore during the building-up of the liquid film.

To replicate the 3D-CFD Evaporation Indexes, the water wall film model required a calibration process which was carried out through a DoE methodology. In particular, for each Water-to-Fuel ratio, the optimal pairs of CEWW and PVM aimed at minimizing the error between 1D-CFD and 3D-CFD Evaporation Indexes were found out. Solid lines of Figure 2-9a represent the results of the refined water

wall film model, while Figure 2-9b reports the values of its calibration parameters as a function of the total mass of injected water per cylinder.

Considering the operating point 4000 RPM - 17 bar BMEP and a Water-to-Fuel ratio of 50%, the different roles of the injected water were analyzed as a function of the consecutive engine cycles with PWI (see Eq. 8), as depicted in Figure 2-10a.

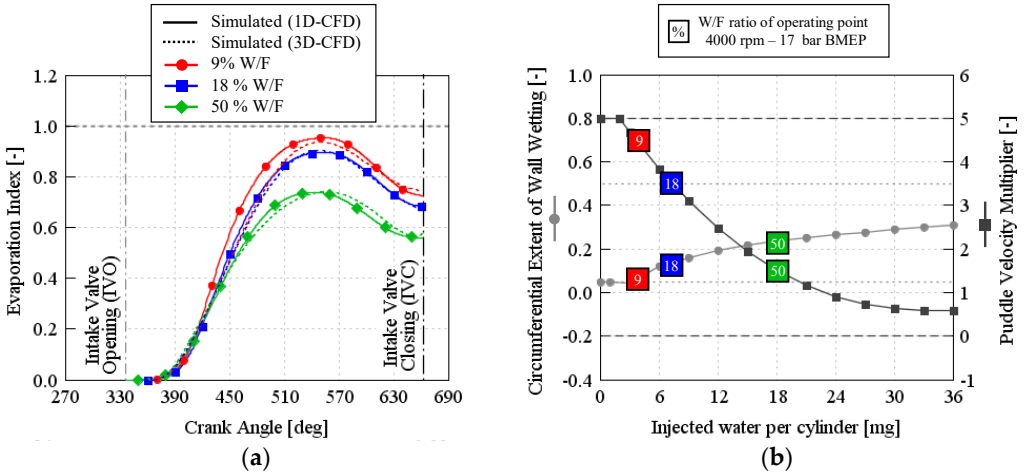


Figure 2-9: (a) Evaporation index measured during the 3rd cycle in a row of PWI at 4000 RPM – 17 bar for Water-to-Fuel ratios of 9% (red line), 18% (blue line) 50% (green line); 1D simulation (solid line), 3D simulation (dashed line); (b) Optimized values of the calibration parameters for the port-puddling model as a function of the total injected water per cylinder

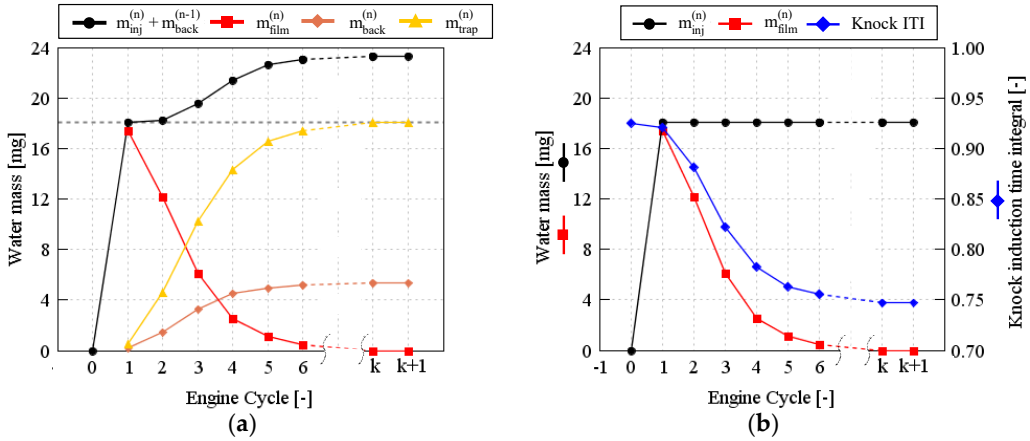


Figure 2-10: (a) The amount of water available before IVO, water trapped in the wall film, water backflow and water which is present into the cylinder during the combustion process as a function of the consecutive engine cycles with PWI; (b) The amount of injected water, trapped water in the wall film and the knock induction time integral as a function of the consecutive engine cycles with PWI; k ≥ 13 cycles

Figure 2-10b shows instead the impact of the water wall film formation on PWI effectiveness in reducing knock tendency. It can be noticed that during the first cycle of port water injection, almost all injected water remains trapped in the wall film (Figure 2-10a), and therefore knock likelihood is not reduced (Figure 2-10b). On the other hand, after 6 cycles, film building-up is almost complete and practically all the injected water gets trapped into the cylinder, thus effectively diminishing knock tendency. Therefore, it can be stated that the PWI system, at the operating point 4000 RPM - 17 bar BMEP and with a Water-to-Fuel ratio of 50%, becomes fully effective after 6 cycles of water injection. In steady state conditions, represented in Figure 2-10a and 9b by cycles 'k' and 'k+1', the fraction of injected water mass that gets trapped in the wall film is null (i.e. the amount of water that enters the film is equal to that which comes out). Moreover, the backflow water of cycle 'n-1' is equal to the one of cycle 'n'. It follows that, in steady state conditions, the amount of water that takes part to the combustion process ($m_{trap}^{(n)}$) is equal to the injected water ($m_{inj}^{(n)}$).

2.4.2 Evaporation model

The engine model governs the water vaporization within the cylinder through a simple phenomenological evaporation model. However, a detailed investigation to quantify the charge cooling effect produced by the phase change of water needs to be carried out. As a matter of fact, when entering the cylinder, the water droplets can impact on either the piston or the liner, thus extracting the heat requested for evaporation from the walls instead of the surrounding gases. The share between these contributions can be tuned through a parameter known as Fraction of Vaporized Heat Taken from Walls (FHW). The latter accounts for the fraction of water whose vaporization occurs on the cylinder walls rather than within the cylinder gases. As shown in Figure 2-11a and Figure 2-11b, where the in-cylinder temperature at Intake Valve Closing (IVC) and the Volumetric Efficiency are respectively reported, an excessively low value of FHW implies a larger amount of heat adsorbed from surrounding air, thus inducing a significant in-cylinder gases cooling with a consequent overestimation of the Volumetric Efficiency with respect to experimental measurements. The increase of FHW improves the calculation of engine airflow: however, a constant value for this parameter did not ensure a satisfactory correlation between numerical and experimental Volumetric Efficiency. Therefore, considering the operating point 4000 RPM – 17 bar BMEP, the FHW was optimized as a function of the total amount of liquid water that enters the cylinder, with the objective to match the experimental air flow rate (Eq. 10).

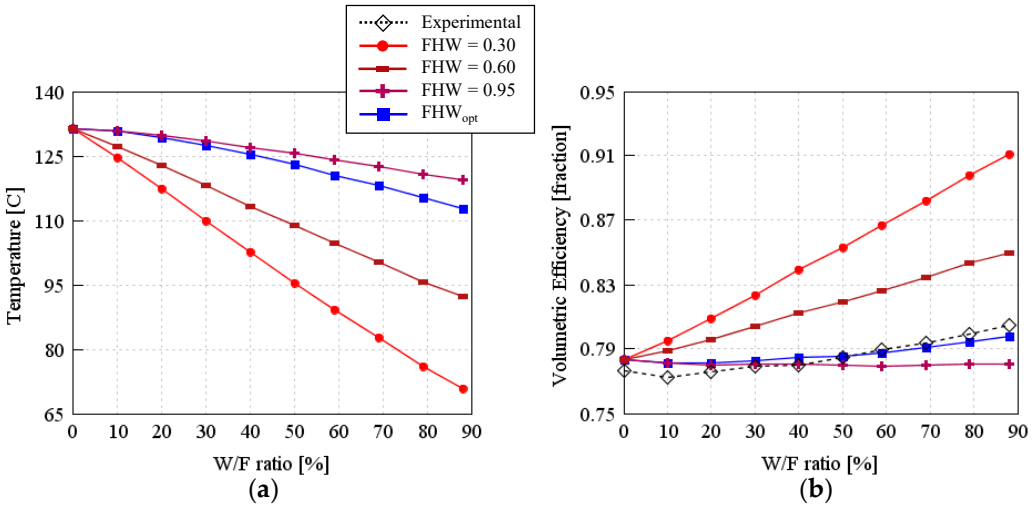


Figure 2-11: (a) In-cylinder temperature measured at IVC and (b) Volumetric Efficiency as a function of the Water-to-Fuel ratio for different values of the FHW model calibration parameter; operating point 2500 RPM – 18 bar

$$FHW_{opt}=0.95-0.0028\cdot\int \dot{m}_{H_2O,liq}\,dt \qquad (10)$$

where $\dot{m}_{H_2O,liq}$ represents the instantaneous mass flow rate of liquid water that passes through the intake valves of a single cylinder.

From Equation 10 it was noticed that, considering a 10% Water-to-Fuel ratio, only around 6% of in-cylinder liquid water vaporizes within the cylinder gases. Furthermore, such percentage rises along with the increase of the injected water and achieves a value around 15% with a Water-to-Fuel ratio equal to 90%. In accordance with previous findings [41,43,44], these results evidence a poor efficiency of PWI system in reducing the charge air temperature.

The robustness of Equation 10, which was defined for the operating point 4000 RPM – 17 bar BMEP, was assessed at the operating point 2500 RPM – 18 bar BMEP. As depicted by the blue solid line of Figure 2-11, the FHW optimization limits the reduction of in-cylinder temperature produced by the increase of the injected water, allowing to correctly reproduce the experimental Volumetric Efficiency for any Water-to-Fuel ratio.

2.4.3 Water dilution effect

Despite replicating the experimental values of boost pressure, spark timing, lambda and intake airflow, the engine model was not capable to satisfactorily

predict the evolution of the combustion process when water was injected. In particular, the higher the water content, the higher the deviation from experimental results: this trend is evident when observing Figure 2-12a, where both the center of gravity of the combustion and the in-cylinder pressure peak (p_{max}) are reported. This error was attributed to an incorrect estimation of the Laminar Flame Speed, the only parameter involved in burn rate calculation which depends on the in-cylinder mass fraction of water (see eq. 1 and 3). As claimed by several authors [34,46,61], the water dilution of the air-fuel mixture drops the S_L, thus delaying the combustion duration. This effect, governed in the SITurb model by the C_D (see Equation 3), seems to be underestimated, thus resulting in a more advanced MFB50 (Crank Angle corresponding to 50% of fuel burned) and a consequently higher in-cylinder pressure peak. Based on the above considerations and similarly to the approach used for FHW, C_D was calibrated as a function of the total amount of in-cylinder water vapor present at spark timing, in order to minimize the error on the prediction of the combustion center of gravity. FHW optimization, carried out at operating point 4000 RPM – 17 bar BMEP, led to definition of Equation 11:

$$C_{D,opt}=0.872+0.0062\cdot\{m_{trap}[mg]\} \quad (11)$$

As expected, Equation 11 shows that the greater the water content, the higher the optimal C_D and therefore the impact on S_L slowing, as claimed by the scientific community. It is worth to remember that, at steady state conditions, the amount of water that takes part to the combustion process (m_{trap}) is equal to the amount of injected water, as already described in '*2.4.1 Port-Puddling model'.*

The robustness of Equation 11 was then assessed at the operating point 2500 RPM – 18 bar BMEP: by observing the green line of Figure 2-12a, the C_D optimization led to MFB50 and maximum in-cylinder pressure values well correlated with the experimental results for the entire Water-to-Fuel ratio sweep, with errors lower than 2%. Moreover, also the simulated pressure cycle and the burn rate profile reported in Figure 2-12b for a 90% W/F show a satisfactory correlation with experimental measurements.

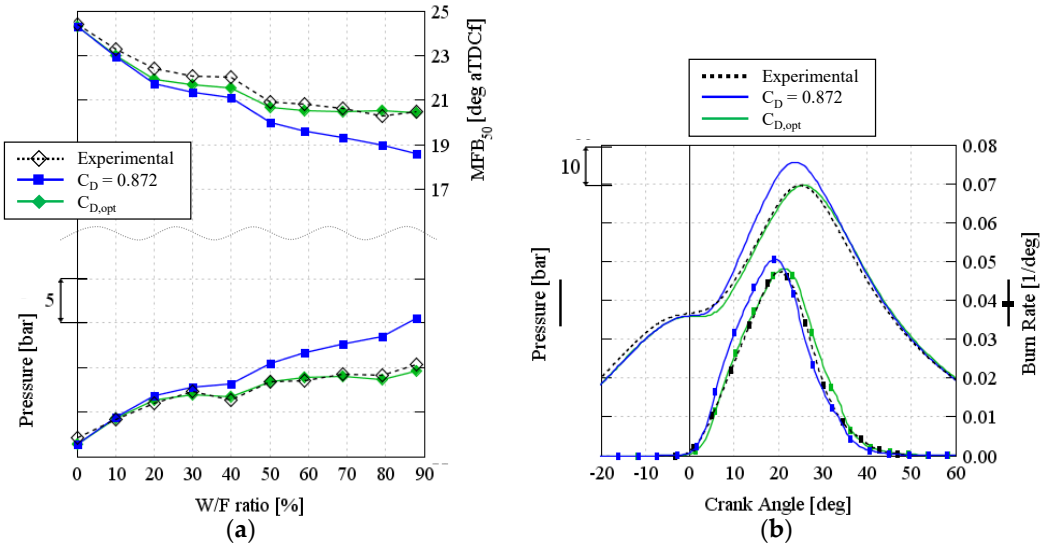


Figure 2-12: (a) Crank Angle corresponding to 50% of fuel burned (top), and maximum in-cylinder pressure (bottom) as a function of the Water-to-Fuel ratio; (b) Pressure Cycle (left), and Burn Rate (right) for a Water-to-Fuel ratio of 90%; operating point 2500 RPM – 18 bar; simulated (solid lines) and experimental (black dashed line)

2.4.4 Port water injection model validation

In this section, the engine model validation against the experimental tests carried out at WOT with PWI is presented and discussed.

At first, FHW_{opt} and $C_{D,opt}$ equations together with the port-puddling model were implemented in the engine model calibrated in dry conditions (see '*2.3 Numerical Set-up*'). Knock model and CCV model were not modified. The latter, which is not predictive, was kept unchanged since all the experimental tests carried out with water injection evidenced only a quite moderate increase in IMEP COV (see Figure 2-13).

Afterwards, by imposing the experimental boost pressure and by controlling the injected fuel mass in order to guarantee stoichiometric combustion, the experimental amount of water mass was injected in the intake runners. Subsequently, by simulating a significant number of engine cycles with the CCV model enabled, the spark timing was adjusted in order to achieve the same percentage of knocking cycles observed at Full-Load without PWI (see the red solid

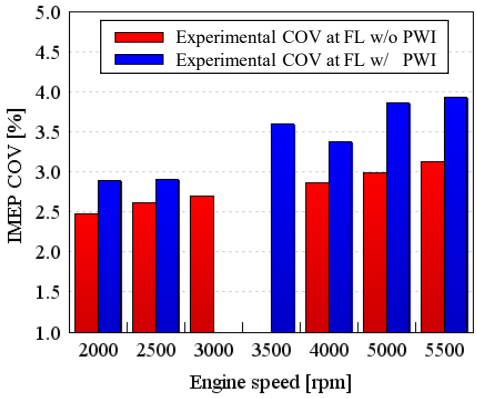


Figure 2-13: Experimental Coefficient of Variation of the Indicated Mean Effective Pressure at Full-Load in dry (red bars) and wet (blue bars) conditions

line of Figure 2-6b). Since engine performance at 5000 RPM and 5500 RPM were not knock limited (see Figure 2-6b), such analysis focused on the engine speed range 2000 – 4000 RPM.

The predicted Knock Limit Spark Advance (KLSA), BMEP as well as pressure cycles and the burn rates, which for the sake of conciseness have been presented only at 4000 RPM, showed a very good agreement when compared to the experimental results (see Figure 2-14a, b and c respectively). The error around 4% obtained in estimating the engine load at 2000 RPM – Full-Load with PWI was attributed to a knock tendency underestimation. Such error, already evident in Figure 2-6b, allowed the exploitation of a more advance of spark timing with a consequently higher BMEP.

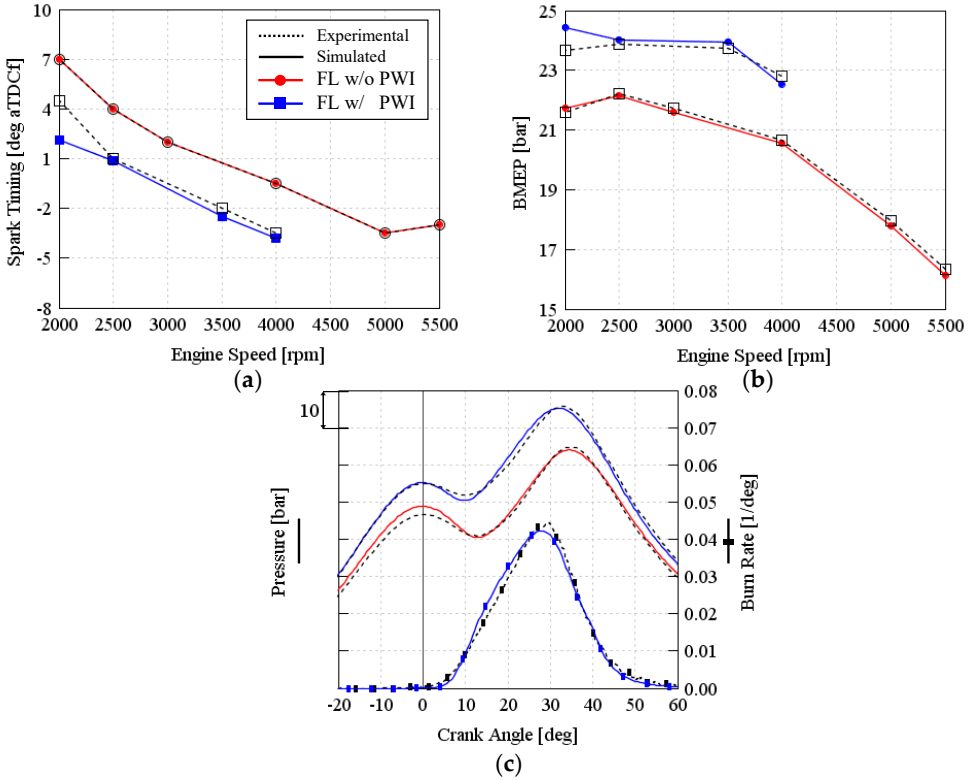


Figure 2-14: In-cylinder Pressure (left), and Burn rate (right) at 4000 RPM – Full-Load both in dry and wet conditions; simulated (red solid line) and experimental (black dashed line)

2.5 Engine Virtual calibration

At first, SITurb combustion model – previously calibrated only considering high-load operating conditions (see '*2.3 Numerical Set-up*' and '*2.4 Port Water Injection Model*') – is validated considering the complete test matrix (Figure 2-3). Validation results are shown through the correlation plots of Figure 2-15, in which combustion parameters from 1D-CFD simulations and experimental tests are compared. The combustion center of gravity angle MFB50 (top left) and duration MFB10-90 (top right) are properly predicted by the combustion model achieving an average error lower than 3 deg. The same accuracy is reached for maximum pressure (avg. error lower than 5 bar) and BSFC (avg. error lower than 5 g/kW-h). After its validation, the SITurb model is exploited to perform a virtual calibration of the engine. The latter includes the definition of a water injection strategy and the optimization of intake valve lift profiles and main engine parameters.

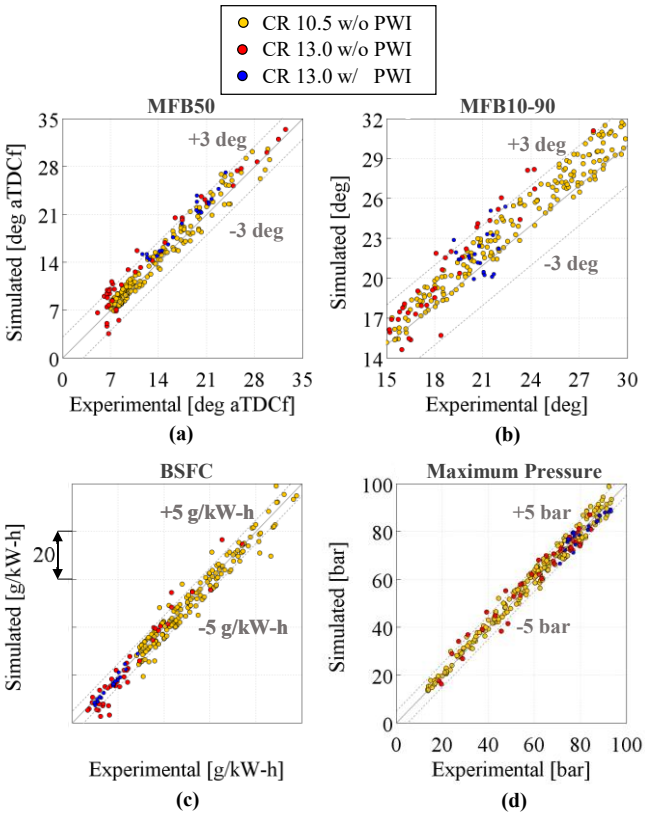


Figure 2-15: Correlation plots between 1D-CFD predictions and experimental results: combustion center of gravity MFB50 (top left), combustion duration MFB10-90 (top right), Brake Specific Fuel Consumption (bottom left), and maximum in-cylinder pressure (bottom right).

2.5.1 Water Injection Strategy definition

The correlated model of the engine in configuration 3, which features a compression ratio equal to 13 and a PWI system, was exploited to perform an optimization of the main calibration parameters, such as spark timing, boost pressure and Water-to-Fuel ratio over the entire operating map. In particular, for each knock-limited operating point of the engine in configuration 2, Water-to-Fuel ratio sweeps were carried out. An example of the results obtained through this methodology is reported in Figure 2-16, which shows the spark-timing, the combustion center of gravity angle, the burn duration and the Brake Specific Fuel Consumption for the operating point 2500 RPM – 18 bar BMEP. As noticeable in Figure 2-16a, the more the injected water increases, the more the knock tendency reduces thus allowing for a more advanced spark timing. It is worth to highlight that the combustion phasing is adjusted until the KITI limit or the optimal

combustion phasing (corresponding to a MFB50 value of about 8 deg aTDCf) is achieved. The better combustion phasing implies lower BSFC and higher brake thermal efficiencies, as illustrated in Figure 2-16d. However, an excessive increase of mixture dilution through the injection of water reduces the laminar flame speed, thus lengthening the burn duration (Figure 2-16c), with a detrimental effect on thermodynamic efficiency. Indeed, although the spark timing is linearly anticipated with the amount of injected water, the rate of BSFC reduction with respect to the water content is lower as soon as the burn duration starts increasing. Specifically, starting from a dry operating condition, the BSFC initially reduces by approximately 6 g/kW-h for each 10 mg of water injected per cylinder. However, when the injected water quantity is increased above the 10 mg threshold, the duration of combustion begins to increase and the BSFC decrement becomes of about 1.5 g/kW-h for each additional 10 mg of injected water. Therefore, for the selected operating condition, 10 mg of injected water per cylinder, which corresponds to a W/F equal to 26%, is considered the optimal amount to reduce as much as possible the BSFC and to contemporarily to limit the water consumption.

The result of this calibration activity, applied to each knock-limited operating point of the engine in configuration 2, is summarized in Figure 2-17. The latter shows the map of the optimal quantity of water to be injected for configuration 3 according to the engine speed and the BMEP. On the other hand, the differences between configuration 3 (optimized water injection strategy – see Figure 2-17) and 2 (no PWI) in terms of MFB50, burn duration and BSFC are reported in Figure 2-18.

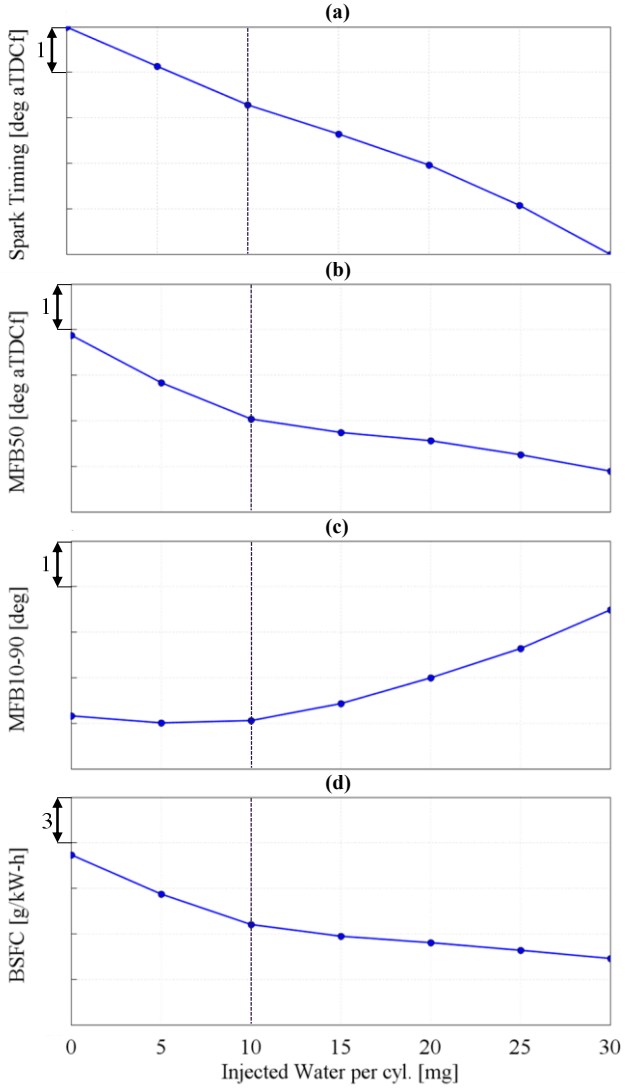


Figure 2-16: (a) Spark timing, (b) Combustion center of gravity angle MFB50, (c) Burn duration (10-90%) and (d) Brake Specific Fuel Consumption as a function of the injected water mass per cylinder at the operating point 2500 RPM – 18 bar BMEP. A vertical gray vertical line has been added in each plot to highlight the quantity of injected water mass beyond which an increase in combustion duration is obtained.

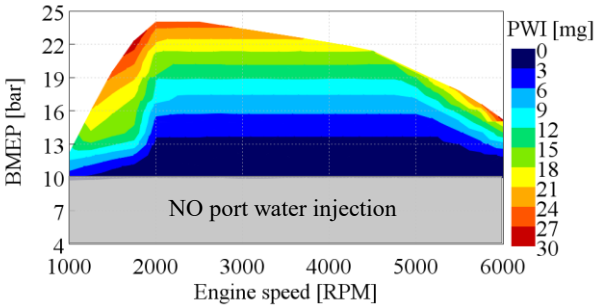


Figure 2-17: Engine (configuration 3) map of the injected water mass per cylinder

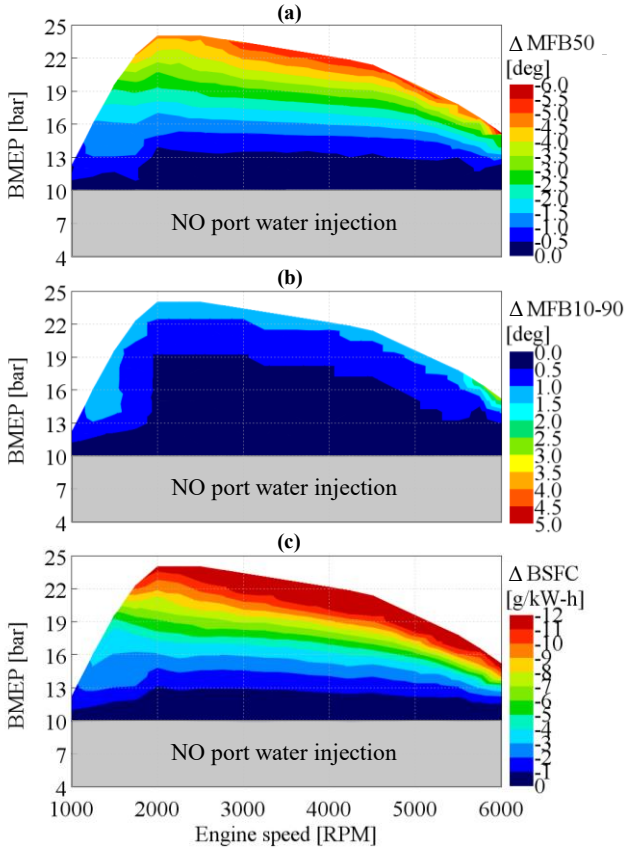


Figure 2-18: Engine map of the variation of (a) combustion center of gravity angle, (b) burn duration (10-90%) and (c) Brake Specific Fuel Consumption between engine variants 2 and 3.

2.5.2 Intake Valve Lift Profile Optimization

The definition of an optimal water injection strategy, thanks to its knock mitigation capability, allows a significant reduction of BSFC – and thus of CO2 emission – passing from configuration 2 to configuration 3.

However, a further contribution to the reduction of knock likelihood could still be provided by an intake valve strategy optimization. As schematized in Figure 2-19, this solution could be exploited in synergy with PWI in different way. For example, by keeping the same level of BSFC achieved for configuration 3, the valve strategy optimization could be adopted to suppress knock instead of PWI, thus reducing the water request (conf. 4). On the other hand, the same strategy could be used to further advance the combustion phasing, so to improve the fuel economy of configuration 3 with the same level of water consumption (conf. 5).

In this regard, for each knock-limited operating point, a Design of Experiments methodology was adopted for the selection of the optimal combination of injected water and Intake Valve Closing (IVC) position, varied by keeping constant the reference Intake Valve Opening Position. An example of the results obtained through this methodology is reported in Figure 2-20, which shows the MFB50 (a), the burning duration (b) and the BSFC (c) for different combinations of injected water and IVC positions for the operating point 2500 RPM – 18 bar BMEP. It is worth pointing out that, for this specific case, a maximum value of 10 mg of injected water was considered on the basis of the analysis whose results are shown in Figure 2-16.

As noticeable in Figure 2-20c, the minimum BSFC area is located in correspondence with the operating points featuring an IVC of 630 deg aTDCf and

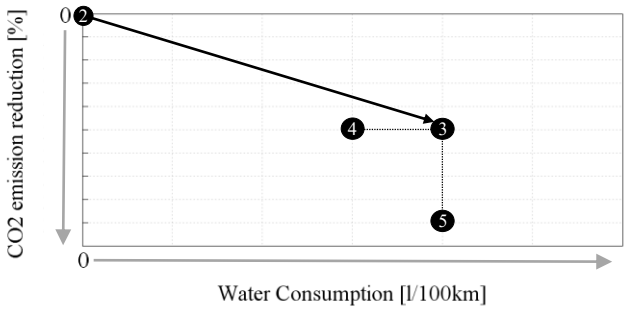


Figure 2-19: Schematic representation of the engine variants with CR 13

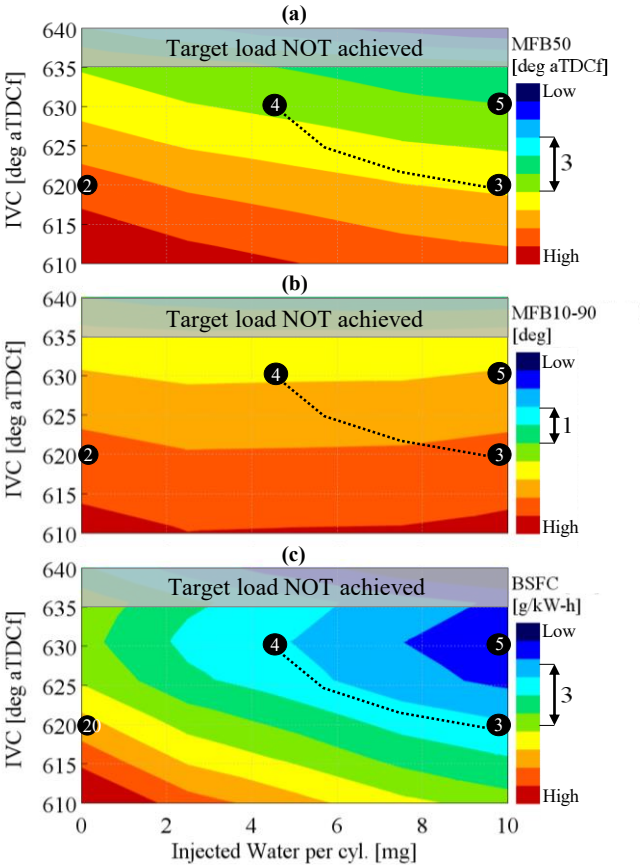


Figure 2-20: (a) Combustion center of gravity angle, (b) burn duration (10-90%) and (c) Brake Specific Fuel Consumption obtained as a function of injected water per cylinder and Intake Valve opening duration for the operating point 2500 RPM × 18 bar BMEP

an injected water mass of 10 mg (conf. 5). The adoption of earlier IVC involves a higher knock tendency (lower Miller effect, increase of geometric compression ratio [46]), a more retarded combustion phasing and a consequently higher BSFC. On the other hand, more delayed IVC positions (higher Miller effect, reduction of geometric compression ratio and knock tendency) induce backflow phenomena, implying a significant reduction of volumetric efficiency and a consequent increase of boost pressure that the turbocharger is unable to deliver, having reached its maximum rotational speed. An IVC of 630 deg could also be adopted to obtain the same BSFC obtained in configuration 3, with almost half the required water (conf. 4). Since the impact of valve profile optimization on BSFC is low compared to impact on water consumption, and since water exploitation should be limited to minimize water tank size, configuration 4 was preferred to 5, which was not taken

into account for the evaluation of the engine fuel economy over the different type approval and RDE driving cycles.

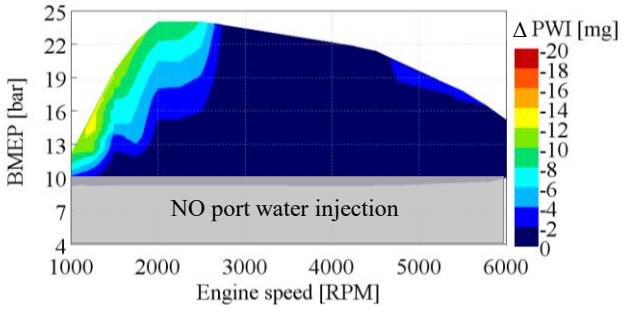


Figure 2-21: Configuration 4 – engine map of the reduction of the injected water mass per cylinder obtained though the intake valve lift profiles optimization with respect to configuration 3 (see Figure 2-17**)**.

The result of this calibration activity is summarized in Figure 2-21, which shows the map of the difference between configuration 3 and 4 in terms of injected water quantity. It is worth pointing out that, for engine speeds above 3000 RPM, no WI reduction could be achieved because the intake valve lift profiles of the reference configuration were already very close to the optimum.

2.6 Virtual test rig

To assess the potential CO2 emission reduction achievable through high Compression Ratio, Miller Cycle and PWI system in different driving conditions, a virtual test rig is developed by using the commercially available software GT-SUITE [43]. The virtual test rig integrates:

- the calibrated 1D-CFD engine model;
- the model of a B-segment Sport Utility Vehicle (B-SUV);
- a 6-gear manual transmission;
- a 12V vehicle electric network.

The vehicle is modelled through a forward approach [62] which takes into account the longitudinal dynamics and integrates the 1D engine model described in the previous section of the paper. The vehicle driver is simulated by means of a Proportional-Integral-Derivative (PID) controller that defines the required boost pressure to achieve the desired power, the brake pedal and the clutch position. The gear shift, on the contrary, is imposed for the NEDC according to UNECE 83 [63],

while for the other driving cycles it is computed by means of the Heinz Steven's tool [64], according to the UE Commission Regulation [65].

The definition of the engine operating parameters is performed through a virtual Engine Control Unit (vECU). The latter was developed for the exploitation of the engine maximum performances, while taking into account the typical constraints for a turbocharged gasoline engine, such as knock, compressor surge and speed margins, maximum temperature at the compressor outlet (T2) and maximum in-cylinder pressure, as well as turbine inlet pressure (P3) and temperature (T3) which are required to limit thermal and mechanical stresses of the engine and its subcomponents. To address these tasks, the vECU exploits a set of PID controllers:

- **Wastegate valve PID controller**: it regulates the wastegate valve opening to achieve the boost pressure target requested by the driver and to simultaneously satisfy the constraints on turbocharger (i.e., avoiding surge and limiting shaft speed), temperature at the compressor outlet, pressure and temperature at turbine inlet;
- **Throttle valve PID controller**: it regulates the throttle valve position to achieve the intake manifold pressure target requested by the driver;
- **Spark-timing PID controller**: it adjusts the combustion phasing to limit the knock intensity and the maximum in-cylinder pressure or to achieve the optimal combustion phasing, corresponding to a MFB50 value of about 8 deg aTDCf.

The vECU also controls the Energizing Time (ET) of the injector to guarantee a stoichiometric combustion and the water flow rate to achieve a Water-to-Fuel ratio target variable depending on the engine operating point. The maps of W/F (more details of which are reported in the following section), boost pressure and the intake manifold pressure are previously defined in steady-state engine conditions.

The engine model integrated in the virtual test rig is controlled using as setpoints the above-mentioned engine maps for each time step as a function of the actual engine speed and target brake torque defined by the driver controller. Since the engine features a VVA system for the intake valves actuation, the proper valve lift profile is chosen as function of the actual engine speed and target brake torque.

The use of such an approach provides a high level of accuracy for the fuel consumption evaluation also in highly dynamic driving cycles, as proved by Millo et al. [66]. It is worth noting that the fuel flow rate in this way is not estimated by interpolating a performance map, but is the result of a fully-physical engine model that reproduces transient phenomena as water film formation in the intake port walls

[49], the turbo-lag effect and the mechanical inertia of the components, which are crucial for the air charging operation and consequently for the fuel consumption especially for highly dynamic driving cycles such as RTS95 and US06.

2.6.1 Results

The developed virtual test rig is finally exploited to assess the four engine configurations (see Table 2-1) in terms of CO2 emission and water consumption in different driving conditions. In this regard, seven driving cycles were selected: the New European Driving Cycle, the Worldwide Harmonized Light-Duty Test Cycle (WLTC), the Federal Test Procedure (FTP75), the Artemis Motorway Cycle, the Standardized Random Test for an aggressive driving style (RTS95), a Real Driving Emission cycle and the US06 Supplemental Federal Test Procedure [67,68]. For the sake of conciseness, the driving schedule and the main operating points of the engine along the abovementioned cycles are reported in the Appendix of this manuscript (see Appendix, Figure A, B, C and D).
The selected cycles were firstly analyzed and classified as a function of a parameter called "VxApos95", that is the 95th percentile of the statistical distribution of the product between vehicle velocity and positive acceleration calculated instant by instant. This parameter is used as an indicator of the power requested during the test: as shown in Figure 2-22, the less aggressive driving cycles is the NEDC while the most dynamic ones are the RDE, the RTS95 and the US06 driving cycles.

Figure 2-23a shows the water consumption of the engine variants 3 and 4, while Figure 2-23b highlights the CO2 emission reduction achievable over each driving cycle by engine configurations 2, 3 and 4 with respect to the reference configuration 1. Focusing on Figure 2-23b, it is possible to notice that the increase of compression ratio from 10.5 to 13 (conf. 2 vs. conf. 1, red bars) enables a significant CO2 emission reduction of -7% over the NEDC driving cycle. On the other hand, along with the increase of the test dynamics, the positive benefits of a higher compression ratio on fuel consumption reduce to a minimum of 1.25% over the RTS95 cycle. The increase of compression ratio implies significant improvement of thermodynamic efficiency only for knock-free operating points. On the other hand, at high-load, where knock is controlled by delaying the combustion phasing, the increase of compression ratio induces a relevant increase of knock likelihood, thus requiring a further delay of MFB50 which has detrimental effects on BSFC.

For these reasons, as highlighted in Figure 2-24, since along the NEDC the engine operates on average at low-load, the benefits of the increase of the compression ratio are much greater than considering the RTS95 cycle, where the engine runs predominantly at knock-limited operating conditions. To fully exploit the benefits of a higher compression ratio over highly dynamic cycles, PWI is required. As expected, considering configuration 3 (see Figure 2-23, light blue bars), PWI has a significant impact on the fuel consumed along RDE, RTS95 and US06, contributing to reduce CO2 emission of a further -2.5% over the RTS95 cycle.

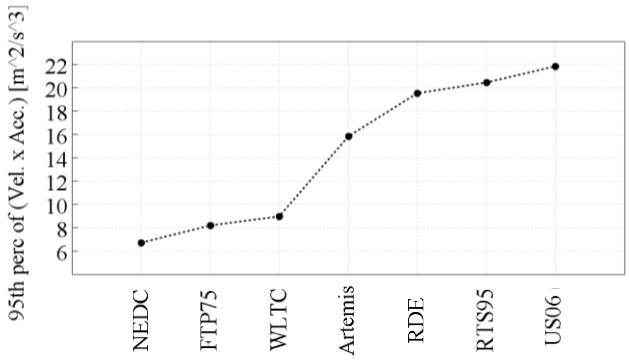


Figure 2-22: 95th percentile of VxApos (vehicle velocity multiplied by vehicle positive acceleration) as a function of driving cycles

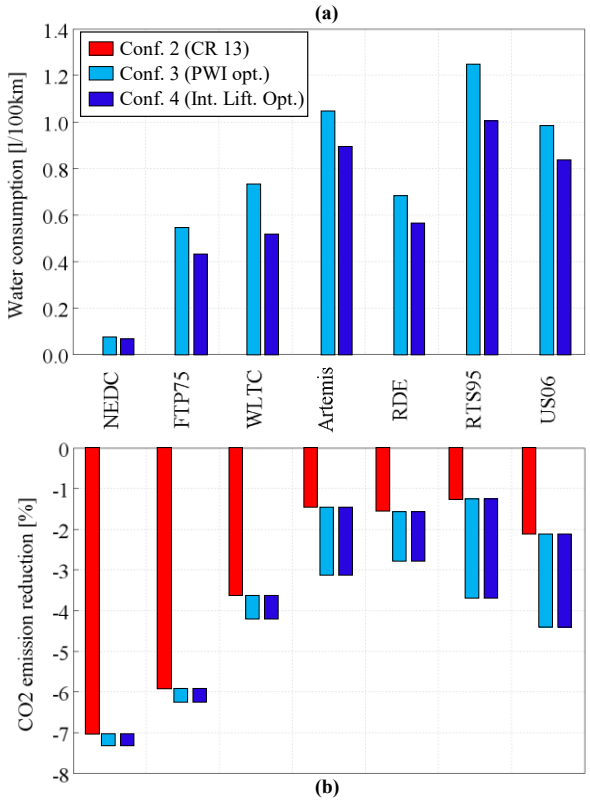


Figure 2-23: (a) Water consumption and (b) CO2 emission reduction as a function of driving cycles

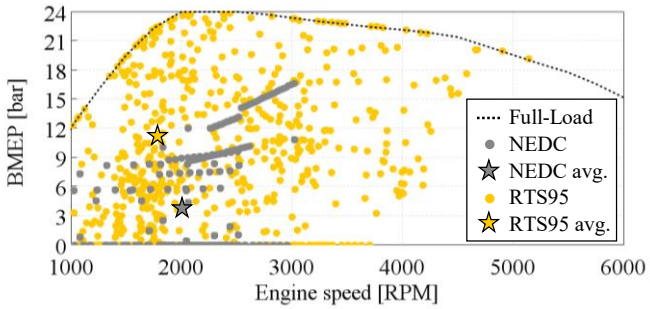


Figure 2-24: Operating points covered by the engine along the NEDC and the RTS95 driving cycles

On the other hand, over the NEDC, as the engine is predominantly operated at low-loads, the consumption of water and its benefits are almost negligible. Concerning configuration 3, the RTS95 is the driving cycle that requires the highest water consumption, i.e. 1.25 l/100km. By optimizing the intake valve lift profiles, exploiting a more aggressive Late Intake Valve Closing strategy, a reduction of

18% on average of water consumption can be obtained over all the driving conditions: in particular, the water consumed along RTS95 cycle reduces from 1.25 l/100km to 1.01 l/100km.

2.7 Conclusions

This chapter presents a quasi-dimensional approach to model a PWI system integrated in a Downsized Turbocharged Direct Injection Spark Ignition engine. Moreover, it shows the effects of different advanced technologies on the performance of the above-mentioned engine, which equips an European B-segment Sport Utility Vehicle. In particular, the CO2 emission reduction as well as the water economy along different type approval and RDE driving cycles related to the exploitation of higher compression ratio, Port Water Injection and Miller strategy are reported.

In a first stage, experimental investigations were carried out at the engine test bench to characterize the engine behavior under "dry" (i.e. without WI) and "wet" (i.e. with WI) operation. Afterwards, the experimental outcomes obtained without PWI were used to preliminary calibrate combustion (SITurb), CCV and knock models. In particular, knock model constants were tuned by simulating CCV over 300 consecutive engine cycles with the aim of matching the experimental percentage of knocking cycles. In a second stage, the results of 3D-CFD simulations of the PWI system were used to calibrate a port-puddling model. The latter, once implemented in the reference engine model, was proven to properly replicate transient phenomena of water wall film formation, catching cycle by cycle the amount of water that enters into the cylinder and is therefore available for knock mitigation. Subsequently, the experimental results collected at medium loads with W/F sweeps were considered for the refinement of both water evaporation and combustion modelling. The first one was calibrated to properly discern the fraction of the injected water that is producing the charge cooling through its evaporation from that which is evaporating due to the heating from the walls. Then, the SITurb model was tuned in order to carefully predict the impact of the injected water on the Laminar Flame Speed: in particular, a linear dependence between the in-cylinder vapor content and the Dilution Effect Multiplier was found. The SITurb model was finally validated against the complete experimental test matrix, showing the capability to accurately predict the effects of water injection in terms of both burning rate slow down and knock tendency reduction. Finally, the proposed methodology was used to create a virtual test rig, featuring a 1D-CFD engine model, coupled with a vehicle model, including the 6-gear manual transmission and the

vehicle electric network. As a result, this simulation platform was used to optimize the main engine calibration parameters, such as spark timing, boost pressure, Water-to-Fuel ratio and intake valve lift profiles over the entire engine operating map. Four different engine configurations (see Table 2-1) were finally selected and assessed in terms of CO2 emission over different driving conditions. The increase of compression ratio (conf. 2) implies significant CO2 emission reduction only for driving cycles where the engine mainly operates at low-load (i.e. NEDC -7%, FTP75 -6%). The same benefits are not achieved over more dynamic cycles, such as RDE, RTS95 or US06, where the engine frequently reaches high-loads: in these operating points the high compression ratio increases the knock likelihood, thus forcing a more delayed combustion and a worsening of the BSFC. The exploitation of a higher compression ratio in combination with PWI allows a reduction of CO2 emission on average of 3.5% over the most aggressive driving cycle. The optimization of Intake Valve Lift profiles contributes to reduce of 18% on average the water consumption required by each driving cycle.

Summarizing, the presented numerical approach showed the potential to predict, on a physical basis, the combined effects of various techniques on the overall performance map as well as on the vehicle fuel and water consumption. This methodology could represent an effective tool to identify the expected improvements of new technologies, contributing to support and drive the calibration and development process of new engines and vehicles.

Chapter 3

Hydrogen-fueled Internal Combustion Engine

3.1 Introduction

Nowadays hydrogen, especially if derived from biomass or produced by renewable power, is rising as a key energy solution to shift the mobility of the future toward a low emission scenario. If compared to the conventional fossil fuels widely used in the transportation sector, namely compressed natural gas, gasoline and diesel, hydrogen shows unique physical and chemical properties, as reported in Table 1-1. From a thermodynamic point of view, H2 allows an excellent combustion quality: indeed, it features a high Lower Heating Value and fast flame propagation over a wide range of temperature, pressure, and air-to-fuel ratios. From the abnormal combustion perspective, the high values of both autoignition temperature and octane number of hydrogen can limit the knock likelihood. However, the low minimum ignition energy might trigger backfire issues or even pre-ignition. Finally, the high diffusion coefficient of H2 leads to fast mixing with the induced air (compared to conventional fuels), which is beneficial for mixture homogenization especially in the case of Direct Injection.

To preliminarily assess the performance of H2-fueled engines, despite several research projects only rely on experimental activities [30,69], the exploitation of numerical tools is crucial to fully understand the fundamentals of both mixture preparation [70] and combustion process [71] and to perform a comprehensive optimization of the system. Klepatz et al. [72] presented a combined approach where the one-dimensional (1D) Computational Fluid Dynamics (CFD) model of the H2-ICE has been primarily validated against a set of experimental data and then used to compare the efficiency of different engine concepts. In a subsequent work [23], the same methodology has been exploited to optimize the calibration of a diesel-revamped H2 engine and to assess the benefit of EGR on its performance and emissions. Scarcelli et al. also proposed a similar synergic approach: the results

of an experimental campaign on a single-cylinder optical engine fueled with hydrogen have been used to validate a 3D-CFD model [73] through which several sensitivity analyses on the injector geometry and of injection parameters have been performed [74]. Nevertheless, for such innovative ICE, experimental data for model validation are quite often not available, and the simulation of such an alternative fuel places several challenges related to the presence of supersonic jets [75], to the correct estimation of the burning speed [76,77], and to the prediction of the abnormal combustion phenomena [78].

In such a framework, the development of a reliable simulation tool capable to preliminarily assess the potential of the hydrogen-fueled engine and to drive its design in the early stage of the development process is to be of paramount importance especially when experimental data are lacking. To tackle this task, this chapter aims to provide a comprehensive methodology to assess, through numerical simulations, the performance of a Hydrogen SI ICE revamped from a high-performance 3.0L V6 120° Twin Turbocharged Direct Injection Spark Ignition gasoline engine. In particular, after a brief description of the case study, a 3D-CFD methodology devoted to understand H2 injection behavior and optimize the mixture preparation is presented and discussed in details. Injector position resulted a key parameter to achieve the highest level of mixture homogeneity. Afterwards, the main features of the 1D engine model, including controllers as well as combustion and knock models, are described. Then, a preliminary virtual H2-ICE architecture optimization is presented. In particular, the optimal combination of engine displacement, compression ratio and turbocharger size has been defined with the aim to achieve the full-load performance target with the minimum water consumption. Finally, the outcomes of the optimization process represented by the maps of the main operating parameters are discussed.

3.2 Case study

The research activity described in Chapter 3 is carried out on a state-of-the-art 3.0L V6 120° Twin Turbocharged Direct Injection Spark Ignition engine whose main characteristics are reported in Table 3-1. The combustion system conversion from gasoline to hydrogen was carried out simply replacing the original gasoline injector with the H2-injector represented in Figure 3-1. The latter is a functional sample specially designed and manufactured by BOSCH for low pressure Direct Injection in an H2 engine. It features:

- a nozzle that opens outward to prevent the combustion pressure in the cylinder from opening the injector and the burned gases from flowing into the injector;
- a mass flow rate of 10.5 g/s at a pressure of 25 barA and a temperature of 85°C;
- a needle lift curve which is independent of the inlet pressure, thus enabling a large spread of the system pressure (typically from 5 bar to 40 bar).

Further information on the characteristics of the H2-injection can be found in [79], while additional details related to specific engine features cannot be disclosed due to confidentiality reasons.

As described in *1.2 Scope of the Work*, at full-load, the hydrogen engine is operated in stoichiometric conditions, which implies high knock likelihood, high exhaust gas temperature, and therefore limited performance. For this reason, to achieve the demanding power target – 20% higher than the reference gasoline engine –, the H2-ICE is equipped with a Port Water Injection system. As far as the boosting system is concerned, the original twin turbocharger (without electrical assistance, not foreseen for this application) is selected for a preliminary performance estimate. However, with the aim of compacting the engine layout so as to free up space for the installation of hydrogen tank, a second configuration featuring a single supercharger mechanically connected to the crankshaft is evaluated. In particular, the roots-type HTV19000 Harrop supercharger [80], whose main features are reported in Table 3-2, is selected for this analysis.

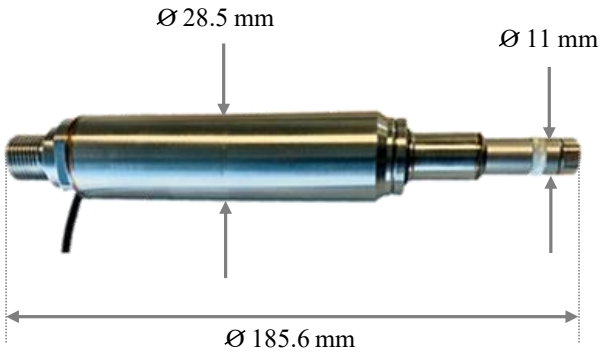


Figure 3-1: H2 injector sample geometry

Table 3-1: V6 120° Twin Turbocharged DISI engine specifications

Specification	Reference gasoline	H2-ICE Conf.1	H2-ICE Conf. 2
N. of cylinders [-]	6	=	=
Displacement [cm3]	2999	≥2999	≥2999
Bore/Stroke	>1	>1	>1
Compression Ratio [-]	>9	>9	>9
Injection System	gasoline-DI	H2-DI	H2-DI
Injection Pressure	350 bar	5÷40 bar	5÷40 bar
PWI	No	Yes	Yes
Boosting system	Electrically assisted TC	Mechanical TC	Mechanical SC
Brake Torque at 2000 RPM	reference	=	=
Brake Power at 8500 RPM	reference	+20%	+20%

Table 3-2: HTV19000 Harrop supercharger (SC) main characteristics

Specification	Value
Max. Pressure Ratio (PR) [-]	2.5
Max. Mass Flow Rate at PR 1. [kg/h]	2414
Max. Rotor Speed [RPM]	1800
Max. Input Power [kW]	93
Max. Outlet Temperature [°C]	160

3.3 Hydrogen Injection Analysis

In the process of building up a virtual engine dedicated for hydrogen development, the injector characterization plays a role of paramount importance. In this regard, this section describes firstly the experimental and numerical characterization of the H2 injector. Afterwards, a preliminary analysis of mixture formation considering different lambda and injector mounting positions is presented and discussed in detail.

3.3.1 Experimental characterization of H2 injector

The analysis of the jet formed by the dedicated H2 injector was carried out through a high pressure vessel with a Schlieren setup [81]. Jet measurements were performed focusing on the variation of operating conditions like hydrogen injection pressure and vessel pressure. Moreover, on the basis of former studies [82], also the impact of the injection axial mounting position was investigated. All the tests, for reasons of safety and practicality, were firstly carried out using helium as a surrogate fuel for hydrogen. Afterwards, to prove this approach and to quantify the differences between these fluids, the Schlieren measurements were repeated using hydrogen. A summary of the experimental campaign is reported in Table 3-3 while more details on experimental test bench setup and measurements results can be found in [79]).

As depicted in Figure 3-2, an increase of the fuel pressure leads to faster penetration of the gaseous jet. On the other hand, an increase of the chamber pressure – from 1 to 3 bar – implies shorter penetrations. Figure 3-3 shows instead the jet penetration measured at different levels of retraction ‘z’, starting from a flush mounting position (retraction z = 0 mm).

Table 3-3: Experimental Schlieren measurements boundary conditions

Test	H2 injection pressure (P_f)	Back pressure (P_{ch})	Injector mounting position
Injection and back pressure variation	5 | 15 | 25 | 40 bar	1 bar	+1.2 mm
	5 | 15 | 25 | 40 bar	3 bar	+1.2 mm
Injection mounting position variation	25 bar	1.2 bar	0 | -1 | -2 | -3 | -4 mm
	40 bar	1.2 bar	0 | -1 | -2 | -3 | -4 mm

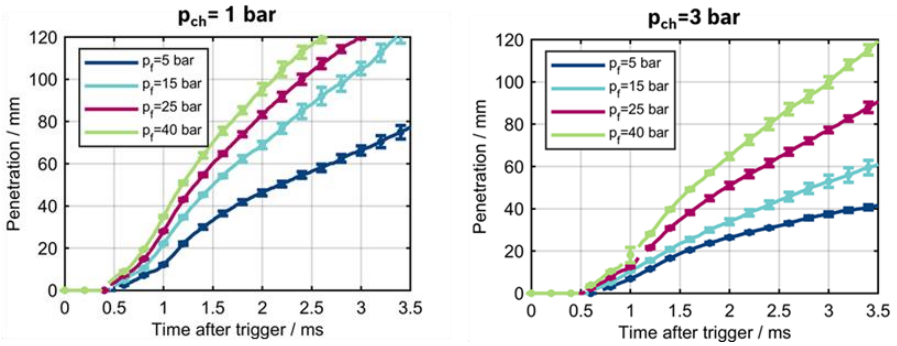


Figure 3-2: Jet penetration as a function of time for different injection and chamber pressures

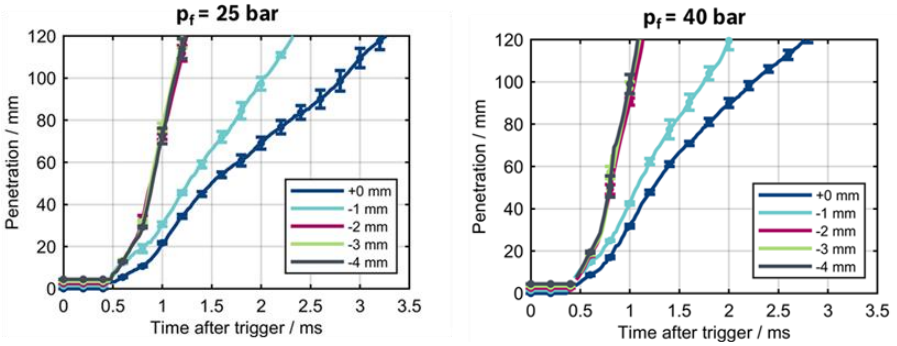


Figure 3-3: Jet penetration as a function of time for different injector mounting positions z and chamber pressures

When the injector is mounted in flush position, the jet is free to develop within the chamber. By increasing the injector retraction of 1 mm, part of the jet is still free to develop in the combustion chamber, while the remaining part interacts with the walls of the injector access. The broad jet opening angle induced by the outward opening needle collapses towards a much smaller jet angle and results in a much deeper penetration in the injector axis direction. A further increment of jet penetration is obtained with a retraction of 2 mm: in this case, the complete jet is supposed to be guided by the walls of the injector access. It follows that, beyond 2 mm injector recession, the jet penetration seems to be insensitive to higher retraction distances. For the sake of conciseness, part of the Schlieren images obtained during the test campaign are reported in the Appendix of this manuscript (see Appendix, Figure E and F).

3.3.2 3D-CFD characterization of H2 injector

Following the experiments, a 3D-CFD methodology was constructed to properly replicate the Schlieren measurements. Among all the experimental tests, the numerical analysis was based on those with injector mounting positions z = 0 mm and z = -4 mm. These two layouts provides the extreme results in terms of penetration and opening angle (see Appendix, Figure F). In particular, only the tests with injection pressure of 40 bar and chamber pressure of 1.2 bar were considered. In fact, being the case with the lowest pressure ratio P_{ch}/P_f, it is also expected to be the most challenging to reproduce through CFD simulations, mainly because of the higher Mach numbers involved.

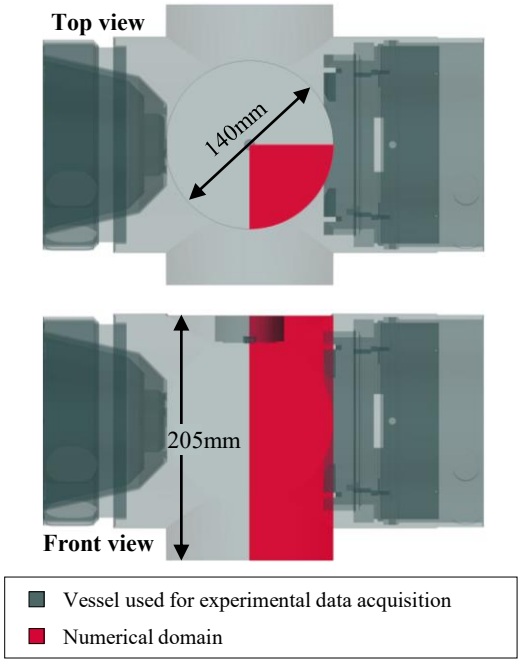


Figure 3-4: Vessel used for experimental data acquisition and numerical domain

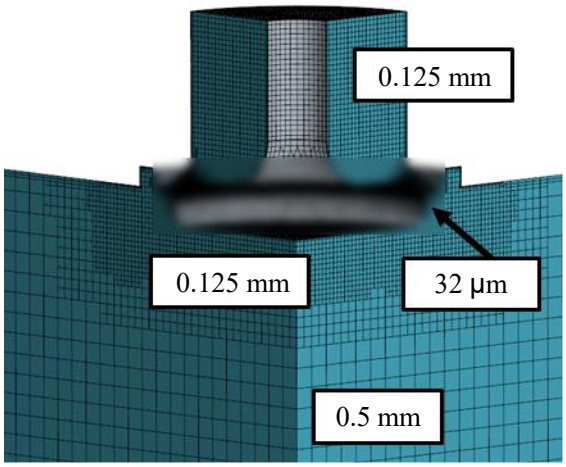


Figure 3-5: Hexahedral mesh adopted for the H2 injection analysis work. In this representation, the injector mounting position corresponds to z = 0 mm. The needle geometry is blurred for confidentiality reasons

Figure 3-4 shows the experimental vessel used for data acquisition and on which the CFD base domain was built. The cylindrical core of the vessel is 205 mm high, with a diameter of 140 mm. To decrease the computational effort, just a quarter of it was considered for the simulations. In principle, also a 2D representation could have been analyzed, but to keep an ICE mesh feasibility, the vessel quarter was used.

Concerning the numerical setup, simulations were carried out using Star-CCM+ 2206 (17.04.007), licensed by SIEMENS DISW. Coherently with the experimental acquisitions, the injected gas was helium and the flow in the chamber was initially quiescent and at 22 °C. Likewise, the wall temperature was set to 22 °C, with a no-slip boundary condition for velocity. All 3D simulation were carried out within a Reynolds-average Navier-Stokes (RANS) framework, using the realizable κ-ε turbulence model, being one of the most widely adopted models in the in-cylinder community. As for the near-wall turbulence treatment, an All-Y+ approach was adopted because of the wide range of Y+ experienced during the subsequent in-cylinder simulations where these characterizations would have been applied. Such an approach is able to simultaneously handle low-Y+ and high-Y+ by blending the corresponding wall function-based and low-Reynolds near-wall formulations. The implicit time integration method was Pressure-Implicit with Splitting of Operators (PISO) algorithm and a second order discretization scheme was used for energy, turbulence, momentum and species. As will be described later, the simulations are highly time demanding so it was crucial to simplify, where possible, the numerical setup. For this reason, the injector needle was maintained

in the fully-open position for the whole simulation duration. It should also be noted that since a mass flow inlet boundary was applied for gas inflow, the needle motion was indirectly considered. Moreover, it is well-known that a mass flow inlet can be applied regardless of the backpressure as long as the flow is choked [83,84].

As for the mesh, with a background homogeneous mesh of 0.5mm, a local cylindrical refinement was performed in the injector inner part and the portion of the chamber exposed to the jet outflow, reducing the cell size to 0.125 mm. The grid size in the space covered by the needle stroke was further reduced up to 32 μm. As for near-wall grid, five layers were used with a boundary layer thickness of 0.06 mm. The near-wall cell height was set to 6e-4 mm to maintain a wall Y+ ≈ 1. Figure 3-5 shows some details of the grid adopted for the simulations. The total number of cells is approximately 2.0 million. A constant simulation time-step of 2.5e-8 seconds was adopted. Concerning the calculation of spray width and penetration, a iso-surface of 99.9 % of the helium fuel mass was considered [85,86].

From a quantitative standpoint, as shown in Figure 3-6, the experimental gas penetration is well reproduced by CFD code for both injector axial positions, meaning that the model is generally able to mimic the complex physics behind it. The jet width measured 21 mm from injector tip is well aligned with experimental acquisition, but is slightly overestimated. It cannot be excluded that a combination of even lower time-steps and finer grid could nullify such a difference. However, considering that these simulations are already highly time-consuming in terms of processor time, the agreement with experimental data was considered enough satisfactory and applicable to in-cylinder simulations.

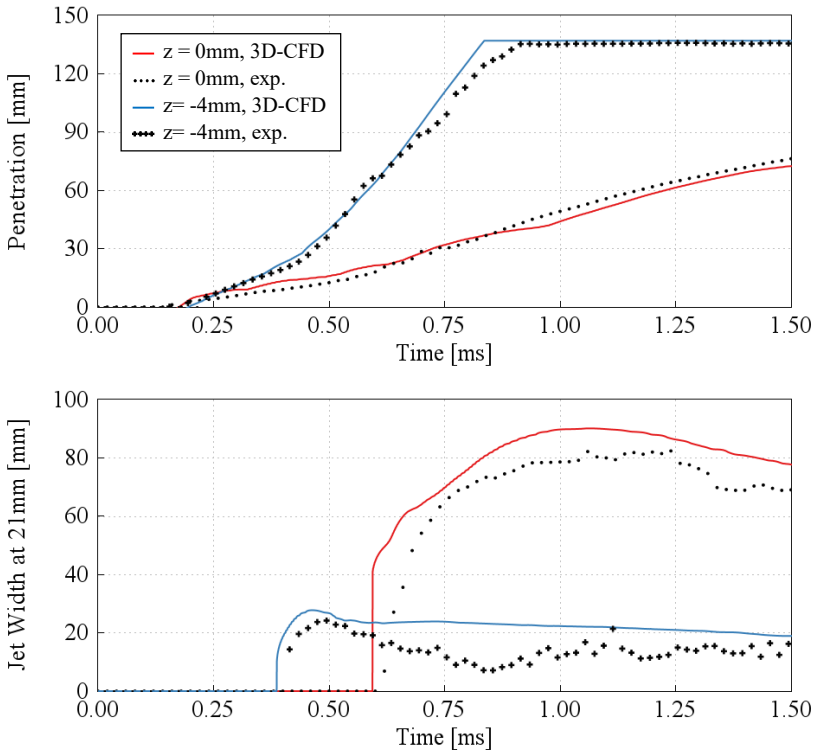


Figure 3-6: Penetration curve (top) and jet width measured 21 mm from injector tip (bottom) as a function of time. Experimental (dashed lines) and simulated (solid lines). Fixed parameters: P_f = 40 bar, P_{ch} = 1.2 bar

3.3.3 H2 Injection in a H2-ICE

Taking advantage of the hydrogen injector characterization, a preliminary analysis of mixture formation in a single cylinder engine (see Table 3-4) was performed. In particular, different lambda and injector mounting positions were considered, to have a cursory idea of mixing homogenization. The latter is of paramount importance for both abnormal combustion and engine out emissions. All configurations were simulated with the assumption to have the start of injection occurring shortly before the Intake Valve Closing (IVC) to avoid H2 from exiting through the intake ports into the intake manifold as well as to avoid a reduction of volumetric efficiency. The characteristics of the operating points considered for this analysis are listed in Table 3-4, while Figure 3-7 reports a schematic of the combustion chamber from the top, highlighting the investigated injector positions.

Table 3-4: Boundary conditions of mixture formation simulations

Specification	Test 1	Test 2	Test 3	Test 4	Test 5	Test 6
H2 inj. position	Central	Central	Intake	Central	Intake	Exhaust
H2 inj. retraction	0 mm	-4 mm	-4 mm	-4 mm	-4 mm	-4 mm
Operative Condition	WOT					
Lambda	2.3			1		
Engine speed	7500 RPM					
Start of Injection (SOI)	10 deg bIVC					
Injection duration	80 deg			120 deg		

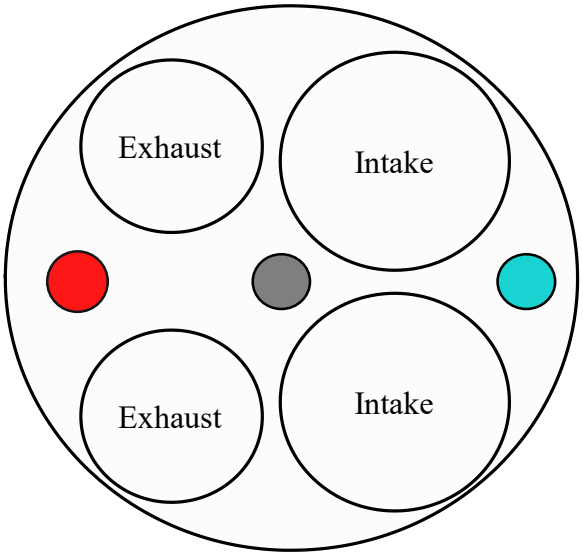


Figure 3-7: Schematic of the combustion chamber from the top, intake valves on the right and exhaust valves on the left. Injector central-mounted in grey, intake side mounted in light blue and exhaust side mounted in red.

For each test, boundary conditions for intake and exhaust ports were extracted from 1D simulations of the same engine. Moreover, thanks to the symmetry plane of the real geometry, only half of the domain was modelled.

Figure 3-8 shows the evolution of lambda distribution throughout the compression stroke for the tests carried out with a lean mixture. In Test 1, featuring a flush mounted injector positioned in the combustion chamber center, the tumble motion pushes the hydrogen towards the liner, thus limiting its interaction with fresh air. Conversely, in Test 2, thanks to the higher penetration enabled by the injector retraction, the hydrogen is able to propagate further into the combustion chamber thus improving the mixture formation. To further emphasize the mixing homogenization, in Test 3 hydrogen is injected against the tumble motion. However, the mixture formation at TDC is even worse with respect to the central-mounted injector case, resulting in a highly rich mixture close to the intake valves and highly lean on the exhaust side. As a matter of fact, the very high velocities affecting hydrogen injection prevail on tumble motion and the injected gas tends to remain confined within the intake side of the combustion chamber.

As can be observed in Figure 3-9, which reports the fuel distribution within the combustion chamber at TDCf, the stratification appears to be significant for all the three tests, meaning that the hydrogen requires more time to interact with fresh air. In fact, Test 1 shows a peak distribution around lambda 1.6 even though the average lambda is 2.3, and the richest spot close to stoichiometry. Moving the injector upwards, i.e. z = - 4 mm, the peak distribution moves to lambda 1.8, but the richest part do not exceed lambda 1.4, an operating condition that favors NOx formation. Finally, positioning the injector between the intake valves, even exploiting a retraction of z = -4 mm, leads to a drastic worsening of the homogenization at TDC, resulting in a much wider fuel distribution. In order to have a complete picture of how the injector mounting position affects the flow field, the analysis of the tumble index throughout the simulation is shown in Figure 3-9. As expected there is a reduction of the tumble when the injector is mounted in a retracted position. A further reduction of the tumble motion is obtained with the intake side mounted injector.

Concerning lambda 1 scenario, the injection duration might be even more critical due to the higher power outputs achievable. In this perspective, the case z = -4 mm is also tested with stoichiometric mixture, for three different injector positions. Figure 3-10 shows the lambda evolution throughout the compression

stroke of the tests carried out with a stoichiometric mixture, while Figure 3-11 illustrates from a quantitative standpoint their mixture distribution at TDCf.

When the injector is central-mounted, the mixture concentration in the center of the combustion chamber is rich and progressively more stratified moving towards the periphery. The peak value of lambda at TDCf appears to be richer and close to 0.8, meaning that more mixing time would be beneficial. As for the side-mounted injector, once again it results in a worse homogenization at TDCf due to a limited interaction with fresh air. Also the effect on tumble motion is confirmed, as depicted in Figure 3-11. A slight improvement of mixture formation can be obtained moving the injector between the exhaust valves. In this case, hydrogen is injected in the same direction of tumble motion, which consequently increases, as can be observed in Figure 3-11. It follows an increase of 5% of the lambda peak distribution, that moves from lambda 0.8 (Test 4) to lambda 1.2. However, even in this case a substantial portion of the mixture is in rich conditions, thus fostering pre-ignition and knock tendency.

Among the six cases analyzed, the highest level of mixture homogeneity is achieved in stoichiometric conditions through an exhaust side mounted injector and a retraction of z = -4mm. However, with the aim of further improving the mixture homogenization, future investigations will focus on the injector characteristics, such as static flow rate and tip caps.

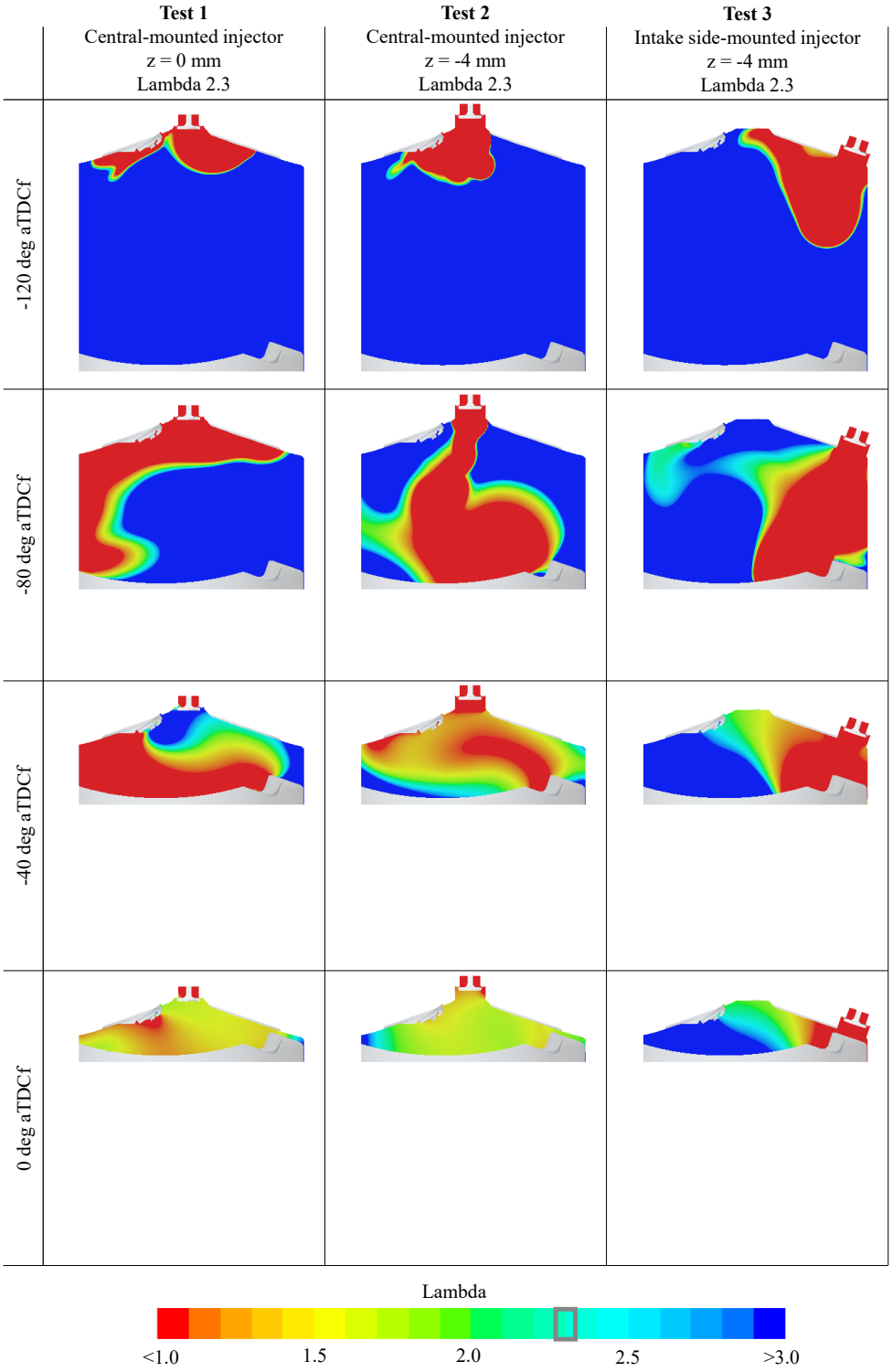


Figure 3-8: Evolution of lambda distribution throughout the compression stroke for tests 1, 2 and 3 (see Table 3-4)

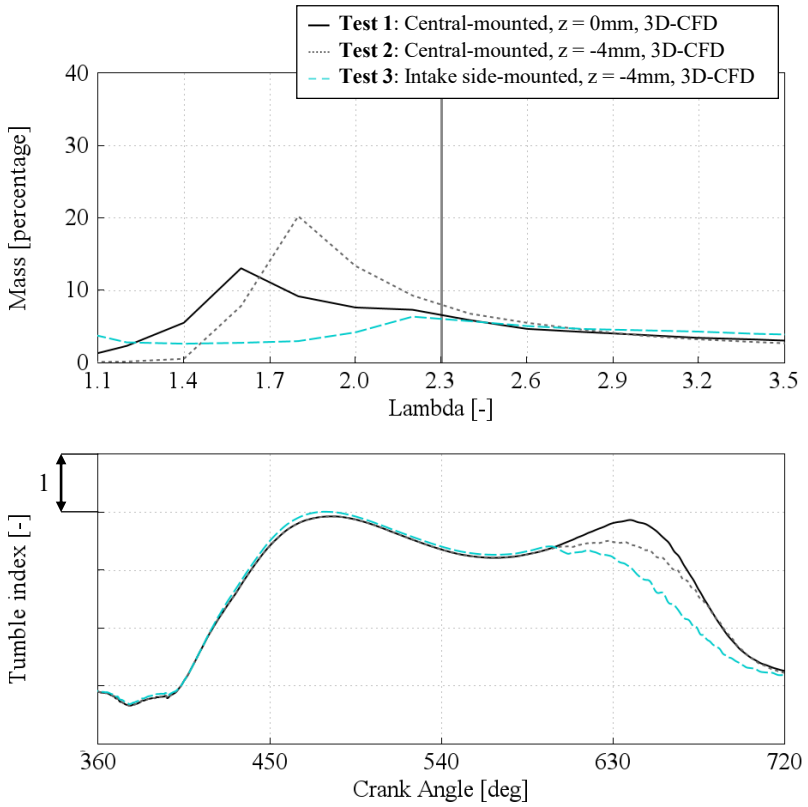


Figure 3-9: Mixture concentration distribution at TDCf (top) and Tumble index as a function of crank angle (bottom) for tests 1, 2 and 3 (see Table 3-4)

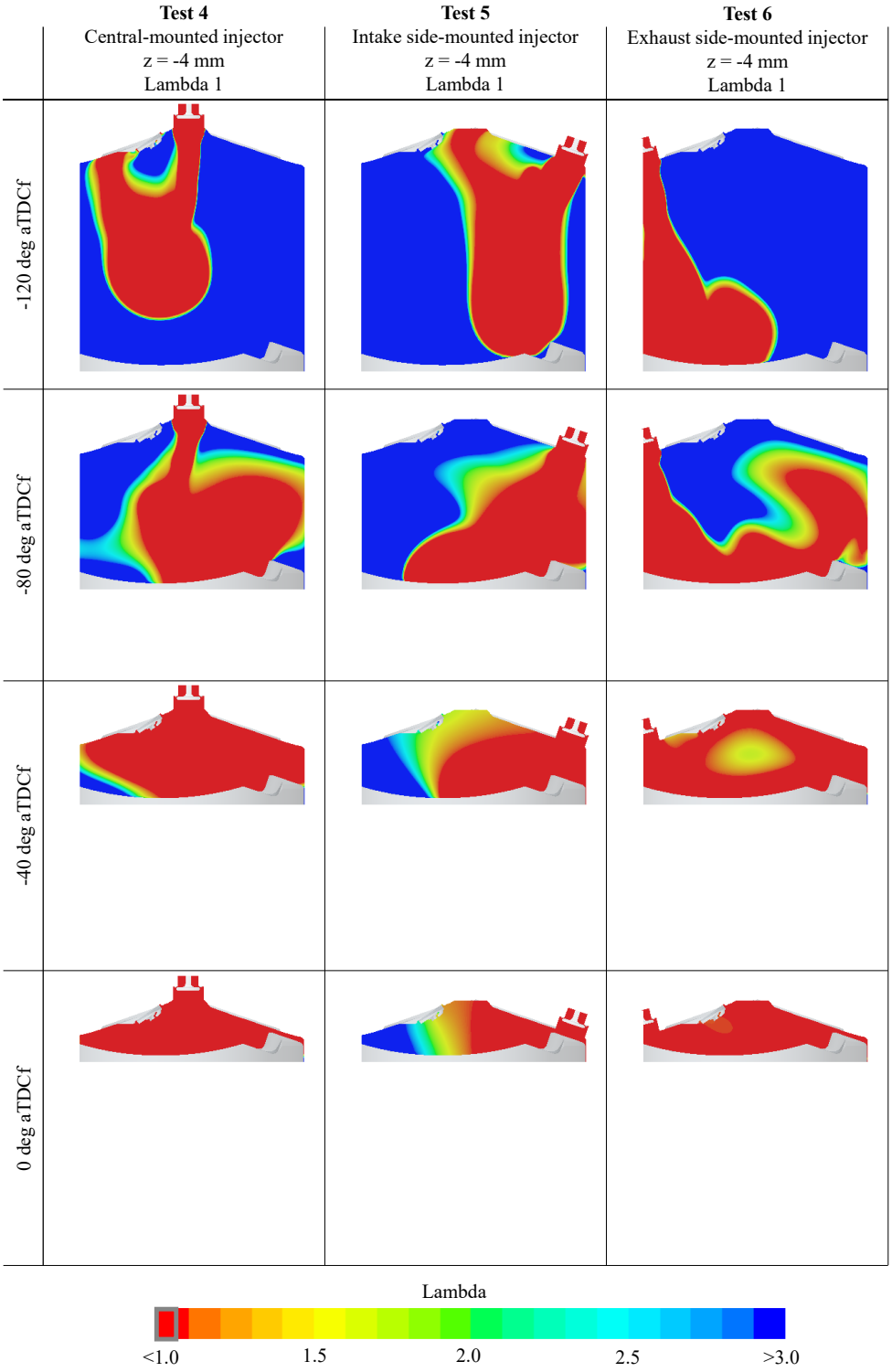


Figure 3-10: Evolution of lambda distribution along the compression stroke for tests 4, 5 and 6 (see Table 3-4)

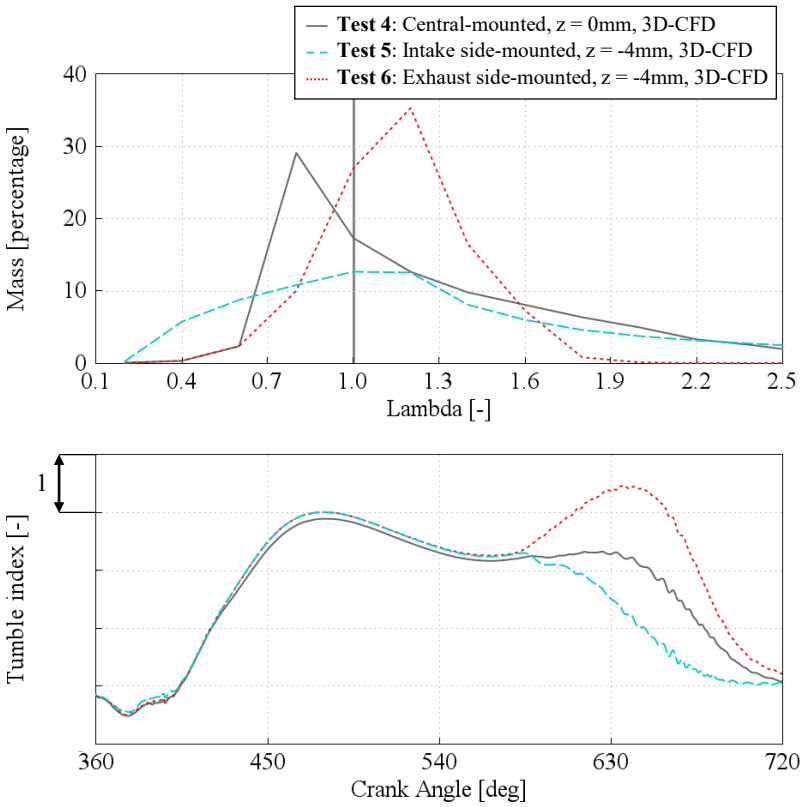


Figure 3-11: Mixture concentration distribution at TDCf (top) and Tumble index as a function of crank angle (bottom) for tests 4, 5 and 6 (see Table 3-4)

3.4 H2-ICE performance analysis

To preliminarily assess the potential of a hydrogen-fueled engine and to drive its design in the early stage of the development process, the creation of a reliable simulation tool is of paramount importance, especially when experimental data are lacking. In this perspective, this section describes the main features of the 1D-CFD model of the H2-ICE. Afterwards, the engine performance achieved through the turbocharged and the supercharged configurations are compared. An optimization of engine displacement, boosting system size and compression ratio is then carried out to prove the capabilities of the proposed methodology to preliminary drive the design of the engine architecture. Then, once defined the most suitable configuration in terms of engine performance, the complete engine maps are presented and discussed in detail.

3.4.1 Methodology

At first, a 1D-CFD model of the reference engine was built by means of GT-SUITE®. The code contains a detailed representation of intake and exhaust line, valve lift profiles, engine cylinders and charging system. Orifice connection were adopted to reproduce the pressure drops induced by air-filter, charge-air-cooler and aftertreatment system. Boost system operation was described by a standard map-based approach, while the flow permeability of the cylinder head was modelled by experimentally-derived flow coefficients. Hydrogen injection was performed through a simple injector model directly connected to the cylinders. The friction losses were calculated by the Chen-Flynn approach [87]. In-cylinder wall temperatures were calculated by a "TWallSoln" model, which is a finite element based solver that calculates in each cycle the heat flux from the gas to the walls and from the latter to the coolant fluids, water and oil, and in-cylinder heat transfer estimation was based on the Woschni correlation [88]. Concerning water injection, it was performed via multiple profile injectors connected to the intake runners. The port-puddling model as well as the evaporation model described in *Port Water Injection technology* were also implemented.

Combustion model

The recent works available in the literature concerning the simulation of the combustion process for H2-air mixture showed both numerical approaches [72,89,90] and phenomenological models [24,91,92] to address this objective. However, the absence of an extensive experimental dataset concerning the application of H2 in ICEs, which is needed to properly calibrate a phenomenological combustion model (e.g., SITurb), made the phenomenological approach unsuitable. For this reason, a Wiebe function [53] was adopted to impose the H2 burn rate as described by Equation 12:

$$x_b = CE\left(1-\exp\left[-WC\left(\frac{\theta-ST}{MFB10-90}\right)^{E+1}\right]\right) \quad (12)$$

where θ is the crank angle, ST is the spark timing, MFB10-90 is the duration from 10% to 90% of burned fuel mass, WC a constant value function of MFB10-90, CE is the combustion efficiency while E is the Wiebe Exponent [53].

On the basis of a former study [93], 100% combustion efficiency was considered (which means CE = 1) while the Wiebe exponent was assumed equal 3.3 and 1.6 for stoichiometric and ultra-lean mixtures respectively.

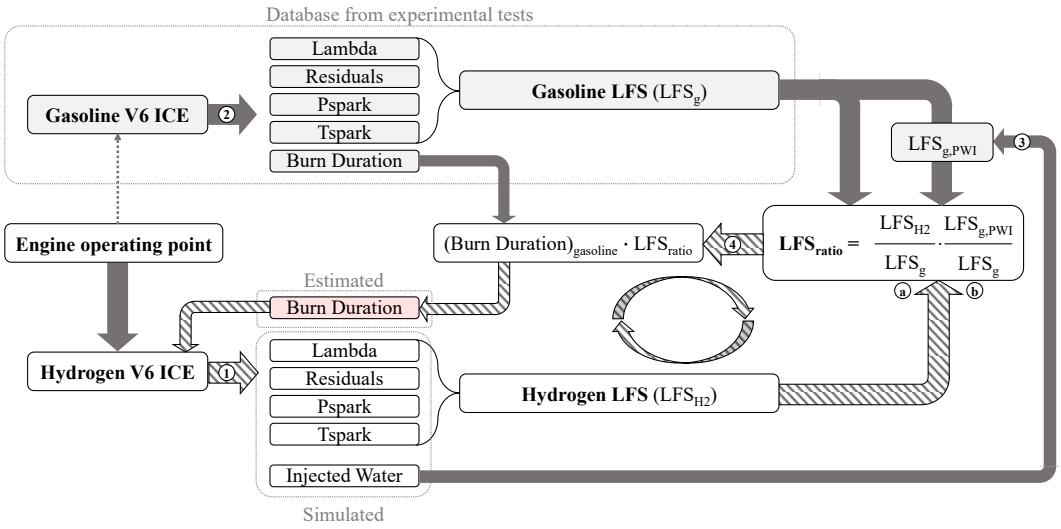


Figure 3-12: Schematic representation of burn duration estimation for a hydrogen engine

As for the burn duration, it was estimated as schematized in Figure 3-12. Given an operating point to be simulated with the hydrogen engine, defined in terms of load (expressed in BMEP) and engine speed:

1. a fist-attempt H2 combustion duration (e.g., 10 deg) is assumed. The target operating point is then preliminarily simulated to provide the inputs (pressure and temperature at spark timing, lambda and residuals mass) for hydrogen laminar flame speed (LFS_{H2}) calculation. The latter is obtained using the equation presented in [24];
2. exploiting a database of experimental data obtained at the same load and speed from the reference gasoline engine, the gasoline laminar flame speed (LFS_g) is estimated through Equation 3 and considering the dilution effect multiplier (Ce) equal to 0.872;
3. if the H2-ICE required a certain amount of water to be injected for component protection or knock mitigation, a second gasoline laminar flame speed is calculated taking into account the effect of water. To this aim, equation 3 is used considering $C_D=0.872+0.0062\cdot\{m_{trap}[mg]\}$ (see *2.4.3 Water dilution effect* for more details)
4. the gasoline experimental burn duration is scaled trough the LFS_{ratio}, which is defined as the product between:
    a. the ratio between hydrogen and gasoline laminar flame speed without water correction (which accounts the transition from gasoline to hydrogen in dry conditions);

b. the ratio between the gasoline LFS corrected as a function of the injected water and the gasoline LFS in dry conditions (which accounts the transition from dry to wet conditions).

The above described methodology strongly relies on the hypothesis that the turbulence effect on flame front speed of hydrogen and gasoline are comparable.

Knock model

The same properties that make hydrogen such a desirable fuel for SI internal combustion engines are also responsible for the risk of abnormal combustion. As already pointed out in the paper introduction, the wide flammability limits, the low required ignition energy and the high flame speed can result in the autoignition of the unburned mixture, a prime limitation that needs to be avoided while maintaining superior performance. The literature on the knock modelling in a H2 fueled engine is quite limited. In addition to Li and Karim [78], who proposed a knock criterion comparing the energy released by end-gas reactions to the energy released by the normal flame propagation, most of authors [94–96] computed the prediction of knock occurrence by adopting the approach proposed by Livengood and Wu [57] (see Equation 6). In general, the calculation of the induction time relies to phenomenological formulations originally developed for gasoline mixtures [60]. However, these approaches require as input the Research Octane Number whose determination with the conventional ASTM method is difficult to obtain for hydrogen [94]. Therefore, for this preliminary analysis, an alternative approach was adopted [42]. The selfignition times have been computed through 0D chemical reactor simulations in the CONVERGE environment: this tool solves the time-dependent equations that govern the evolution of chemical and thermodynamic states of an air-fuel mixture, allowing its exothermal reaction in a constant-volume bomb. The time required to observe a temperature increase of 400 K from its initial value is defined as induction time. Such calculations were carried out covering a wide range of pressure, temperature, air-to-fuel ratio, residuals and water content.

Controllers

For each specific operating condition, several constraints are present, such as knock, compressor surge and speed margins, maximum boost temperature (T2), maximum hydrogen and water flow rate, maximum in-cylinder pressure, maximum rate of in-cylinder pressure increase, turbine inlet pressure (P3), as well as turbine and Three-way catalyst inlet temperature (T3 and T4 respectively), required to limit thermal and mechanical stresses of the engine and its subcomponents. Based on

these limitations, a set of PID controllers were employed. In particular, concerning the turbocharged H2-ICE (configuration 1), a first PID acts on the turbine wastegate valve opening position to follow the assigned load level and to simultaneously satisfy the constraints on the turbocharger, T2 and P3.On the other hand, regarding configuration 2, the same PID controls the opening position of a non-return valve the allows to recirculate the boosted air at the supercharger inlet. If the wastegate or the non-return valve are completely open and the engine load is above the target, the PID starts closing the throttle valve, which is normally fully-open. Contemporarily, a second PID tunes the spark timing until the Knock Induction Time Integral (KITI) or the maximum pressure limit are reached. A third PID regulates the injected water amount to keep the exhaust gas temperature below the threshold.

3.4.2 Results

The objectives that guide the hydrogen engine design are resumed below:

- +20% maximum brake power with respect the reference gasoline engine;
- equal brake torque at 2000RPM reached by the reference gasoline engine (without the possibility to exploit electrical assistance);
- maximize the operating range in ultra-lean conditions, guaranteeing the achievement of the operating point 2000 RPM – 32% of Low-End Torque (LET) target, i.e. the average operating point experienced by the engine during the Artemis Motorway cycle
- minimum water injection demand.

Engine Architecture Optimization

At first, a Design of Experiments methodology [97] was adopted for the selection of the optimal combination of displacement and Water-to-Fuel ratio that guarantee the above mentioned H2-ICE performance target achievement. The results obtained through this methodology for configuration 1are reported in Figure 3-13, which shows the Water-to-Fuel ratio for different levels of engine displacement as a function of the brake torque achieved at 2000 RPM in dry conditions (x-axis) and the brake power reached at 8500 RPM exploiting PWI (y-axis). It is worth pointing out that the increase of engine displacement is obtained by keeping constant the bore to stroke ratio. The maximum exploitable Water-to-Air ratio has been set equal to 0.12 [95], which corresponds to a Water-to-Fuel ratio around 4.1.

As expected, configuration 1 (see Table 3-1) is not able to achieve the selected performance targets in dry conditions. Low-End Torque and brake power are limited by the lack of energy at turbine stage and the exhaust gas temperature respectively. The increase of engine displacement is consistently followed by the increment of Low-End Torque, which exceeds the target value for a 5 liters configuration. Indeed, at equal boost pressure, which is limited by the lack of energy at the turbine stage at low engine speed, the larger the displacement, the greater is the air mass flow rate and therefore the maximum load achievable. However, the same increase in engine displacement does not correspond to an increment in brake power at high engine speed. This behavior is explained by Figure 3-14, which illustrates the fuel energy split evolution as a function of the engine displacement. The comparison is performed in dry conditions and exploiting the same level of fuel power. At first, the increase of engine displacement leads to an increment of friction and pumping losses, with a consequent reduction of the effective power.

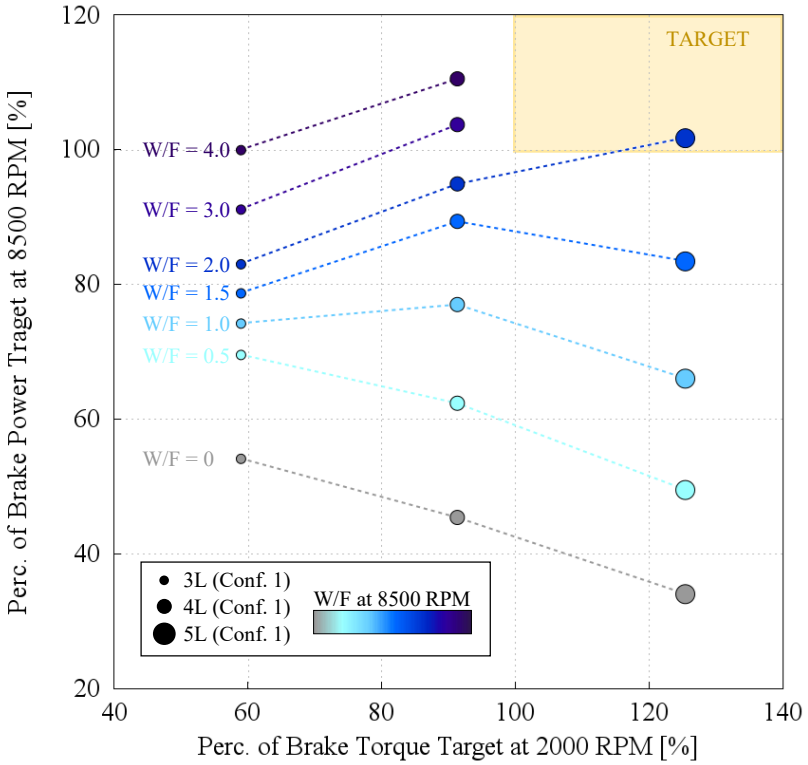


Figure 3-13: Configuration 1 (TC), Water-to-Fuel ratio required at 8500 RPM full-load by different engine displacements as a function of the brake torque achieved at 2000 RPM in dry conditions (x-axis) and the brake power reached at 8500 RPM exploiting PWI (y-axis)

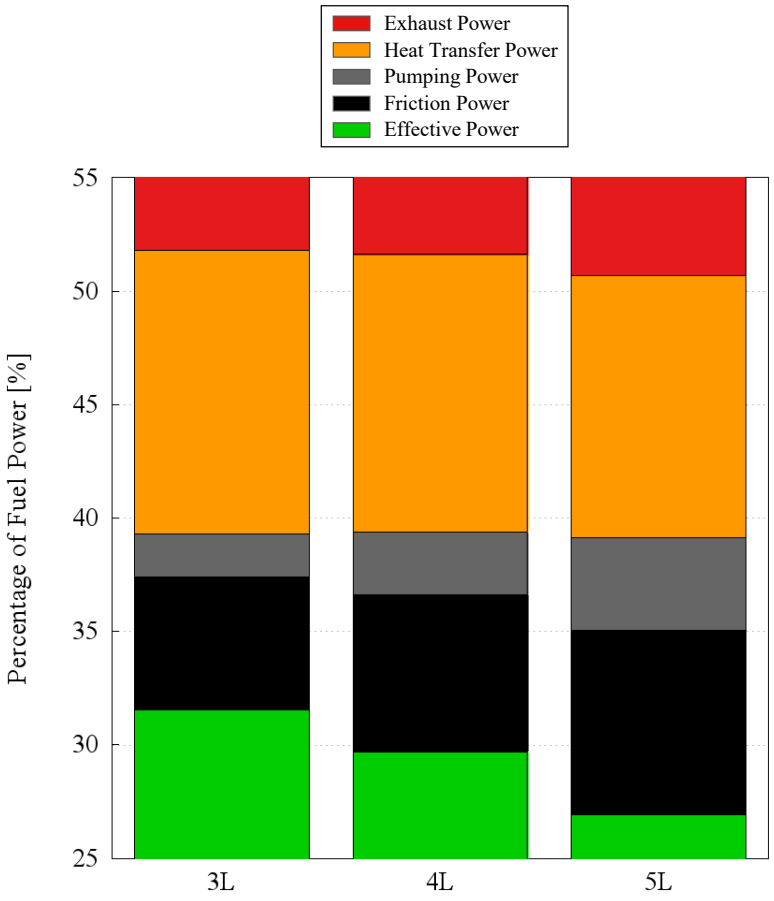


Figure 3-14: Fuel energy split in dry operating conditions, 8500 RPM and 55% of brake power target as a function of engine displacement

Moreover, in addition to a more favorable cylinder surface-to-volume ratio, the lower pressure and therefore the lower density achieved in larger combustion chambers (see Figure 3-15, top) implies a reduction of the in-cylinder heat transfer, thus increasing the exhaust energy loss and therefore the turbine inlet temperature: this implies a larger opening of the wastegate valve to control the exhaust gas temperature, thus further reducing the effective power achievable.

The 3 liters configuration is able to achieve the brake power target only exploiting a W/F close to the maximum allowable, 4. As shown in Figure 3-15, such a high request of water results from a significantly retarded combustion. Indeed, up to about 70% of the power target, MFB50 is kept at knock limit, thus guaranteeing a high brake thermal efficiency. At 70% of the power target, the maximum in-cylinder pressure limit is achieved: from this operating point, each load increase is followed by a strong delay of the MFB50, which is necessary to

avoid a further increment of in-cylinder pressure. The retarded combustion has a detrimental effect on thermodynamic efficiency, on exhaust gas temperature and consequently on water consumption. By increasing the engine displacement, the maximum pressure limit is reached at 90% and 105% of the brake power target for the 4L and 4L configurations respectively. As a result, the Water-to-Fuel required at brake power target reduces up to 2.55 (4L) and 1.95 (5L). The same analysis has been carried out also in reference to configuration 2, as shown in Figure 3-16. In general, this configuration is penalized by the power absorbed by the supercompressor, which is mechanically connected to the crankshaft. Moreover, the maximum brake power achievable is limited by the supercharger pressure ratio. A simple scaling of the map aimed at increasing the pressure ratio was not considered as a feasible solution, cause it would have led to temperatures at the supercompressor outlet exceeding the limit of 160°C. To increase the pressure ratio, an intercooled two stage supercompressors was deemed necessary. However, this solution was not taken into consideration due to the increase in costs, complexity of the system and overall dimensions.

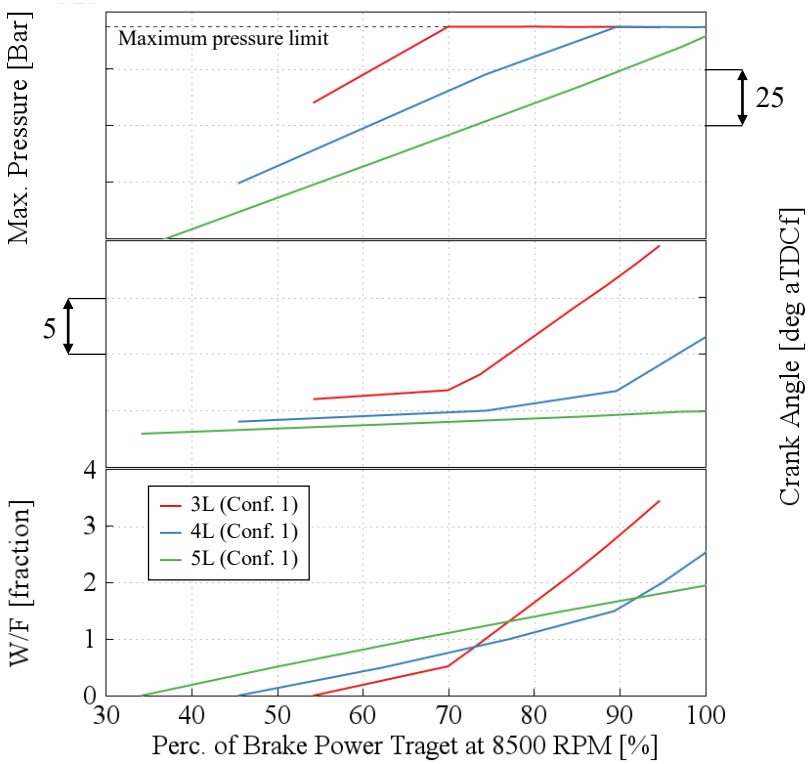


Figure 3-15: Configuration 1 (TC), maximum in-cylinder pressure (top), anchor angle MFB50 (middle), Water-to-Fuel ratio (bottom) as a function of brake power achieved at 8500 RPM with three different levels of engine displacement

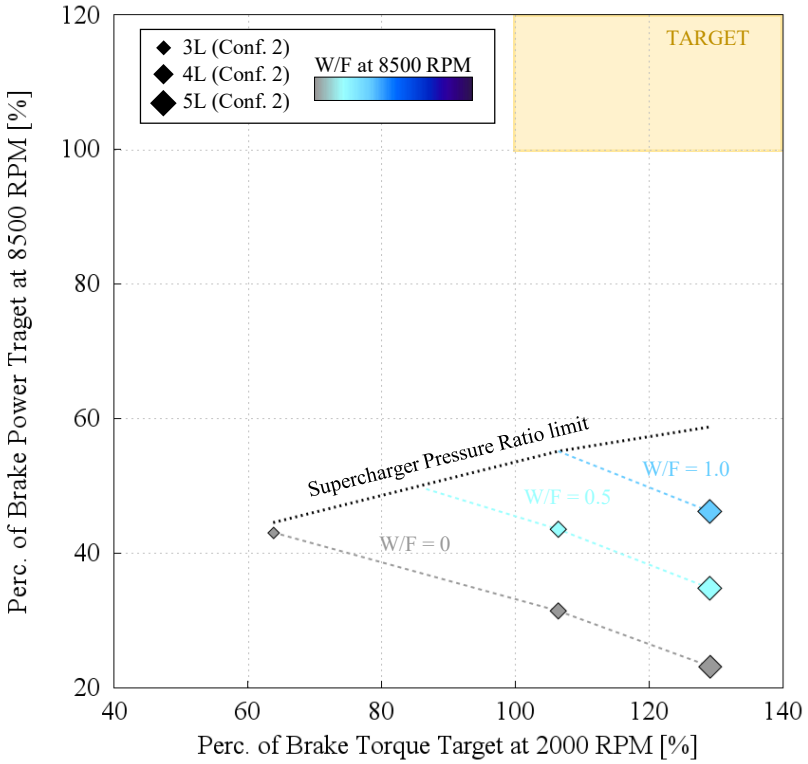


Figure 3-16: Configuration 2 (SC), Water-to-Fuel ratio required at 8500 RPM full-load by different engine displacements as a function of the brake torque achieved at 2000 RPM in dry conditions (x-axis) and the brake power reached at 8500 RPM exploiting PWI (y-axis)

To conclude the investigation on engine displacement variation, a last analysis was carried out at part load. In particular, each variant of configurations 1 and 2 was firstly evaluated in term of maximum torque achieved at 2000 RPM in ultra-lean conditions, i.e. lambda 2.8. Afterwards, the operating point 2000 RPM – 32% of LET target was simulated adopting lambda 1 and, only for the variants that exceeded the target load in ultra-lean conditions, lambda 2.8. The part-load simulation results are reported in Figure 3-17. First of all, only supercharged 4L and 5L as well as turbocharged 5L versions of H2-ICE are able to operate at lambda 2.8 in motorway driving conditions. Exploiting such a lean mixture, thanks to the strong reduction of pumping and heat losses, the brake thermal efficiency increases with a consequent advantage in terms of fuel economy. On the other hand, if operated at lambda 1, the engine is less efficient and the fuel consumption gets worse. Moreover, regardless of mixture composition, lower displacements result in lower fuel consumption.

At the end of this investigation, the configuration 1 variant with 5 liters displacement results the only one capable to respect the WOT performance target

(see Figure 3-13) contemporarily guaranteeing to operate with ultra-lean mixture in the operating point 2000 RPM – 32% of LET target.

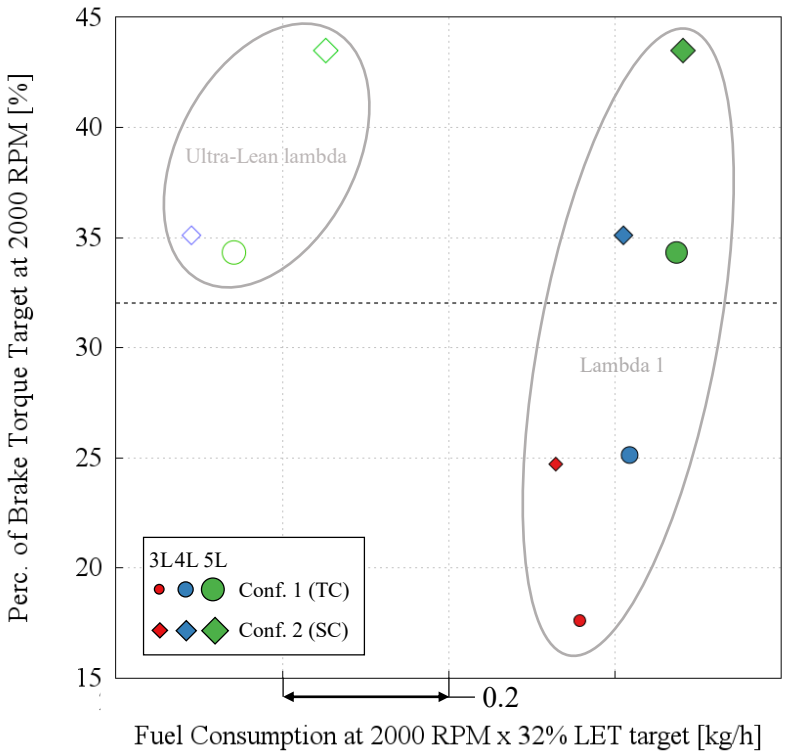


Figure 3-17: Performance of configurations 1 and 2, considering 3 different engine displacements, as a function of maximum torque achieved at 2000 RPM in ultra-lean conditions, i.e. lambda 2.8 (x-axis) and fuel consumption measured at the operating point 2000 RPM – 32% of LET target

With the aim of reducing as much as possible the water consumption of the selected variant, a second DoE methodology was adopted for the definition of the optimal combination of compression ratio and turbocharger size. To carry out the preliminary selection of a bespoke turbocharger, the baseline compressor and turbine maps were scaled following the approach proposed by [98]. First, according to Equation 13, a scaling factor (SF) was defined as the ratio between the scaled and the baseline compressor diameter. Afterwards, in accordance with similarity laws [99], the corrected mass flow of both compressor and turbine was scaled proportionally to the square of the SF while the rotational speed was modified as a function of its inverse (see equations 14 and 15). On the other hand, the pressure ratio multiplier as well as the compressor efficiency were kept constant.

$$SF= \left(\frac{D_{comp,scaled}}{D_{comp,base}}\right)^2 = \left(\frac{D_{turb,scaled}}{D_{turb,base}}\right)^2 \quad (13)$$

$$\text{Mass flow rate multiplier} = SF \quad (14)$$

$$\text{Speed multiplier} = \frac{1}{\sqrt{SF}} \quad (15)$$

The results obtained through this methodology are reported in Figure 3-18. From reference configuration, a larger turbocharger leads to reduced turbine backpressure and a lower water request. On the other hand, at low engine speed, the larger the turbocharger, the lower the energy that can be extracted from the turbine and therefore the maximum LET achievable. As concern the compression ratio, its increase has two opposing effects on exhaust gas temperature. On one hand, thanks to the higher expansion ratio, it helps to cool the exhaust gases more. On the other hand, it increases the knock tendency, thus forcing a more delayed combustion with a detrimental effect on exhaust gas temperature. Indeed, as shown in Figure 3-18 (bottom left), a compression ratio increment of one point leads to a reduction of W/F, meaning that the positive effect of a higher expansion ratio dominates. On the other hand, a further increment of CR makes the water request higher due to the increase of knock likelihood and the consequent delay of MFB50. A scaling factor of 1.12 in conjunction with a compression ratio increase of one point results the optimal solution to reduce the Water-to-Fuel ratio from 1.95 to 1.75 without jeopardizing the Low-End Torque.

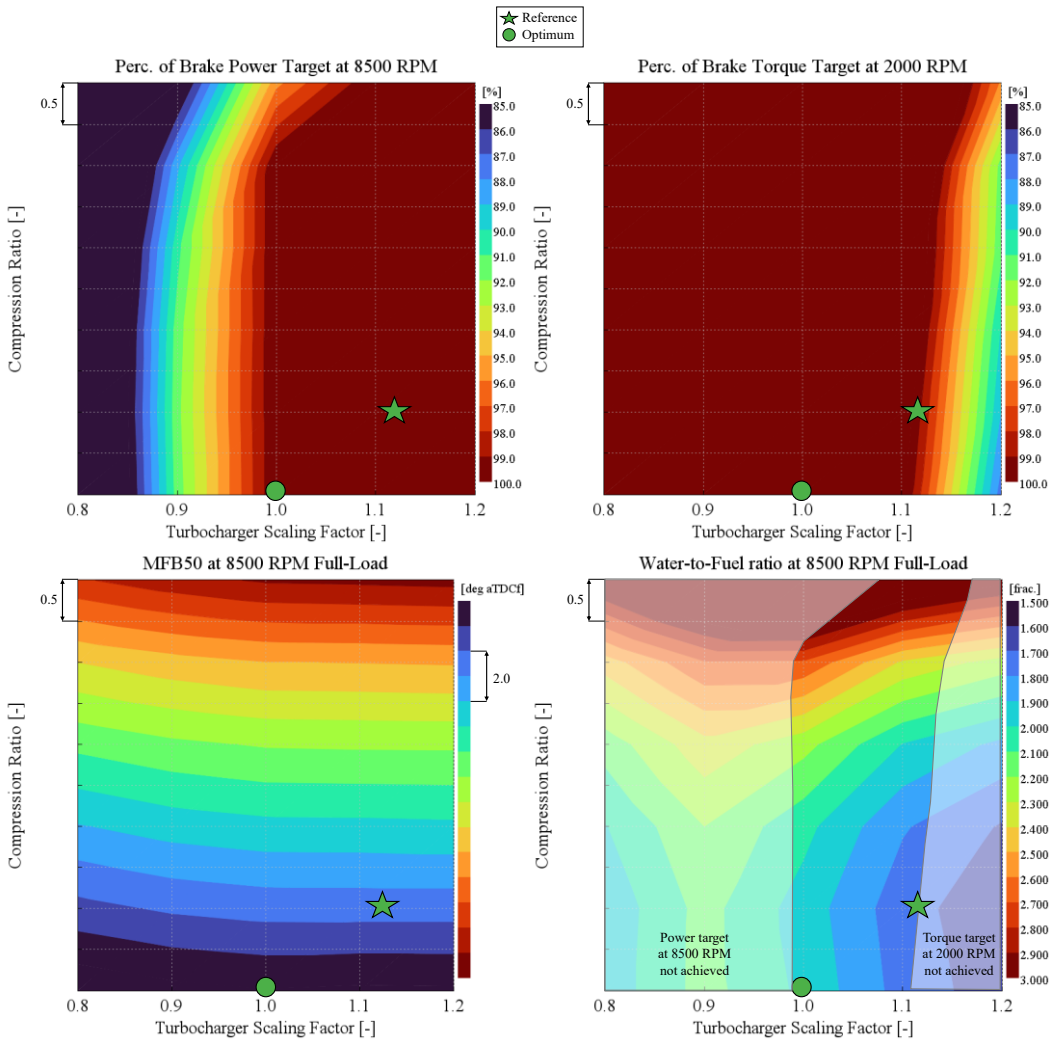


Figure 3-18: Configuration 1 (TC), brake power at 8500 RPM (top-left), brake torque at 2000 RPM (top-right), anchor angle MFB50 (bottom-left) and Water-to-Fuel ratio at 8500 RPM full-load (bottom-right) as a function of turbocharger scaling factor (x-axis) and compression ratio (y-axis)

Engine Maps

In this section, the results of the preliminary architecture optimization activity to assess the potential of the H2-ICE retrofitted from an existing gasoline V6 engine, are presented in terms of complete engine maps. The main engine parameters are reported in Figure 3-19, including engine thermodynamic efficiency, lambda, Water-to-Fuel ratio, intake manifold pressure. Combustion results (anchor angle MFB50 and burn duration MFB10-90), maximum in-cylinder pressure and turbine inlet temperature are reported in Figure 3-20. Starting from the full-load

performance analysis, the Low-End Torque target is successfully achieved thanks to the increment in engine displacement. Moving to higher engine speeds, the increment in turbine inlet temperature forces the injection of water starting from 5500 RPM. The brake power target is achieved exploiting a Water-to-Fuel ratio of 1.75 and 1.82 at 8500 and 9000 RPM respectively. At low engine speed, the full-load curve is mainly limited by the maximum boost pressure that can be provided by the turbocharger system, whose size has been increased to minimize the water demand at high engine speed. On the other hand, at high engine speed, a further increase of engine performance could be achieved by increasing the water consumption. However, having reached the maximum in-cylinder pressure limit, an increase in load would correspond to a strong delay of combustion anchor angle, which would lead to a dramatic deterioration in engine efficiency as well as a significant increment of water demand. The peak of brake thermal efficiency is measured at high loads between 3000 RPM and 4000 RPM. Moving to higher engine speed, the retarded combustion adopted as countermeasure to reduce the knock likelihood implies an engine efficiency worsening. It is worth to highlight that the rate at which MFB50 is retarded decreases as the injected water increases, demonstrating the positive effect of PWI on knock likelihood. Decreasing the engine load, the spark timing is advanced thanks to the higher knock margin, with the aim to increase the engine efficiency. However, despite an MFB50 close to the optimum level of 8÷10 deg after Top Dead Center firing (aTDCf) and a reduced combustion duration, decreasing the load leads to a reduction of thermodynamic efficiency, which is significantly penalized by pumping losses. Concerning the burn duration, it increases as the combustion is retarded. Moreover, a further increase of burn duration is registered when water injection is performed.

The 35% of the maximum torque reached at 2000 RPM results the highest load where the switch from stoichiometric to ultra-lean operations could take place. From the curve obtained at lambda 2.8 (grey line of Figure 3-19), loads adjustment are accomplished by solely varying the relative air/fuel ratio, minimizing the in-cylinder heat transfer and the losses caused by use of the throttle valve. It follows an increase of brake thermal efficiency that, with respect to stoichiometric operations, grows of around 4 percentage points at 2000 RPM. Moreover, the adoption of ultra-lean mixture leads to an increase of boost pressure, to a significant reduction of exhaust gas temperature and, in terms of combustion, to a burn duration lengthening.

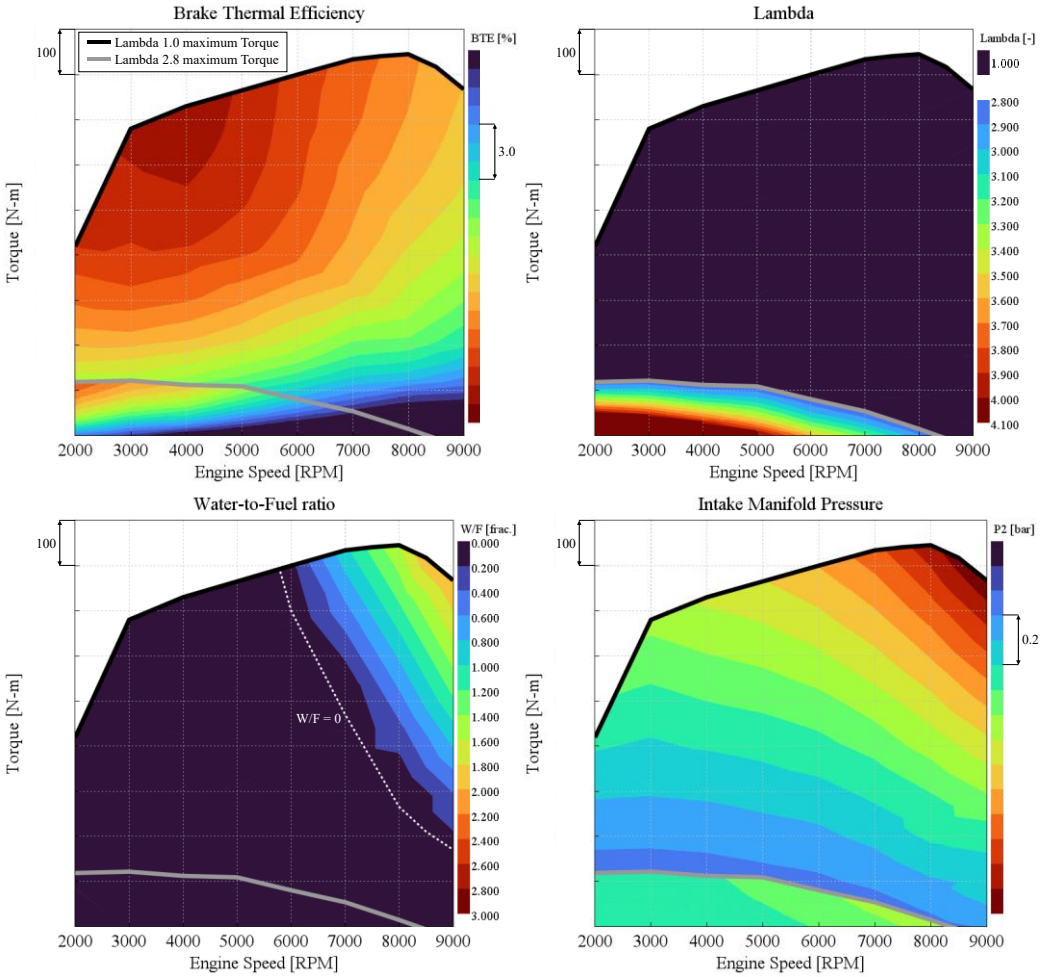


Figure 3-19: Configuration 1 (TC), 5L H2-ICE maps of brake thermal efficiency (top-left), lambda (top-right), Water-to-Fuel ratio (bottom-left) and intake manifold pressure (bottom-right)

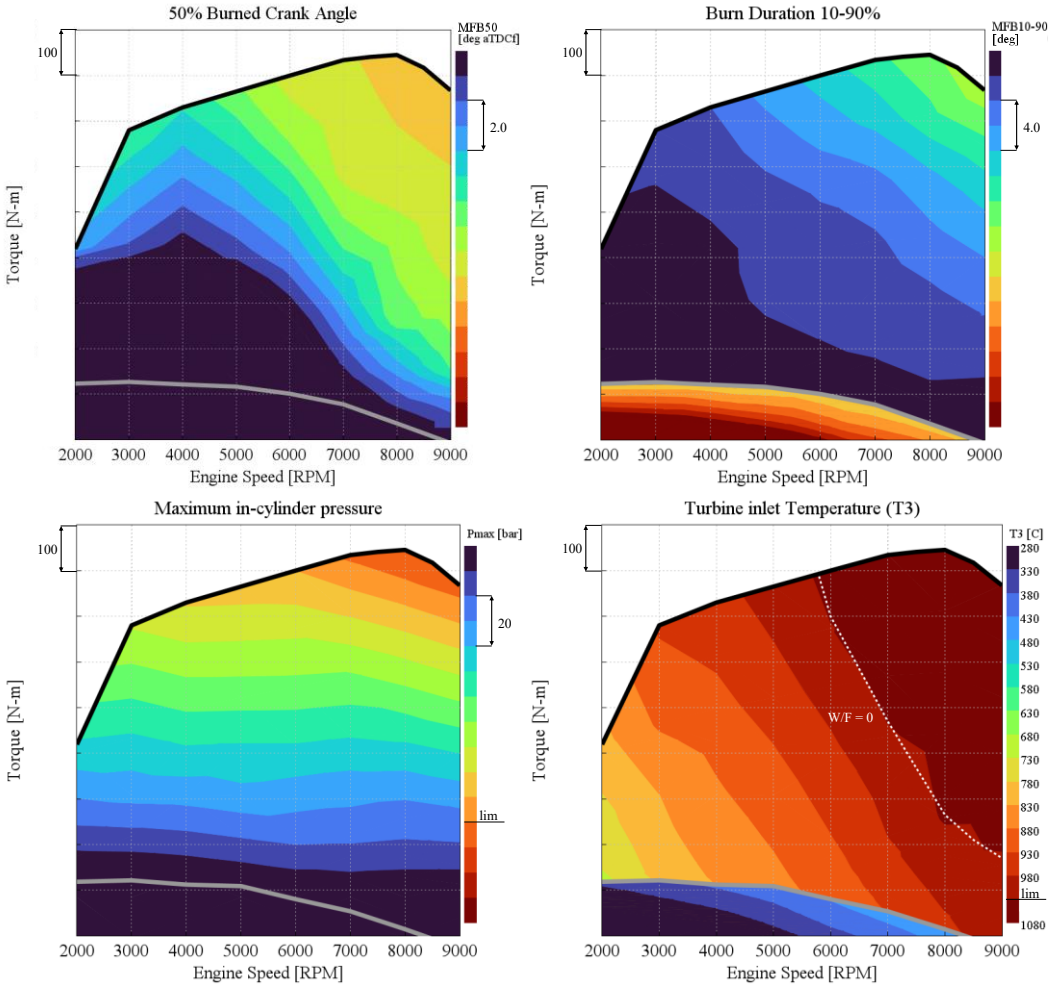


Figure 3-20: Configuration 1 (TC), 5L H2-ICE maps of combustion anchor angle (top-left), burn duration 10-90% (top-right), maximum in-cylinder pressure (bottom-left) and turbine inlet temperature (bottom-right)

3.5 Conclusions

This chapter presents a comprehensive methodology to preliminary drive the design of the engine architecture of a hydrogen-fueled ICE converted from a high performance 3.0L V6 120° Twin Turbocharged Direct Injection Spark Ignition engine. At first, a 3D-CFD methodology was developed to mimic H2 injection in ICE application. This allowed to assess the mixture formation at the end of the compression stroke for different lambda and injector mounting positions. With a start of injection shortly before the Intake Valve Closing to prevent H2 from entering the intake manifold and to avoid a reduction of volumetric efficiency, the highest level of mixture homogeneity is achieved under stoichiometric conditions through an exhaust side mounted injector and a retraction of z = -4 mm. However, since stratification is still present, future investigations will focus on the injector characteristics, increasing the static flow rate and mounting tip caps with optimized design. The research activity continued moving towards the preliminary definition of H2-ICE displacement, compression ratio and turbocharger size. To tackle this task, a combustion model able to account for water content impact on burn duration slow down and a H2 dedicated knock model were defined. The preliminary full-load H2-ICE simulations demonstrated the requirement of an increased displacement (i.e. 5L) to achieve the Low-End Torque target in dry conditions. A higher displacement is also beneficial to reach the desired brake power with an acceptable Water-to-Fuel ratio and to guarantee a satisfactory level of power output in ultra-lean conditions. Finally, the adoption of a bespoke turbocharger in combination with a 1 point higher compression ratio leads to a 10% reduction of water demand. The engine maps generation demonstrates the necessity to inject water at full-load from 5500 RPM, requiring a maximum W/F of 1.82 at 9000 RPM. In future research activities, the computed maps could be embedded in a vehicle model with the aim of estimating hydrogen and water consumption over different driving cycles thus enabling a preliminary sizing of their tank.

Chapter 4

Concluding remarks and Outlook

In the automotive field, the development of new propulsion systems is currently undergoing tremendous transformations. While until a few years ago, the principal focus was to ensure the best performance at high loads and comply with the regulations in place, today the main target, in addition to increased power and excellent performance in transient operations, is carbon neutrality. The push towards a net zero GHG emissions has led the light duty industry to offer a broader than ever powertrain portfolio, comprising pure Internal Combustion Engines, mild-hybrids, Plug-In Hybrids, Battery Electric Vehicles and Fuel Cell Electric Vehicles. As a matter of fact, powertrain electrification represents the most promising solution to improve the air quality in highly congested urban areas. However, the adoption of ICEs powered by alternative fuels capable to achieve a zero impact in their entire life cycle is gaining interest in the automotive community. In particular, among these alternative fuels, hydrogen has recently become a highly attractive solution since it could be produced from renewable energy sources, and its combustion generates almost zero GHG emissions. In recent years, to reduce costs and development time of new engines, companies made an extensive use of numerical simulations. Indeed, the creation of numerical models has the great potential to provide some reliable preliminary analysis of the engine to be developed or optimized. In light of these motivations, in this doctoral work, a CFD methodology to guide a preliminary design of a H2-ICE revamped from a high-performance 3.0L V6 120° Twin Turbocharged Direct Injection Spark Ignition engine was developed. The converted ICE is supposed to achieve a 20% higher brake power with respect to the reference gasoline engine, without jeopardizing the Low-End Torque performance, whose target must be guaranteed without electrical assistance. Despite the adoption of highly lean mixtures results in a high energy conversion efficiency and in very low Nitrogen Oxides emissions, the achievement of such a high specific power makes necessary the exploitation of stoichiometric combustion with the aim to limit the boost and the Charge Air Cooler (CAC) cooling power requirements. In turn, lambda 1 operations leads to knock likelihood increase and higher exhaust gas temperature, making mandatory the

injection of water. For this reason, the first part of this activity focused of Port Water Injection technology. In particular, exploiting a huge set of experimental data collected on a small displacement gasoline engine in dry and wet conditions, the objective was to develop a methodology able to predict, on a physical basis, the impact of the water content on the combustion process and on the knock occurrence likelihood. Once validated, this methodology was firstly exploited to drive a virtual calibration of the reference engine. Afterwards, it allowed to assess the benefits of PWI in combination with other technologies in terms of CO2 emission reduction over different driving cycles. Once acquired a solid background on Port Water Injection technology, the focus returned to the hydrogen engine. With the aim to perform a preliminary design of H2-ICE architecture, a first methodology capable to properly replicate the H2 injection behavior under different injector positions, injection pressure and chamber pressure, was developed. This methodology allowed a preliminary assessment of H2-air mixture formation, proving that mixture homogenization could be enhanced by injecting hydrogen in the same direction of tumble motion, and mounting the injector with a retraction higher than 2 mm so as to maximize the jet penetration. On the other hand, to perform a H2-ICE performance analysis, a 1D-CFD methodology was built. The latter inherited the Port-Puddling and the evaporation model developed in the first part of the activity. Concerning the combustion model, in absence of experimental data, a numerical approach was adopted. In particular, assuming that the turbulence effect on flame front speed of hydrogen and gasoline are comparable, the gasoline burn duration (experimentally measured) has been scaled as a function of the ratio between hydrogen and gasoline LFSs. As for knock, a phenomenological model based on Livengood and Wu approach was developed. The preliminary full-load H2-ICE simulations demonstrated the requirement of an increased displacement (i.e. 5L) to achieve the Low-End Torque target in dry conditions. A higher displacement is also beneficial to reach the desired brake power with an acceptable Water-to-Fuel ratio and to guarantee a satisfactory level of power output in ultra-lean conditions. Finally, the adoption of a bespoke turbocharger in combination with a 1 point higher compression ratio leads to a 10% reduction of water demand. The engine maps generation demonstrates the necessity to inject water at full-load from 5500 RPM, requiring a maximum W/F of 1.82 at 9000 RPM.

In future research activities, the computed maps could be embedded in a vehicle model with the aim of estimating hydrogen and water consumption over different driving cycles thus enabling a preliminary sizing of their tank. However, in the process of building up a reliable virtual engine dedicated for hydrogen development, the primary objective will be the validation of the proposed

combustion model against experimental data. In parallel, the calibration of a NOx emissions model [24] and the development of mono-dimensional models of TWC and NOx trap will be essential to prove whether the proposed H2-ICE concept, in different driving conditions, respects the emission limits proposed by the most recent regulations. A further activity will be devoted to the development of a vECU capable to manage the lambda 1 - lambda lean transitions with the aim to avoid power output discontinuity. As for hydrogen injection, future investigations will focus on the injector characteristics, increasing the static flow rate and mounting tip caps with the aim to further enhance mixture homogenization.

Keeping in mind the points that should be further investigated to improve the model reliability, and attempting to have a baseline experimental evidence, the proposed methodologies can already be exploited as a supporting tool for the development and optimization of a new hydrogen engine.

References

1. International Energy Agency, “CO2 emissions in 2022,” 2022, https://iea.blob.core.windows.net/assets/3c8fa115-35c4-4474-b237-1b00424c8844/CO2Emissionsin2022.pdf, accessed June 2023.

2. Our World In Data, "CO2 Emissions," 2023, https://ourworldindata.org/co2-emissions, accesseed june 2023.

3. Korn, T., “Der effizienteste Weg zur CO2-Minderung: die neueste Generation von Wasserstoffverbrennungsmotoren [The Most Efficient Way for CO2 Reduction: The New Generation of Hydrogen Internal Combustion Engines Summary],” in *41th International Vienna Motor Symposium*, Vienna, 2020.

4. Dilara, P., “The Future of Clean Cars in Europe: EU Green Deal and EURO 7,” in *4th Sino-EU Workshop on New Emissions Standards and Regulations for Motor Vehicles*, Virtual event jointly organised by the Vehicle Emission Control Center (China) and the Joint Research Centre, 2021.

5. European Commission, “Communication from the Commission to the European Parliament, the Council, the European Economic and Social Committee and the Committee of the Regions a Hydrogen Strategy for a ClimateNeutral Europe,” COM/2020/301 Final, Brussels, 2020, https://eur-lex.europa.eu/legal-content/EN/TXT/?qid=1594897267722&uri=CELEX:52020DC0301, accessed June 2023.

6. European Commission, “European Clean Hydrogen Alliance,” 2020, https://ec.europa.eu/growth/industry/policy/european-clean-hydrogen-alliance_en, accessed June 2023.

7. Yip, H.L., Srna, A., Yuen, A.C.Y., Kook, S. et al., “A Review of Hydrogen Direct Injection for Internal Combustion Engines: Towards Carbon-Free Combustion,” *Applied Sciences* 9, no. 22 (2019): 4842, https://doi.org/10.3390/app9224842.

8. Banerjee, S., Musa, M.N., Jaafar, A.B., “Economic assessment and prospect of hydrogen generated by OTEC as future fuel, ” *International Journal of Hydrogen Energy* 42, no. 1 (2017): 26–37, https://doi.org/10.1016/j.ijhydene.2016.11.115.

9. Deloitte, “Green hydrogen: Energizing the path to net zero,” 2023, https://www.deloitte.com/content/dam/assets-shared/docs/gx-deloitte-green-hydrogen-report-2023.pdf, accessed June 2023.

10. Cornell, A., “Hydrogen production by electrolysis, ” In Proceedings of the *1st International Conference on Electrolysis*, Copenhagen, Denmark, 2017, https://energiforskmedia.blob.core.windows.net/media/23562/5-hydrogen-production-by-electrolysis-ann-cornell-kth.pdf, accessed on June 2023.

11. Helmolt, R.V.; Eberle, U., “Fuel cell vehicles: Status 2007,” *Journal of Power Sources* 165, no. 2 (2007): 833-843, https://doi.org/10.1016/j.jpowsour.2006.12.073.

12. Manoharan, Y., Hosseini, S.E., Butler, B., Alzhahrani, H. et al., “Hydrogen Fuel Cell Vehicles: Current Status and Future Prospect,” *Applied Sciences* 9, no. 11 (2019): 2296, https://doi.org/10.3390/app9112296.

13. Enke, W., Gruber, M., Hecht, L., and Staar, B., “Der bivalente V12-Motor des BMW Hydrogen 7,” *MTZ-Motortechnische Zeitschrift* 68 (2007): 446-453, https://doi.org/10.1007/ BF03227411.

14. Mazda, “MAZDA: Hydrogen Rotary Vehicle,” https://newsroom.mazda.com/en/technology/1426/index.html, accessed June 2023.

15. MAN and Shell, “Shell, MAN and Connexxion Planning Worlds Largest Hydrogen Public Transport Project,” in *Green Car Congress*, 2006, https://www.greencarcongress.com/2006/06/shell_man_and_c.html, accessed June 2023.

16. Pauer, T., Weller, H., Schünemann, E., Eichlseder, H. et al., “H2 ICE for

Future Passenger Cars and Light Commercial Vehicles," in *41th International Vienna Motor Symposium*, Vienna, 2020.

17. Babayev, R., Andersson, A., Dalmau, A.S., Im, H.G. et al., "Computational Characterization of Hydrogen Direct Injection and Nonpremixed Combustion in a Compression- Ignition Engine," *International Journal of Hydrogen Energy* 46, no. 35 (2021): 18678-18696, https://doi.org/10.1016/j.ijhydene.2021.02.223.

18. Tsujimura, T. and Suzuki, Y., "The Utilization of Hydrogen in Hydrogen/Diesel Dual Fuel Engine," *International Journal of Hydrogen Energy* 42, no. 19 (2017): 14019-14029, https://doi.org/10.1016/j.ijhydene.2017.01.152.

19. Saravanan, N., Nagarajan, G., Sanjay, G., Dhanasekaran, C. et al., "Combustion Analysis on a DI Diesel Engine with Hydrogen in Dual Fuel Mode," *Fuel* 87, no. 17-18 (2008): 3591-3599, https://doi.org/10.1016/j.fuel.2008.07.011.

20. Dhyani, V. and Subramanian, K.A., "Fundamental Characterization of Backfire in a Hydrogen Fuelled Spark Ignition Engine Using CFD and Experiments," *International Journal of Hydrogen Energy* 44, no. 60 (2019): 32254-32270, https://doi.org/10.1016/j.ijhydene.2019.10.077.

21. White, C.M., Steeper, R.R., and Lutz, A.E., "The Hydrogen-Fueled Internal Combustion Engine: A Technical Review," *International Journal of Hydrogen Energy* 31, no. 10 (2006): 1292-1305, https://doi.org/10.1016/j.ijhydene.2005.12.001.

22. Ozcanli, M., Baş, O., Akar, M., Yıldızhan, Ş., and Serin, H., "Recent studies on hydrogen usage in Wankel SI engine," *International Journal of Hydrogen Energy* 43, no. 38 (2018): 18037-18045, https://doi.org/10.1016/j.ijhydene.2018.01.202.

23. Thomas Koch, D., Sousa, A., and Bertram, D., "H2-Engine Operation with EGR Achieving High Power and High Efficiency Emission-Free Combustion," *SAE Technical Paper* 2019-01-2178, 2019, https://doi.org/10.4271/2019-01-2178.

24. Millo, F., Piano, A., Rolando, L., Accurso, F., Gullino, F., Roggio, S., Bianco, A., Pesce, F., Vassallo, A., and Rossi, R., "Synergetic Application of Zero-, One-, and Three-Dimensional Computational Fluid Dynamics Approaches for Hydrogen-Fuelled Spark Ignition Engine Simulation," *SAE Int. J. Engines* 15(4):3–15, 2021, doi:10.4271/03-15-04-0030..

25. Senecal, K. and Leach, F., “Racing Toward Zero,” 2021, ISBN 978-1-4686-0146-6.

26. Stępień, Z., “A Comprehensive Overview of Hydrogen-Fueled Internal Combustion Engines: Achievements and Future Challenges,” *Energies* 14(20), 2021, https://doi.org/10.3390/en14206504.

27. Zheng, J., Liu, X., Xu, P., Liu, P., Zhao, Y., and Yang, J., “Development of High Pressure Gaseous Hydrogen Storage Technologies,” I*nternational Journal of Hydrogen Energy* 37, no. 1 (2012): 1048–1057, https://doi.org/10.1016/j.ijhydene.2011.02.125.

28. Wallner, T., Lohse-busch, H., Gurski, S., Duoba, M., Thiel, W., Martin, D., and Korn, T., “Fuel economy and emissions evaluation of BMW Hydrogen 7 Mono-Fuel demonstration vehicles,” *International Journal of Hydrogen Energy* 33, no. 24 (2008):7607–7618, https://doi.org/10.1016/j.ijhydene.2008.08.067.

29. Kapus, P.,Heindl, R., Weißbäck, M., and Grabner, P., “High Efficiency Hydrogen Internal Combustion Engine – Carbon Free Powertrain for Passenger Car Hybrids and Commercial Vehicles,” in *43th International Vienna Motor Symposium*, Vienna, 2022.

30. Berckmüller, M., Rottengruber, H., Eder, A., Brehm, N. et al., “Potentials of a Charged SI-Hydrogen Engine,” *SAE Technical Paper* 2003-01-3210, 2003, https://doi.org/10.4271/2003-01-3210.

31. Wan, J., Zhuang, Y., Huang, Y., Qian, Y., and Qian, L., "A review of water injection application on spark-ignition engines," *Fuel Processing Technology*, v. 221, pp. 106956, 2021, https://doi.org/10.1016/j.fuproc.2021.106956.

32. Falfari, S., Bianchi, G., Cazzoli, G., Ricci, M. et al., "Water Injection Applicability to Gasoline Engines: Thermodynamic Analysis," *SAE Technical Paper* 2019-01-0266, 2019, https://doi.org/10.4271/2019-01-0266.

33. Zhu, S., Hu, B., Akehurst, S., Copeland, C., Lewis, A., Yuan, H., Kennedy, I., Bernards, J., and Branney, C., "A review of water injection applied on the internal combustion engine," *Energy Conversion Management*, v. 184, 2019, https://doi.org/10.1016/j.enconman.2019.01.042.

34. Cazzoli, G., Bianchi, G., Falfari, S., Ricci, M. et al., "Evaluation of Water and EGR Effects on Combustion Characteristics of GDI Engines Using a Chemical Kinetics Approach," *SAE Technical Paper* 2019-24-0019, 2019,

https://doi.org/10.4271/2019-24-0019.

35. De Bellis, V., Bozza, F., Teodosio, L., and Valentino, G., "Experimental and Numerical Study of the Water Injection to Improve the Fuel Economy of a Small Size Turbocharged SI Engine," *SAE Int. J. Engines* 10(2):550-561, 2017, https://doi.org/10.4271/2017-01-0540.

36. Gern, M., Vacca, A., and Bargende, M., "Experimental Analysis of the Influence of Water Injection Strategies on DISI Engine Particle Emissions," *SAE Int. J. Adv. & Curr. Prac. in Mobility* 2(2):598-606, 2020, https://doi.org/10.4271/2019-24-0101.

37. Vacca, A., Bargende, M., Chiodi, M., Franken, T. et al., "Analysis of Water Injection Strategies to Exploit the Thermodynamic Effects of Water in Gasoline Engines by Means of a 3D-CFD Virtual Test Bench," *SAE Technical Paper* 2019-24-0102, 2019, https://doi.org/10.4271/2019-24-0102.

38. Durst, B., Landerl, C., Poggel, J., and Schwarz, C., "BMW Water Injection: Initial Experience and Future Potentials. ," *38th International Vienna Motor Symposium*, Vienna, 2017.

39. Battistoni, M., Grimaldi, C., Cruccolini, V., Discepoli, G. et al., "Assessment of Port Water Injection Strategies to Control Knock in a GDI Engine through Multi-Cycle CFD Simulations," *SAE Technical Paper* 2017-24-0034, 2017, https://doi.org/10.4271/2017-24-0034.

40. Hoppe, F., Thewes, M., Seibel, J., Balazs, A. et al., "Evaluation of the Potential of Water Injection for Gasoline Engines," *SAE Int. J. Engines* 10(5):2500-2512, 2017, https://doi.org/10.4271/2017-24-0149.

41. Zembi, J., Battistoni, M., Ranuzzi, F., Cavina, N., and Cesare, M. De, "CFD analysis of port water injection in a GDI engine under incipient knock conditions," *Energies* 12(18), 2019, https://doi.org/10.3390/en12183409.

42. Millo, F., Mirzaeian, M., Rolando, L., Bianco, A., and Postrioti, L., "A methodology for the assessment of the knock mitigation potential of a port water injection system," *Fuel* v. 283, 2021, https://doi.org/10.1016/j.fuel.2020.119251.

43. Paltrinieri, S., Mortellaro, F., Silvestri, N., Rolando, L. et al., "Water Injection Contribution to Enabling Stoichiometric Air-to-Fuel Ratio Operation at Rated Power Conditions of a High-Performance DISI Single Cylinder Engine," *SAE Technical Paper* 2019-24-0173, 2019,

https://doi.org/10.4271/2019-24-0173.

44. Tornatore, C., Siano, D., Marchitto, L., Iacobacci, A. et al., "Water Injection: a Technology to Improve Performance and Emissions of Downsized Turbocharged Spark Ignited Engines," *SAE Int. J. Engines* 10(5):2319-2329, 2017, https://doi.org/10.4271/2017-24-0062.

45. Wilson, J.P., "Effects of Water Injection and Increased Compression Ratio in a Gasoline Spark Ignition Engine," *Master's Thesis*, Mechanical Engineering, University of Idaho, Moscow, ID, USA, 2011.

46. Doria, A. Stroppiana, M. Ferrera, F. Millo, M. Mirzaeian, D.P. V., "Knock Mitigation Techniques for highly boosted downsized SI engines," *Internaltional Congress SIA Powertrain*, Versailles, France, 2016.

47. Bozza, F., De Bellis, V., Teodosio, L., Tufano, D. et al., "Techniques for CO2 Emission Reduction over a WLTC. A Numerical Comparison of Increased Compression Ratio, Cooled EGR and Water Injection," *SAE Technical Paper* 2018-37-0008, 2019, https://doi.org/10.4271/2018-37-0008.

48. Millo, F., Rolando, L., and Andreat, M., "Numerical Simulation for Vehicle Powertrain Development," Numerical Analysis - Theory and Application, (IntechOpen, 2011), doi:10.5772/24111.

49. Millo, F., Gullino, F., and Rolando, L., "Methodological approach for 1D simulation of port water injection for knock mitigation in a turbocharged DISI engine," *Energies* 13(17), 2020, https://doi.org/10.3390/en13174297.

50. Doria, A. Stroppiana, M. Ferrera, F. Millo, M. Mirzaeian, D.P. V., "Knock Mitigation Techniques for highly boosted downsized SI engines," *Internaltional Congress SIA Powertrain*, Versailles, France, 2016.

51. De Martino, C., Maiorana, G., Pallotti, P., Quinto, S., Sacco, D., "The Global Small Engine 3 and 4 Cylinder Turbo: The New FCA's Family of Small High-Tech Gasoline Engines," In Proceedings of the *39th International Vienna Motor Symposium*, Vienna, Austria, 26–27 April 2018.

52. Wahiduzzaman, S., Moral, T., and Sheard, S., "Comparison of Measured and Predicted Combustion Characteristics of a Four-Valve S.I. Engine," *SAE Technical Paper* 930613, 1993, https://doi.org/10.4271/930613.

53. Gamma Technologies, "GT-SUITE Engine Performance Manual v2022," 2022.

54. Mirzaeian, M., Millo, F., and Rolando, L., "Assessment of the Predictive Capabilities of a Combustion Model for a Modern Downsized Turbocharged SI Engine," *SAE Technical Paper* 2016-01-0557, 2016, https://doi.org/10.4271/2016-01-0557.

55. Zhao, L., Moiz, A.A., Som, S., Fogla, N., Bybee, M., Wahiduzzaman, S., Mirzaeian, M., Millo, F., and Kodavasal, J., "Examining the role of flame topologies and in-cylinder flow fields on cyclic variability in spark-ignited engines using large-eddy simulation," *International Journal of Engine Research* 19(8):886–904, 2018, doi:10.1177/1468087417732447.

56. Millo, F., Rolando, L., Pautasso, E., and Servetto, E., "A Methodology to Mimic Cycle to Cycle Variations and to Predict Knock Occurrence through Numerical Simulation," *SAE Technical Paper* 2014-01-1070, 2014, https://doi.org/10.4271/2014-01-1070.

57. Livengood, J.C. and Wu, P.C., "Correlation of Autoignition Phenomena in Internal Combustion Engines and Rapid Compression Machines," *Symposium (International) on Combustion* 5, no. 1 (1955): 347-355, https://doi.org/10.1016/S0082-0784(55)80047-1.

58. By, A., Kempinski, B., and Rife, J., "Knock in Spark Ignition Engines," *SAE Technical Paper* 810147, 1981, https://doi.org/10.4271/810147.

59. Belli, M., Danieli, G., Amelio, M., Bova, S. et al., "A Detonation Model in Spark-Ignition Engines: Preliminary Results on Engine Octane Requirement," *SAE Technical Paper* 841338, 1984, https://doi.org/10.4271/841338.

60. Douaud, A. and Eyzat, P., "Four-Octane-Number Method for Predicting the Anti-Knock Behavior of Fuels and Engines," *SAE Technical Paper* 780080, 1978, https://doi.org/10.4271/780080.

61. Paltrinieri, S., Mortellaro, F., Silvestri, N., Rolando, L. et al., "Water Injection Contribution to Enabling Stoichiometric Air-to-Fuel Ratio Operation at Rated Power Conditions of a High-Performance DISI Single Cylinder Engine," *SAE Technical Paper* 2019-24-0173, 2019, https://doi.org/10.4271/2019-24-0173.

62. Onorati, A. and Montenegro, G., "1D and Multi-D Modeling Techniques for IC Engine Simulation," 2020, ISBN 9780768099522.

63. European Union, " Establishing a framework for the approval of motor vehicles and their trailers, and of systems, components and separate technical units intended for such vehicles," DIRECTIVE 2007/46/EC, OJ L

263, 9.10.2007, p. 1–160., https://eur-lex.europa.eu/legal-content/EN/TXT/PDF/?uri=CELEX:02007L0046-20160101&from=IT, accessed June 2023.

64. Gearshift Calculation Tool, https://wiki.unece.org/display/trans/Gearshift+calculation+tool, accessed June 2023.

65. European Eunion, "COMMISSION REGULATION (EU) 2017/1151, OJ L 175, 7.7.2017, pp. 1–643., https://eur-lex.europa.eu/legal-content/EN/TXT/?uri=OJ:L:2017:175:TOC, accessed June 2023.

66. Millo, F., Lorenzo, G. di, Servetto, E., Capra, A., and Pettiti, M., "Analysis of the performance of a turbocharged s.i. engine under transient operating conditions by means of fast running models," *SAE Int. J. Engines* 6(2):968–978, 2013, https://doi.org/10.4271/2013-01-1115.

67. DieselNet - Emission Test Cycles, https://dieselnet.com/standards/cycles/index.php, accessed June 2023.

68. Rolando, L., Millo, F., Pulvirenti, F., and Medda, M., "Supercar Hybridization: A Synergic Path to Reduce Fuel Consumption and Improve Performance," *SAE Technical Paper* 2018-37-0009, 2018, doi: 10.4271/2018-37-0009.

69. Verhelst, S., De Landtsheere, J., De Smet, F., Billiouw, C. et al., "Effects of Supercharging, EGR and Variable Valve Timing on Power and Emissions of Hydrogen Internal Combustion Engines," *SAE Int. J. Engines* 1(1):647-656, 2009, https://doi.org/10.4271/2008-01-1033.

70. Le Moine, J., Senecal, P.K., Kaiser, S.A., Salazar, V.M. et al., "A Computational Study of the Mixture Preparation in a Direct-Injection Hydrogen Engine," *J. Eng. Gas Turbines Power* 137, no. 11 (2015): 111508, https://doi.org/10.1115/1.4030397.

71. Gerke, U. and Boulouchos, K., "Three-Dimensional Computational Fluid Dynamics Simulation of Hydrogen Engines Using a Turbulent Flame Speed Closure Combustion Model," I*nternational Journal of Engine Research* 13, no. 5 (2012): 464-481, https://doi.org/10.1177/1468087412438796.

72. Klepatz, K., Rottengruber, H., Zeilinga, S., Koch, D. et al., "Loss Analysis of a Direct-Injection Hydrogen Combustion Engine," *SAE Technical Paper* 2018-01-1686, 2018, https://doi.org/10.4271/2018-01-1686.

73. Scarcelli, R., Wallner, T., Obermair, H., Salazar, V.M. et al., "CFD and Optical Investigations of Fluid Dynamics and Mixture Formation in a DI-H2ICE," in *ASME 2010 Internal Combustion Engine Division Fall Technical Conference*, San Antonio, TX, 2010, https://doi.org/10.1115/ICEF2010-35084.

74. Wallner, T., Matthias, N., and Scarcelli, R., "Influence of Injection Strategy in a High-Efficiency Hydrogen Direct Injection Engine," *SAE Int. J. Fuels Lubr.* 5, no. 1 (2012): 289-300, https://doi.org/10.4271/2011-01-2001.

75. Scarcelli, R., Wallner, T., Matthias, N., Salazar, V. et al., "Mixture Formation in Direct Injection Hydrogen Engines: CFD and Optical Analysis of Single- and Multi-Hole Nozzles," *SAE Int. J. Engines* 4, no. 2 (2011): 2361-2375, https://doi.org/10.4271/2011-24-0096.

76. Verhelst, S., Woolley, R., Lawes, M., and Sierens, R., "Laminar and Unstable Burning Velocities and Markstein Lengths of Hydrogen-Air Mixtures at Engine-Like Conditions," *Proceedings of Combustion Institute* 30, no. 1 (2005): 209-216, https://doi.org/10.1016/j.proci.2004.07.042.

77. Ó Conaire, M., Curran, H.J., Simmie, J.M., Pitz, W.J. et al., "A Comprehensive Modeling Study of Hydrogen Oxidation," *Int. J. Chem. Kinet.* 36, no. 11 (2004): 603-622, https://doi.org/10.1002/kin.20036.

78. Li, H. and Karim, G.A., "Knock in Spark Ignition Hydrogen Engines," *International Journal of Hydrogen Energy* 29, no. 8 (2004): 859-865, https://doi.org/10.1016/j.ijhydene.2003.09.013.

79. Paltrinieri, S., Olcuire, M., Calia, V., Mortellaro, F. et al., "Experimental and Numerical Investigation of Hydrogen Injection and its Preliminary Impact on High Performance Engines Development," *SAE Technical Paper* 2023-01-0402, 2023, https://doi.org/10.4271/2023-01-0402.

80. Harrop, "HTV1900 SUPERCHARGER," https://www.harrop.com.au/htv1900-supercharger, accessed June 2023.

81. Settles, G.S., "Schlieren and Shadowgraph Techniques: Visualizing Phenomena in Transparent Media, " 2001, ISBN 978-3-642-63034-7.

82. Lejsek, D., Leick, P., Jochmann, P., Grabner, P. et al., "Analysis of Mixture Formation and Combustion in H2 Engines for Passenger Cars and Light Commercial Vehicles," *9th International Engine Congress*, Baden-Baden, 2022.

83. Stratford, B.S., "The Calculation of the Discharge Coefficient of Profiled

Choked Nozzles and the Optimum Profile for Absolute Air Flow Measurement," *The Areonautical Jurnal*. 68, no.640 (1964): 237-245, https://doi.org/10.1017/S0001924000060905.

84. Ingle, R., Rao, V.S., Mohan, S., Dai, Y. et al., "Modelling of Flashing in Capillary Tubes using Homogeneous Equilibrium Approach," *Procedia IUTAM* 15: 286-292, https://doi.org/10.1016/j.piutam.2015.04.040.

85. Zhong, W., Mahmoud, N., and Wang, Q., "Numerical Study of Spray Combustion and Soot Emission of Gasoline-Biodiesel Fuel under Gasoline Compression Ignition-Relevant Conditions," *Fuel*, https://doi.org/10.1016/j.fuel.2021.122293.

86. Tang, M., "Spray and Combustion Studies of High Reactivity Gasoline in Comparison to Diesel under Advanced Compression Ignition Engine Conditions," *Dissertation, Michigan Technological University*, 2018, https://doi.org/10.37099/mtu.dc.etdr/686.

87. Chen, S. and Flynn, P., "Development of a Single Cylinder Compression Ignition Research Engine, " SAE Technical Paper 650733, 1965, https://doi.org/10.4271/650733.

88. G. Woschni, "A Universally Applicable Equation for the Instantaneous Heat Transfer Coefficient in the Internal Combustion Engine," *SAE Transactions*, vol. 76, p. 3065, 1967.

89. Alam, S.S. and Depcik, C., "Adaptive Wiebe Function Parameters for a Port-Fuel Injected Hydrogen-Fueled Engine," in Proceedings of *ASME International Mechanical Engineering Congress and Exposition IMECE2019*, Salt Lake City, UT, 2019, https://doi.org/10.1115/IMECE2019-10031

90. Kunal, R., Natarajan, S., Abraham, M., Subash, G. et al., "Effects of Governing Parameters on the Performance and Emissions of Hydrogen Engine for Automotive Application," *SAE Technical Paper* 2013-01-2891, 2013, https://doi.org/10.4271/2013-01-2891.

91. Rezaei, R., Hayduk, C., Sens, M., Fandakov, A., et al., "Hydrogen Combustion—A Puzzle Piece of Future Sustainable Transportation!," in Proceedings of *SIA 2020 Digital Powertrain & Energy*, France, 2020, 304-311.

92. D'Errico, G., Onorati, A., and Ellgas, S., "1D Thermo-Fluid Dynamic Modelling of an S.I. Single-Cylinder H2 Engine with Cryogenic Port Injection," *International Journal of Hydrogen Energy* 33, no. 20 (2008):

5829-5841, https://doi.org/10.1016/j.ijhydene.2008.05.096.

93. Orbaiz, P., Brear, M., Abbasi, P., and Dennis, P., "A Comparative Study of a Spark Ignition Engine Running on Hydrogen, Synthesis Gas and Natural Gas," *SAE Technical Paper* 2013-01-0229, 2013, https://doi.org/10.4271/2013-01-0229.

94. Boretti, A.A. and Watson, H.C., "Enhanced combustion by jet ignition in a turbocharged cryogenic port fuel injected hydrogen engine," *Int. J. Hydrogen Energy* 34(5):2511–2516, 2009, doi:10.1016/j.ijhydene.2008.12.089.

95. Boretti, A., "Stoichiometric H2ICEs with water injection," *International Journal of Hydrogen Energy* 36, no.7 (2011):4469–4473, https://doi.org/10.1016/j.ijhydene.2010.11.117.

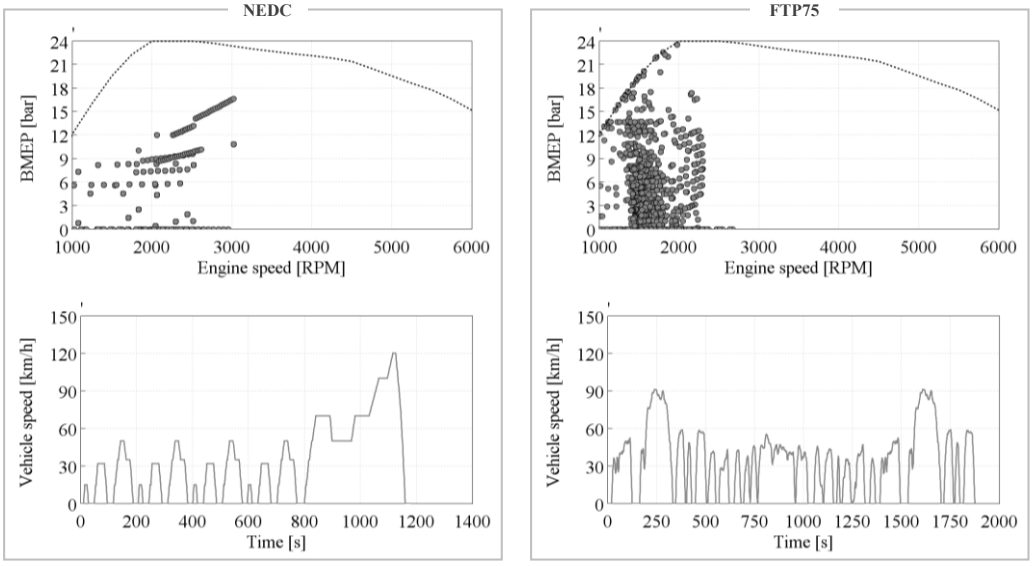
96. Sadiq Al-Baghdadi, M.A.R., "Development of a Pre-ignition Submodel for Hydrogen Engines," *Proceedings of the Institution of Mechanical Engineers, Part D: Journal of Automobile Engineering* 219, no. 10 (2005): 1203-1212, https://doi.org/10.1243/095440705X34883.

97. Millo, F., Pautasso, E., Delneri, D., and Troberg, M., "A DoE Analysis on the Effects of Compression Ratio, Injection Timing, Injector Nozzle Hole Size and Number on Performance and Emissions in a Diesel Marine Engine," *SAE Technical Paper* 2007-01-0670, 2007, https://doi.org/10.4271/2007-01-0670.

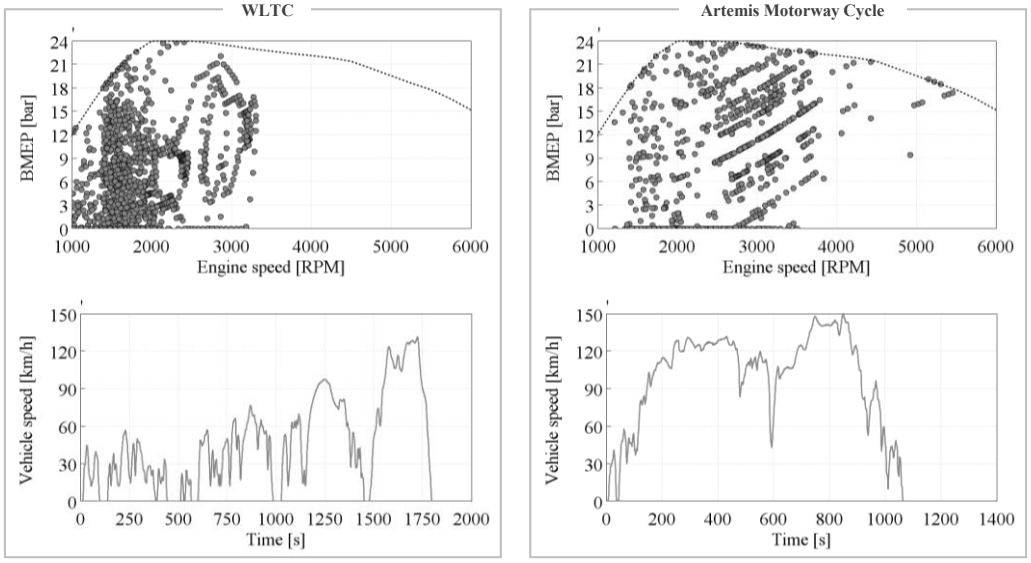
98. Ernst, B, Kammeyer, J, and Seume, JR. "Improved Map Scaling Methods for Small Turbocharger Compressors." *Proceedings of the ASME 2011 Turbo Expo: Turbine Technical Conference and Exposition*, Vancouver, 2011, https://doi.org/10.1115/GT2011-45345.

99. Japikse, D., "Centrifugal Compressor Design and Performance," Concepts E, 1996.

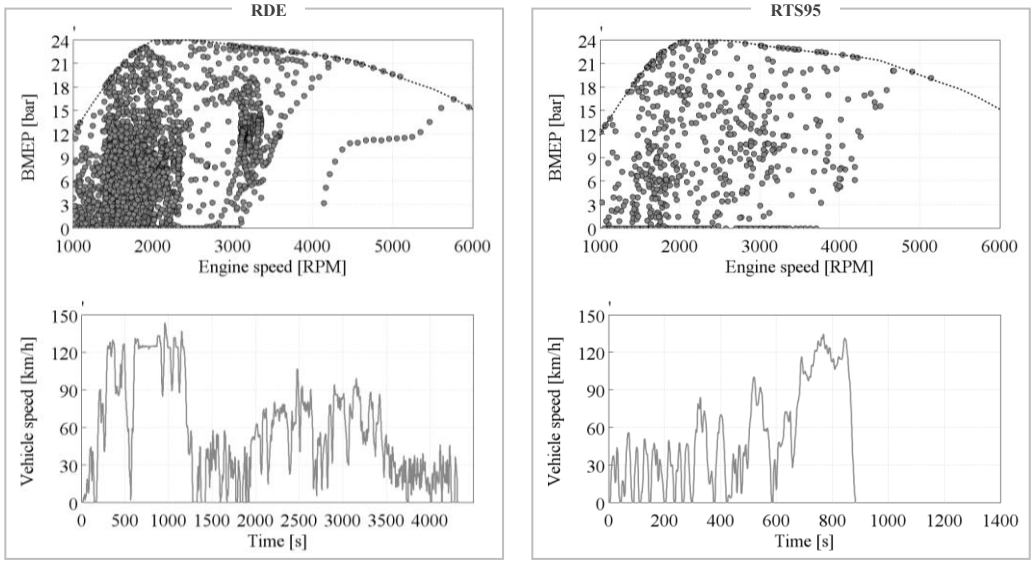
Appendix



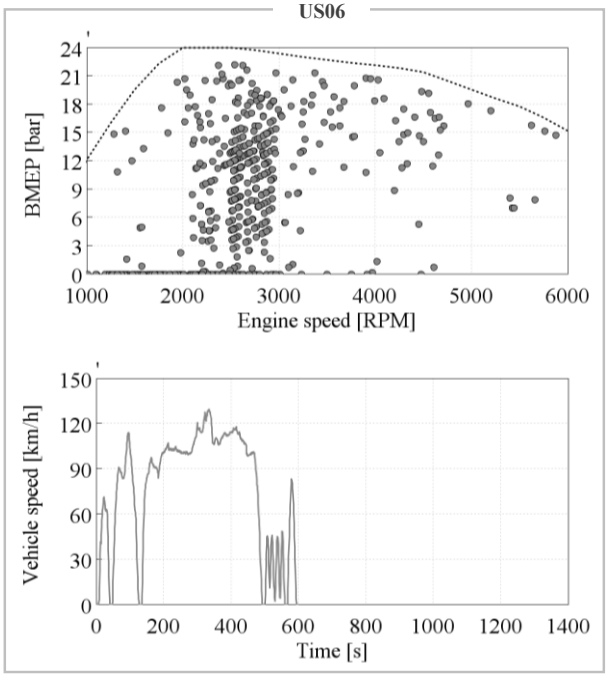
Appendix, Figure A: Driving schedule and main operating points experienced by the engine along the New European Driving Cycle (NEDC) and the Federal Test Procedure (FTP75)



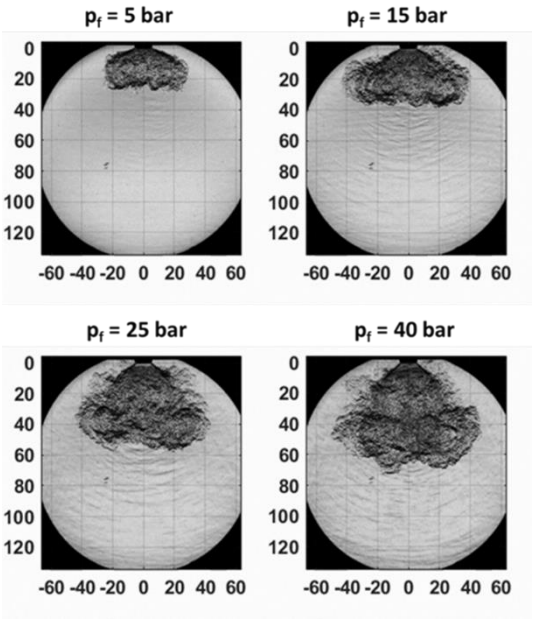
Appendix, Figure B: Driving schedule and main operating points experienced by the engine along the Worldwide Harmonized Light-Duty Test Cycle (WLTC) and the Artemis Motorway Cycle



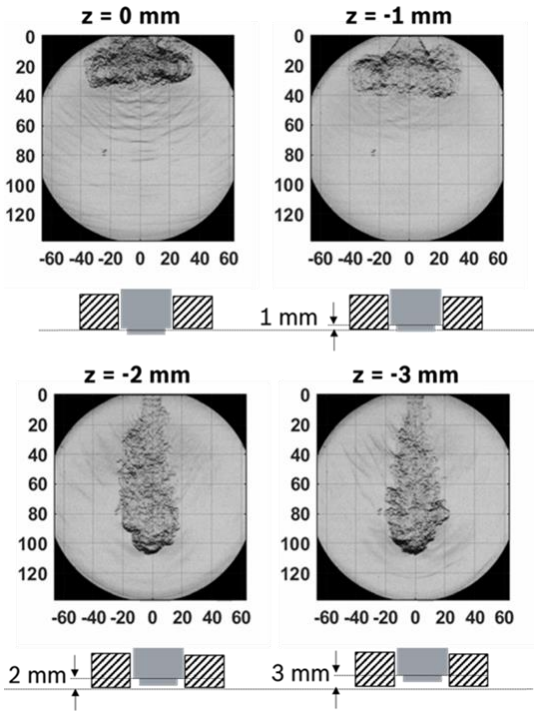
Appendix, Figure C: Driving schedule and main operating points experienced by the engine along a Real Driving Emission cycle (RDE) and the Standardized Random Test for an aggressive driving style (RTS95)



Appendix, Figure D: Driving schedule and main operating points experienced by the engine along the US06 Supplemental Federal Test Procedure



Appendix, Figure E: Schlieren results obtained varying the injection pressure. Fixed parameters: t_i = 3 ms, P_{ch} = 3 bar, T_{ch} = T_f = 22 °C, 2 ms aSoE



Appendix, Figure F: Schlieren results obtained varying the injector mounting position. Fixed parameters: t_i = 3 ms, P_f = 25 bar, P_{ch} = 1.2 bar, T_{ch} = T_f = 22 °C, 1.16 ms ASoE